Chem Soc Rev

Functional Metal-Organic Frameworks as Effective Sensors of Gases and Volatile Compounds

Journal:	*Chemical Society Reviews*
Manuscript ID	CS-SYN-11-2019-000778.R2
Article Type:	Review Article
Date Submitted by the Author:	10-Jun-2020
Complete List of Authors:	Li, Hai-Yang; Zhengzhou University Zhao, Shuna; Zhengzhou University, Zang, Shuang-Quan; Zhengzhou University, Li, Jing; Rutgers State Univ

Chem Soc Rev

REVIW ARTICLE

Functional Metal-Organic Frameworks as Effective Sensors of Gases and Volatile Compounds

Received 00th January 20xx,
Accepted 00th January 20xx

DOI: 10.1039/x0xx00000x

Hai-Yang Li, [†a] Shu-Na Zhao, [†a] Shuang-Quan Zang,[*a] Jing Li [*b]

Developing efficient sensor materials with superior performance for selective, fast and sensitive detection of gases and volatile organic compounds (VOCs) is essential for human health and environmental protection, through monitoring indoor and outdoor air pollutions, managing industrial processes, controlling food quality and assisting early diagnosis of diseases. Metal-organic frameworks (MOFs) are a unique type of crystalline and porous solid materials constructed from metal nodes (metal ions or clusters) and functional organic ligands. They have been investigated extensively for possible use as high performance sensors for the detection of many different gases and VOCs in the recent years, due to their large surface area, tunable pore size, functionalizable sites and intriguing properties, such as electrical conductivity, magnetism, ferroelectricity, luminescence and chromism. The high porosity of MOFs allows them to interact strongly with various analytes, including gases and VOCs, thus resulting in easily measurable responses to different physicochemical parameters. Although much of the recent work on MOF-based luminescent sensors have been summarized in several excellent reviews (up to 2018), a comprehensive overview of these materials for sensing gases and VOCs based on chemiresistive, magnetic, ferroelectric, colorimertic mechanisms is missing. In this review, we will highlight the most recent progress in developing MOF sensing and switching materials with an emphasis on sensing mechanisms based on electricity, magnetism, ferroelectricity and chromism. We will provide a comprehensive analysis on the MOF-analyte interactions in these processes, which play a key role in the sensing performance of the MOF-based sensors and switches. We will discuss in detail possible applications of MOF-based sensing and switching materials in detecting oxygen, water vapor, toxic industrial gases (such as hydrogen sulfide, ammonia, sulfur dioxide, nitrous oxide, carbon oxides and carbon disulfide) and VOCs (such as aromatic and aliphatic hydrocarbons, ketones, alcohols, aldehyde, chlorinated hydrocarbons and N,N'-dimethylformamide). Overall, this review serves as a timely source of information and provides insight for the future development of advanced MOF materials as next-generation gas and VOC sensors.

1. Introduction

Gas is an important state of substances. Generally, normal ambient air consists of oxygen (O_2), nitrogen (N_2), noble gases, carbon dioxide (CO_2) and small amounts of other gases. Air quality is very important for all living organisms on the Earth. However, over the years, the air composition is altered by various gases and volatile organic compounds (VOCs) resulted from human activities and

[a.] *Green Catalysis Center, and College of Chemistry, Zhengzhou University, Zhengzhou 450001, China*
[b.] *Department of Chemistry and Chemical Biology, Rutgers University, Piscataway, NJ 08854, USA*
[c.] *E-mail: zangsqzg@zzu.edu.cn; jingli@rutgers.edu*
† These authors contributed equally to this work.
Electronic Supplementary Information (ESI) available: See DOI: 10.1039/x0xx00000x

Hai-Yang Li

Hai-Yang Li obtained his BS degree in chemistry in 2011 and received his PhD degree in inorganic chemistry in 2017 from Zhengzhou University under the supervision of Prof. Thomas C. W. Mak and Prof. Shuang-Quan Zang in 2017. After then, he joined in the college of chemistry of Zhengzhou University in 2017. His research focuses on the design and synthesis of functional metal-organic frameworks.

Shu-Na Zhao

Shu-Na Zhao obtained her BS degree in Chemistry from Lanzhou University in 2011. She received her PhD degree (2016) in Inorganic Chemistry at Changchun Institute of Applied Chemistry, University of Chinese Academy of Sciences (UCAS) under the supervision of Prof. Hongjie Zhang, where she studied lanthanide metal-organic frameworks for luminescence sensing. She worked as a postdoctoral fellow in COMOC group, Department of Chemistry at Ghent University in 2016-2019. Now, she joined in Laboratory of Functional Crystalline Molecular Materials in Zhengzhou University. Her research interests include synthesis and applications of MOFs in heterogeneous catalysis and chemical sensing.

geological hazards. The excessive emissions of industrial exhausts, including greenhouse gases, industrial toxic gases (such as H_2S, NH_3, SO_2, NO_x, CO_x, CS_2, etc.) and VOCs (such as aromatic and aliphatic hydrocarbons, ketones, alcohols, aldehydes, etc.), have exerted substantial impact on the global climate and environment[1-3]. Therefore, it is critical to develop effective gas and VOC sensors and switches to track environmental conditions, safeguard employees from exposure to harmful chemical species in the working environment, control food quality in agro-industries, aid early diagnosis of diseases in medicine, and monitor indoor air quality (IAQ)[4-6]. Although various conventional gases sensors have been widely used, their inherent limitations have hampered their further development. Thus, designing novel smart sensing and switching materials with superior performance for gases and VOCs is much needed.

MOFs are a type of unique crystalline porous materials self-assembled by metal nodes (metal ions or clusters) and organic ligands via coordination bonds[7-12]. They possess diverse and interesting physical properties, including optical absorbance[13-15], luminescence[16-19], magnetism[20-22], resistance[23,24], conductivity[25-27], and ferroelectricity[28,29], derived from metal nodes, organic ligands, guests, pores, or a combination/collection of some or all of these building blocks. Since their discovery, MOFs have attracted substantial attention and become a rapidly growing material class. Because of their aesthetically pleasing structures (topologically diverse MOFs can be synthesized with different metal nodes and a variety of organic linkers with different coordination numbers), unique characteristics (ultrahigh porosity (up to 90% of the free volume), extraordinarily large surface areas (BET surface area up to 7000 $m^2\ g^{-1}$ and pore volume up to 4.4 $cm^3\ g^{-1}$)[30], tunable pore size/shape, and adjustable internal surface functionality MOFs have demonstrated great potential in numerous applications, such as gas adsorption[31-33], catalysis[34-38], optoelectronics[39-41], bio-imaging[42] and energy storage and conversion[43-46]. In addition, chemical sensing based on MOF materials has become a particularly promising application, due to the advantages listed below: 1) The permanent porosity of MOFs provides large surface areas and numerous active sites for accelerating surface host-guest reactions. The confined pores also allow pre-concentration of target gases and VOCs to high levels, which may enhance the sensing sensitivity. 2) The excellent reversibility of MOFs for the adsorption and desorption of guest molecules render them highly regenerable and recyclable. 3) The tunable pore size, shape and surface environment of MOFs can potentially increase their sensing selectivity and sensitivity; at the same time, chemical selectivity and sensitivity can also be modified by incorporating functional groups (such as Lewis acid or base sites) into the framework. 4) The high crystallinity of MOFs enables precise structure determination which can offer information on the host-guest interactions at the atomic/molecular level. 5) Many MOFs possess high temperature and/or moisture stability, which is often required by numerous applications[47,48].

Based on different working principles, various MOFs have been developed for possible use as chemiresistive sensors, magnetic sensors, ferroelectric sensors, colorimetric sensors, as well as luminescent sensors[49-61]. The inherently low electrical conductivity of most MOFs has historically severely limited their applications in electrical sensors. Fortunately, over the past few years, the development of 2D electrically conductive MOFs (EC-MOFs) and proton-conducting MOFs has facilitated the emergence of MOF-based electronic sensors and switches. Various electrochemical parameters, including resistance, current, potential, impedance, and capacitance, can be changed through the interaction of MOFs with gases and VOCs analytes, boosting their potential as electrical sensing and switching materials[62-69]. In addition, MOF membranes coated onto conductive devices as selective gas filtration layers may enhance the sensitivity and selectivity. Although, MOFs derivatives (e.g. porous carbon materials and metal oxides obtained by simple calcination of MOFs) have shown excellent electrical sensing performances, they will be not included in this review as the focus is on the sensing performances based on the measurable responses between analytes and the integrated MOFs. In the reversible exchange of guest molecules, the amazing phenomenon of single-crystal-to-single-crystal (SCSC) transformations is always accompanied by the cleavage and formation of chemical bonds, thus leading to a change in the local environment of metal nodes and/or even resulting in the dimensional transformation of MOFs[70,71]. The magnetic behaviours (such as magnetic ordering, magnetic susceptibility, hysteresis loop, spin crossover, etc.) of single-molecule magnet (SMM)/single-ion magnet (SIM)-based MOFs can be easily modulated through the SCSC transformation,

Shuang-Quan Zang

Shuang-Quan Zang received his PhD degree in Chemistry from Nanjing University in 2006 under the supervision of Prof. Qingjin Meng. After postdoctoral research with Prof. T. C. W. Mak in The Chinese University of Hong Kong, he joined in the chemistry faculty of Zhengzhou University. His current scientific interests include the atomically precise metal clusters and cluster-assembled materials, functional metal-organic frameworks, luminescence-structure relationship and applications.

Jing Li

Jing Li is a Distinguished Professor in the Department of Chemistry and Chemical Biology at Rutgers University, USA. She received her PhD degree from Cornell University in 1990 under the guidance of Professor Roald Hoffmann. She joined the chemistry faculty at Rutgers University in 1991 as Assistant Professor. She was promoted to Associate Professor in 1996, to Full Professor in 1999, and to Distinguished Professor in 2006. She has published 350+ research articles, invited book chapters and reviews, and holds 15 issued and pending patents. Her research focuses on the development of functional materials for renewable, sustainable and clean energy related applications.

indicating that MOFs represent promising magnetic switching materials[72-74]. In particular, polar guest molecules with an orderly arrangement in the pores may lead to the spontaneous polarization of MOFs, and thus ferroelectricity will be realized. Similarly, the ferroelectricity of MOFs has been modulated by the SCSC transformation[75,76]. In addition, colorimetric sensors are based on colour changes of MOFs. This area is rapidly expanding simply because a colour change is the most easily visualizable and simplest signal for gas and VOC sensing[77-79]. While the research on MOF sensors based on electricity, magnetism, ferroelectricity and chromism is comparably still in its early stage; a comprehensive discussion on their sensing mechanisms and methods is urgently needed.

Luminescent MOFs (LMOFs) based gas and VOC sensors that depend on luminescent signal transduction have been studied extensively and have been discussed comprehensively in many excellent reviews published up to 2018[6,53,54,80-83]. Nevertheless, with the rapid development of MOF materials, significant improvement in their luminescence-based gas and VOC sensing performance has been achieved even within a very short time period. For example, Su and co-workers reported an ultrafast (on the order of seconds) water vapor sensor based on a robust microporous Zn-MOF with switchable luminescence[84]. The detection of trace amounts of water (ppm level) in organic solvents was achieved by various MOF materials, which is very important for industrial processes. The scope of detectable analytes has also been expanded over the past few years, such as dissolved oxygen[85,86] and acid vapors[87-89]. Using metal nanoclusters as metal nodes, a novel type of MOFs, cluster-based MOFs, was recently discovered and bridges the gap between metal nanoclusters and MOFs, showing significant advantages in gas and VOC sensors and switches[90-93]. Furthermore, the integration of MOFs into thin films for sensors of gases and VOCs and the construction of logic gates from luminescent signal transductions have allowed researchers to come closer to developing portable sensors of gases and VOCs.

In this review, we will focus on the development of MOF sensors and switches for the detection of gases and VOCs based on the principles of electricity, magnetism, ferroelectricity, and chromism, as well as the most recent advances on the LMOFs sensors. In Section 2, we will highlight the basic mechanisms and methods of MOF-based sensing. Sensing applications of MOFs targeted on different analytes, including oxygen, water vapor, toxic industrial gases (such as hydrogen sulfide, ammonia, sulfur dioxide, nitrous oxides, carbon oxides and carbon disulfide), and VOCs (such as aromatic and aliphatic hydrocarbons, ketones, alcohols, aldehyde, chlorinated hydrocarbons and N,N'-dimethylformamide) will be overviewed in Section 3. The challenges and prospects of this research topic will also discussed in detail to provide insights into the further development of advanced MOF materials for next-generation sensors of gases and VOCs.

2. Methods and Mechanisms of MOF-Based Sensing

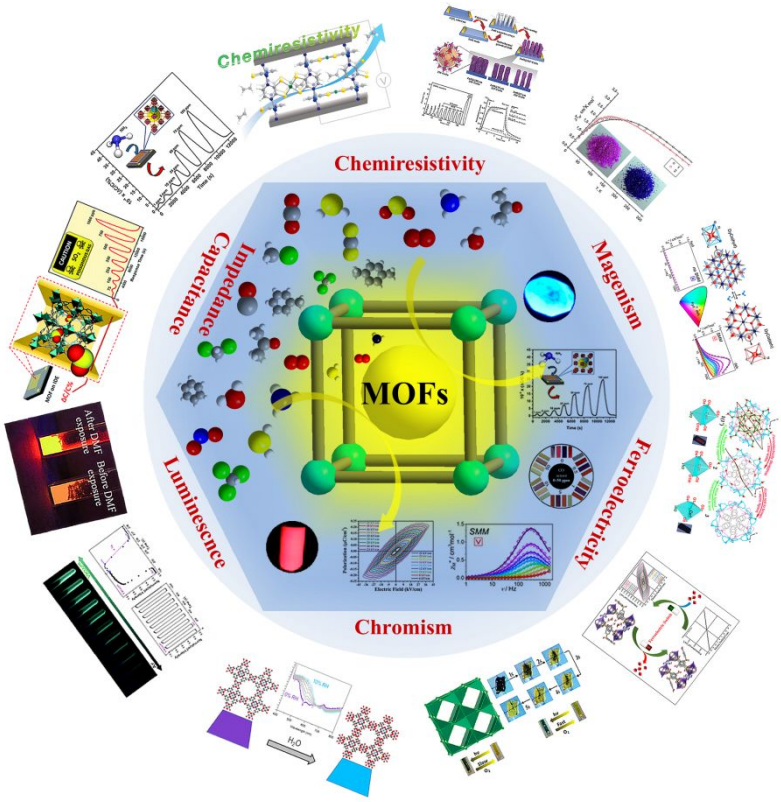

Fig. 1 Sensing based on different properties of MOFs.

The general sensing mechanisms of sensors are based on signal transduction arising from the surface reaction or adsorption of gas molecules on the sensing materials. MOFs with very large surface areas and functional groups afford sufficiently strong interactions with guest molecules, which can affect the properties of MOFs through changes in optical, electrical, and mechanical signals. Generally, major methods for gas sensing are optical (vapochromism, luminescence, and interferometry), mechanical techniques (quartz crystal microbalance, surface acoustic wave devices, and microcantilevers), magnetism, and electrical sensing (impedance, ferroelectric, chemicapacitive, and chemiresistive) (Fig. 1).

2.1 Chemiresistive MOF-Based Sensing

The basic working principle of chemiresistive sensors is a change in the electronic properties or resistance of the sensing material upon the adsorption of and interaction with the analysed gas[48]. Compared to conventional porous materials, MOFs have large surface areas for interacting with gas molecules. However, the inherently low electrical conductivity of most MOFs has substantially limited their electrical sensing applications. Within the past ten years, the improvements in EC-MOFs and MOF-based electronic devices have made them wonderful candidates for various electrochemical applications in supercapacitors, electrocatalysis, proton conduction, and field-effect transistors. Furthermore, the coexistence of a large surface area, tunable pore size and conductivity in EC-MOFs creates a new platform for advances in next-generation chemiresistive sensors[94-99].

The mechanism of chemiresistive MOF-based sensors is mainly attributed to the absorption of gas molecules by the functional material that causes electron and hole transfer, or the gas molecules react on the surface of functional material, resulting in changes in the resistance (or conductance) of sensing materials. Because of the uniqueness of MOFs, many different mechanisms for MOF-based chemiresistive sensors have been identified (Fig. 2). The gas molecules adsorbed on the surface of MOFs change their resistance by interacting with the framework. The redox reaction between gas molecules and active metal sites or active functional organic groups in MOFs changes the conductivity of MOFs. In addition, the conductivity of MOFs varies with the structural changes caused by the adsorption of gas molecules.

Because of the low-cost fabrication and ease of miniaturization, chemiresistive sensors have been widely studied. However, selectivity and sensitivity are still the major challenges for chemiresistive sensors. MOFs with ultra large surface areas, ultrahigh porosity, and tunable framework structures are ideal sensing materials. The first MOF-based chemiresistive sensor was investigated by Zhang et al[100]. The authors constructed a Co-based ZIF-67 sensor that detected formaldehyde at concentrations as low as 5 ppm due to its large surface area. However, the operating temperature was as high as 150 °C, revealing the poor room temperature conductivity of ZIF-67. The poor electrical conductivity of most MOFs has substantially limited their electrical sensing applications. In recent years, numerous developments have been achieved in the use of EC-MOFs, MOFs with electrically conductive guest, and MOF membranes as chemiresistive sensors. Notably,

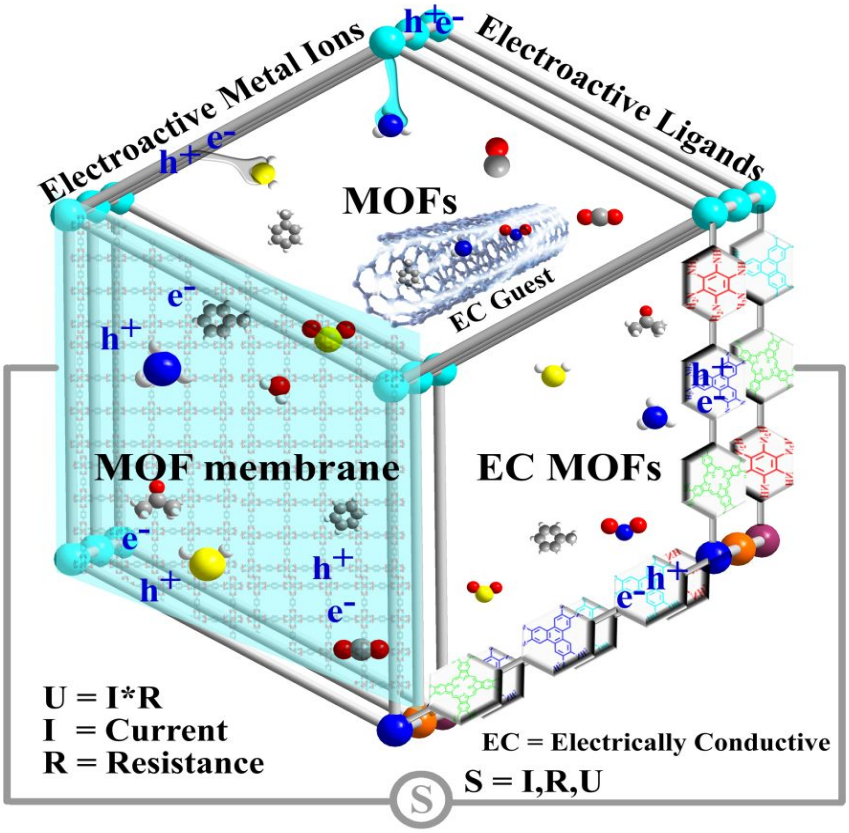

Fig. 2 The sensing mechanism of MOF-based chemiresistive sensors.

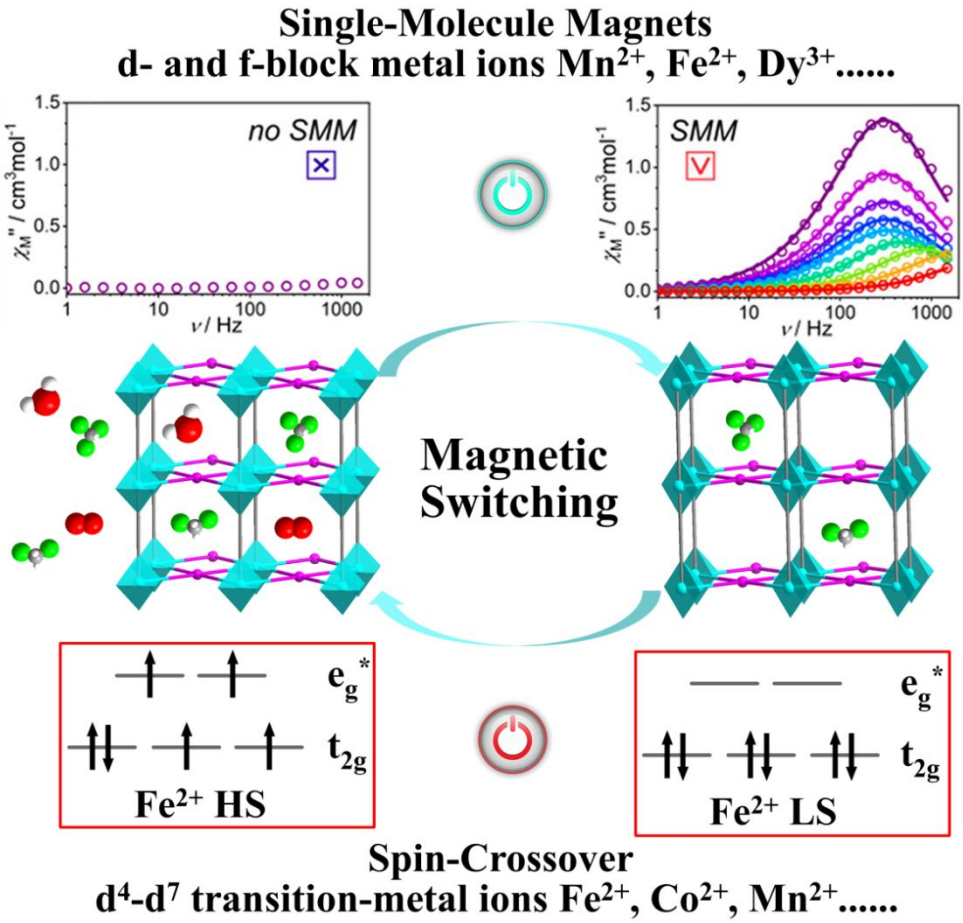

Fig. 3 The sensing mechanisms of magnetic MOF-based sensor.

2D EC-MOFs have been investigated by the Xu, Martí-Gastaldo and Dincă laboratories[95–97, 101]. EC-MOFs with the advantages of high porosity, diversity and excellent electrical conductivity suggest that they represent appealing candidates for chemiresistive sensors.

In addition, coating MOF membranes onto sensing devices is a promising method to solve the inherently poor selectivity and sensitivity of chemiresistive sensors. MOF membranes have been rationally designed with an appropriate pore size for the selective separation of target gas molecules, and the enrichment of thin films may increase the sensitivity to gas molecules. Xu et al reported the controllable high-quality fabrication of a thin film of an EC-MOF, $Cu_3(HHTP)_2$. The $Cu_3(HHTP)_2$ thin film shows good selectivity for NH_3 in the presence of different interfering gases, a low limit of detection (LOD), fast response time, and excellent stability and reproducibility[97]. Thus, MOFs are ideal materials for chemiresistive sensors, and relevant studies will develop rapidly in the future.

2.2 Magnetic MOF-Based Sensing

Magnetic MOF-based sensing switches are mainly produced from two types of magnetic MOFs, the spin crossover MOFs (SCO MOFs) and SMMs/SIMs MOFs (Fig. 3). The SCO MOFs have been one of the main focuses of research into molecular functional materials. The metal centres of SCO MOFs are common transition metal ions with d^4-d^7 electronic configurations, because these metal ions may exist in high spin (HS) and low spin (LS) states. For example, the iron(II) ion displays the $t_{eg}^4e_g^2$ ($^5T_{2g}$) configuration for the HS state and $t_{eg}^6e_g^0$ ($^1A_{1g}$) configuration for the LS state. SCO MOFs respond to external physical and chemical stimuli, and switch between the two characteristic HS and LS states of metal ions, resulting in changes in the structure, colour, magnetic behaviour, dielectric constant, luminescence and other physical properties of the material. SCO MOFs show a considerably valuable application prospects in the fields of colour devices, molecular switches, molecular sensors and other devices[102-105]. In addition, the spin states may be affected by the guest molecules through coordinated or other interactions, and thus SCO MOFs represent perfect candidates for gas sensors.

SMMs/SIMs composed of d- and f-block (Mn^{2+}, Fe^{2+}, Dy^{3+} etc.) metal complexes have attracted increasing attention for potential applications in spintronic devices, quantum information processing systems, and high-density magnetic memory. In recent years, the magnetic switch has become a research hotspot because the magnetism of SMMs/SIMs is very sensitive to an external stimulus, such as temperature, pressure, light, and guest molecules. However, 0D SMMs/SIMs readily collapse in the presence of the external stimulus and reversible regulation is difficult to achieve, which also limits their sensing applications. In comparison, MOFs display much higher stability. Therefore, the SMMs/SIMs MOFs constructed with SMMs/SIMs as nodes and functional organic ligands as linkers are promising candidates for magnetic switches, because the MOFs are able to undergo SCSC transformations in response to different stimuli. The SCSC transformations of MOFs

occur with the exchange of the guest solvent molecules or cleavage and formation of chemical bonds, which modulate the magnetism. For instance, the reversible exchange of coordination solvent molecules alters the coordination environment of the metal centre and subsequently alters the spin state. The reversible exchange of guest solvent molecules potentially affects the angles and distance between ligands and metal ions and further change the coordination modes of metal centre and may also lead to crystal lattice transformations, resulting in bond formation or cleavage that subsequently affects magnetism[106-109]. Furthermore, the sizeable effect of lattice solvents may alter the interactions and subsequently exerts a profound effect on the magnetic property.

The SMMs/SIMs MOFs and SCO MOFs are appealing candidates for magnetic switches, due to the combination of the porosity, optical, and electric properties of MOFs and the magnetism. However, the MOF-based magnetic switches are still rare, particularly in combination with other properties. Therefore, the rational design of SMMs/SIMs and SCO MOFs that take full advantage of the synergy of MOFs and SMMs/SIMs or SCO to construct MOF-based sensors with multiple response properties still requires additional investigations.

2.3 Ferroelectric MOF-Based Sensing

The ferroelectricity of a crystal refers to the phenomenon in which the positive and negative charge centres of the crystal do not coincide and the electric dipole moment appears, leading to spontaneous polarization. The space groups of ferroelectric compounds must belong to the 10 polar point groups (C_1, C_s, C_2, C_{2v}, C_3, C_{3v}, C_4, C_{4v}, C_6, and C_{6v}). Therefore, crystallinity is a prerequisite for ferroelectric materials. Crystal MOF materials can be enriched ferroelectric materials due to their unique characteristics, including an ultrahigh porosity, tunable pore size, and designable function (Fig. 4). The ferroelectric properties of MOFs are mainly derived from the hydrogen bond interactions of MOFs and polar guest molecules, which endow them with ferroelectric properties[28]. In addition, MOFs have been used as ferroelectric switch materials due to their sensitivity to external stimuli; MOFs easy undergo the SCSC transformation in response to external stimuli. Zang et al. investigated a polar chiral 3D MOF that contains two outer coaxial unequal double-helical chains and induces the helical guest water columns[75]. Importantly, the MOF displays two-step fast reversible SCSC transformation, and the first step of SCSC transformation involves the desorption/adsorption of guest water molecules, accompanied by the ferroelectric switchable property.

As a ferroelectric switch, MOFs are still in the initial stage of development. This limited development is because the MOFs used as ferroelectric switches must meet more stringent conditions. First, the space groups of MOF must belong to polar point groups. Second, the MOF should have hydrophilic cavity. Therefore, the synthesis of MOF-based ferroelectric switches is random, which limits the development of MOF ferroelectric switches. In addition, the measurement of ferroelectric properties requires large-scale single crystals, but MOFs are unable to easily form large-scale crystals, which also limits the universality of MOF-based ferroelectric switches. Due to the chemical versatility, ultrahigh porosity and high compatibility of MOFs with other materials, MOFs may serve as a host to construct multifunctional composites with ferroelectric materials to achieve the coupling between ferroelectricity and other useful properties, such as optical, electric, and magnetic properties. This approach may provide new types of sensing materials and improve the development of new types of sensors.

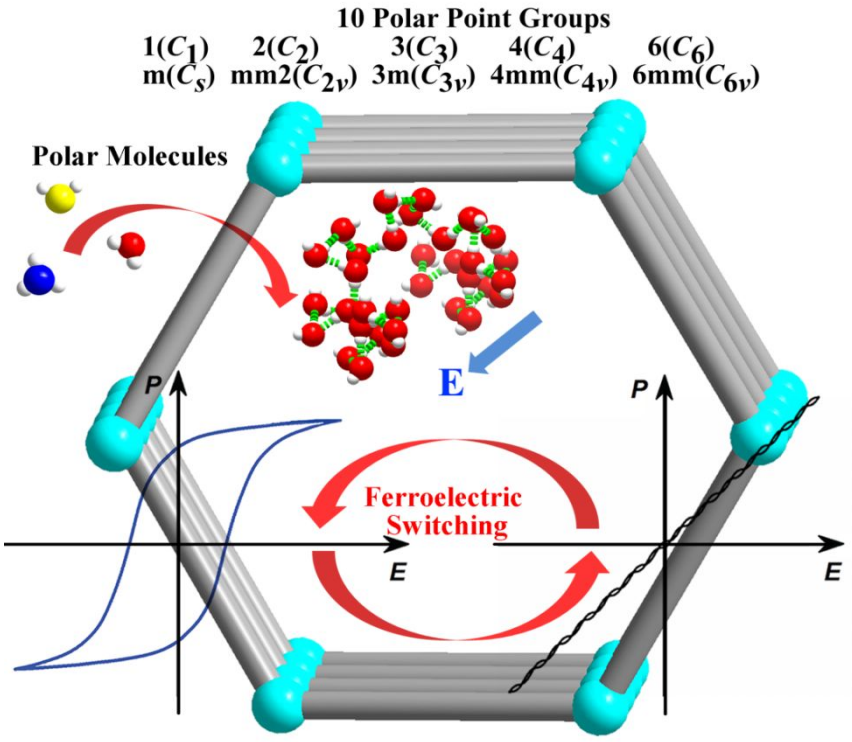

Fig. 4 The sensing mechanism of ferroelectric MOF-based sensor.

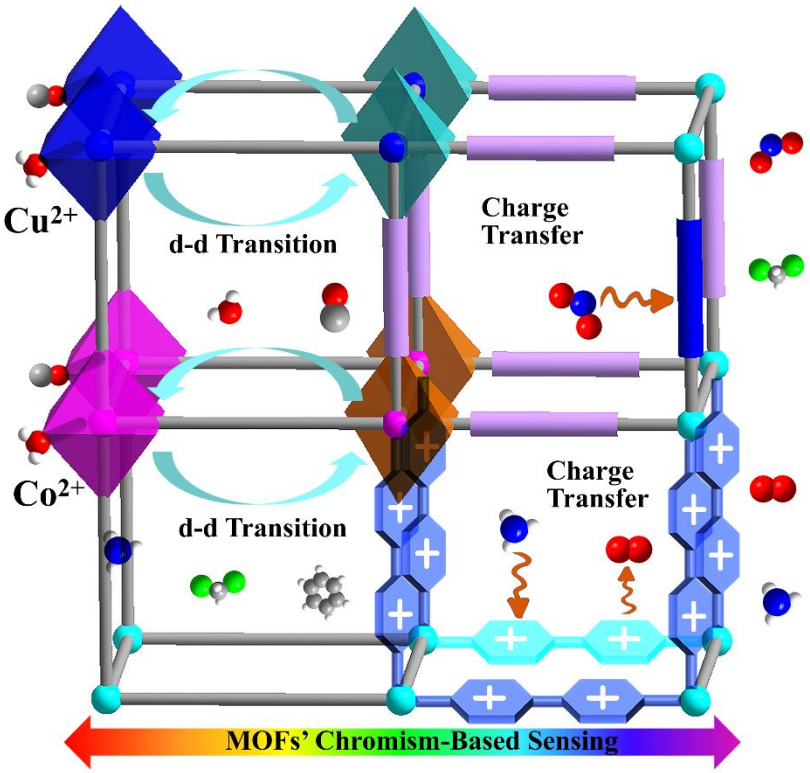

Fig. 5 The chromism-based sensing mechanisms of MOFs

2.4 MOFs' Chromism-Based Sensing

The colour change of MOFs is the most easily visualized and simplest signal for gas sensors (Fig. 5). Normally, the colour change is achieved through two common mechanisms. First, the metal coordination geometry is altered by the reversible removal/reabsorption of coordination molecules. The coordination molecules can be lost in response to light, temperature or pressure, resulting in an alteration in the coordination modes of metal centre, a change in the d-d transition process and a change in the absorption spectrum of MOFs[110-112]. In addition, the exposed metal site readily interacts with gas or vapor guest molecules.

Second, the interactions between numerous guest and host molecules may alter the charge transfer process between the ground and excited electronic states, and thus the absorption spectrum will be correspondingly modified[113-117]. Dong et al. preformed a porous Cu^{+}-MOF assembled with Cu^{+} and 1-benzimidazolyl-3,5-bis(4-pyridyl)benzene[113]. Cu^{+}-MOF functions as a sensitive visual colorimetric sensor for water through a solvent-induced SCSC process. When Cu^{+}-MOF is exposed to air for a predetermined period, the encapsulated organic molecules (CH_3CN and MeOH) will be replaced by the water vapor in air, resulting in a change in the colour from yellow to red brown. Moreover, the colour of crystals displays different responses at different humidity levels, enabling Cu^{+}-MOF to function as a visual colorimetric humidity sensor. The sensing mechanism is that the diverse size of guest analytes can form different guest and host interactions, and thus induces changes in structural parameter.

In addition, viologen-based MOFs are interesting sensors that use the charge transfer process to achieve their unique photoelectric properties. Viologen-functionalized MOFs display excellent photochromic properties through a charge transfer process upon light exposure, and the viologen-based MOFs also change their colour through charge transfer between electron-rich molecules such as amines[77,118,119]. Importantly, the coloured MOFs can decolour in the presence of oxygen, making them excellent oxygen sensors[120,121]. Lu et al. reported a porous MOF containing methyl viologen cations[120]. Due to the effective photoresponse of the viologen compound, the colour of MOF changes from dark-yellow to black after X-ray irradiation. After exposure of the colourful MOF to pure O_2 or an oxygen-containing atmosphere, the colour immediately returns to dark-yellow (within 5 s). Although the sensor based on a colour change is the most easily visualized gas sensor, studies of chromism-based sensors incorporating MOFs are still rare, and more attention and research are needed to focus on the chromism-based sensing mechanism of MOFs.

2.5 Luminescent MOF-Based Sensing

Luminescent metal organic frameworks (LMOFs) are an important branch of MOFs with a number of possible applications in lighting, optical communications, biomedical devices and chemical sensing. To date, a substantial number of LMOFs have been discovered, and their luminescence can originate from various sources. 1) Luminescence arises from organic ligands. This type of ligand normally features extended π-conjugation systems (Fig. 6a). The fluorescence of organic molecules includes two basic forms, fluorescence and phosphorescence; the molecular fluorescence corresponds to the spin-allowed transition from its first singlet state S_1 to the ground singlet state S_0 and has a short excited state lifetime on the order of 1–100 ns. Phosphorescence is based on

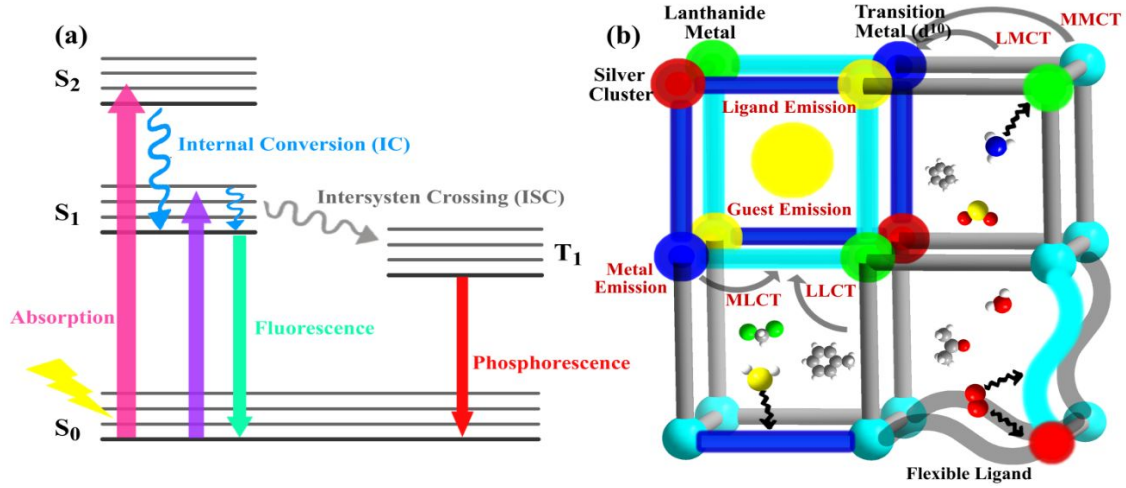

Fig. 6 (a) Schematic illustrating the various photophysical processes. (b) The sensing mechanisms of luminescent MOF-based sensors.

the transition from triplet state T_1 to S_0, which is spin-forbidden and is characterized by excited state lifetimes of 1 μs or longer. 2) Metal-centred emission, such as lanthanide metal ions, d^{10} transition metal ions, and silver clusters, has also been observed. Lanthanide ions show narrow and unique 4f-4f transitions and the emission of lanthanide ions ranges from ultraviolet (UV) to near-infrared (NIR) wavelengths. 3) Charge-transfer luminescence is based on the transition from the charge-transfer excited state to the ground state, including ligand-to-ligand charge transfer (LLCT), metal-to-ligand charge transfer (MLCT), ligand-to-metal charge transfer (LMCT) and metal-to-metal charge transfer (MMCT). 4) Guest emission from lanthanide ions and fluorescent dyes encapsulated in the pores of MOFs and guest-sensitization luminescence are other types of luminescence. In addition, the various interactions between the guest and host framework may change the luminescent properties of MOFs (Fig. 6b).

Due to their unique characteristics, LMOFs have become the most widely studied type of MOF sensors. For example, the inherent porosity ensures the adsorption of analyte species into the MOF pores, abundant interactions can occur between guest analytes and the host framework, such as van der Waals interactions, halogen bonding, hydrogen bonding, and π-π stacking interactions, and tunable pore size of the MOFs allows systematic control of the selectivity for the targeted analytes. The inherent crystallinity of MOFs has facilitated analysis of the sensing mechanism when a precise crystal structure of analyte@MOF structure can be determined to probe the exact interactions between the analyte and the host framework. In addition, the rational design of the MOFs with specific functional groups and tunable electronic structures has endowed LMOFs with desirable luminescence that are more suitable for sensing applications. Furthermore, the luminescent property of MOFs is very sensitive to the species and concentration of guest analytes and small changes in the surrounding environment. In LMOFs, the main sensing mechanisms include photoelectron transfer (PET), intermolecular charge transfer (ICT), Förster resonant energy transfer (FRET), and competitive adsorption, among others. Several recent review articles have summarized LMOF-based sensors[16,17,42,52-54,80-83].

However, with the rapid growth of the MOF field, new types of MOFs and new types of sensing mechanisms are emerging. Recently, some new types of MOFs have been reported to function as sensor materials[90-92]. Zang et al. creatively combined the silver(I) chalcogenide/chalcogenolate clusters (SCCs) with MOFs to construct rigid SCC-based MOFs (SCC-MOFs, Ag_{12}bpy)[90]. SCC-MOFs successfully solve the inherent instability and poor quantum yield (QY) of SCCs by assembling SCCs and rigid organic ligands. Importantly, Ag_{12}bpy potentially functions as an ultrafast visual fluorescence turn-off oxygen sensor. In addition, Ag_{12}bpy also displays different emission colours from green to yellow-orange at room temperature upon exposure to VOCs, and the emission exhibited an excellent linear correlation with the empirical parameters of the solvent polarity values. Furthermore, new sensing mechanisms are improved. The traditional sensing mechanism is the reversible coordination or interaction of the analyte with the probe, such as via physical/electrostatic interactions, and the new sensing mechanism is the irreversible reaction of the target analyte with a probe to yield a product that is chemically different from the starting probe via target-induced oxidation, hydrolysis, and nucleophilic processes, which will substantially increase the selectivity of the sensor.

Moreover, combined with the logic operation, INHIBIT or IMPLICATION-type logic gate-based luminescence sensors have been constructed, and the preparation of MOF film sensors will stimulate the development of MOF-based gas sensor devices[84,90,122,123]. Qian et al. investigated two Tb-based LMOF films constructed using a postfunctionalization method[122]. Both films exhibit fast and reversible detection of O_2 due to the binding interaction between the extra carboxylic acid and incorporated Tb ion in MOF that improves the efficiency of energy transfer. With the development of the MOF field, the response speed, detection limit, selectivity and stability of LMOF gas sensors have been improved. The combination of the logic operation and the preparation of a MOF film sensor will promote the development of MOF gas sensor devices. However, these devices are still far away from real commercialization, and substantial efforts are still needed.

2.6 Sensing Based on Other Properties of MOFs

In addition to the aforementioned aspects, MOFs with other properties, such as impedance or chemicapacitive properties, are also being investigated as sensing materials. The high porosity and

tunable pore size of MOFs allow guest molecules to easily access the cavity. The strong interactions between guests and hosts induce changes of the properties of MOFs. In principle, any MOF can be used as a sensing material as long as its chemical or physical properties change at a detectable level upon exposure to the guest molecules.

3. Sensing Application of MOFs

MOFs are ideal candidates as gas-sensing materials and have been widely used to detect oxygen, water vapor, toxic and hazardous gases, special air pollutants, and VOCs.

3.1 Oxygen Sensing

Oxygen is the most important and essential element in our life that provides metabolic energy to cells during cellular respiration. In the healthy organs, tissues, and cells, oxygen levels must be maintained within a certain range. Hypoxia and hyperoxia are both pathological conditions and causes of various diseases. The former may cause diseases such as cardiac ischaemia, pulmonary disease, inflammatory diseases, and cancer, whereas the latter results in oxygen toxicity syndrome. Oxygen also has a wide range of applications in the chemical industry, defence industry and medical treatment. Therefore, the detection of oxygen is very important in medical diagnoses, chemistry, and industry, in which the required O_2 detection level ranges from the ppm level to ambient pressure

A magnetic MOF-based oxygen sensor was investigated by Jung et al.[124,125]. The authors used the most extensively studied Fe–MOF-74 (Fe_2(dobdc), $dobdc^{4-}$ = 2,5-dioxido-1,4-benzenedicarboxylate) to investigate the relationship between the absorption of oxygen molecules and the magnetic property[120]. The high electron affinity of oxygen withdraws a minor spin electron from the Fe centres in the MOF, and the significant back donation develops a new situation for superexchange interactions that promote the ferromagnetic coupling between Fe centres to subsequently regulate the magnetic property. Based on the theoretical calculations, O_2 adsorption also results in the ferromagnetic ordering along the 1D chain of the MOF framework.

Studies of chromism-based oxygen sensors composed of MOFs have focused on viologen-functionalized MOFs[120,121] Lu et al. reported a stable porous MOF containing methyl viologen cations, which functions as fast and selective sensor for oxygen that is visible to the naked eye[120]. Due to the effective photoresponse of the viologen compound, the colour of MOF changes from dark-yellow to black after X-ray irradiation. After exposure of the coloured MOF to pure O_2 or an oxygen-containing atmosphere, the colour returns to dark-yellow within 5 seconds and is visible with the naked eye (Fig. 7a), but the colour fails to change in the presence of other gases, such as N_2 and CO_2. Thus, the MOF is a valuable option for the fast and selective detection of oxygen. The charge transfers between viologen radicals and oxygen molecules and the occurrence ofoxidative quenching comprises the sensing mechanism. Zhang et al. also investigated two viologen-functionalized MOFs[121], and both show photochromic properties (Fig. 7b). The difference is that the colour of the nonporous MOF changes under both anaerobic or air conditions and slowly returns to the original colour, whereas the

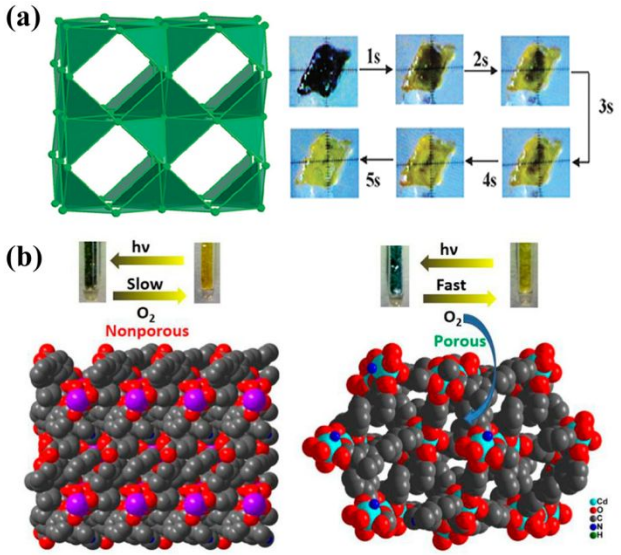

Fig. 7 (a) Polyhedral representation of the 3D framework and the photographs of the bleaching process from black to dark-yellow by O_2 within 5 seconds. Reproduced with permission from ref. 120. Copyright 2013, Royal Society of Chemistry. (b) The structures of porous and nonporous viologen-based MOFs and visually sensing of oxygen. Reproduced with permission from ref. 121. Copyright 2018, American Chemical Society.

porous MOF only changes colour under anaerobic conditions and recovers immediately; at the same time, they are easily examined with the naked eye. The different response times may be caused by the one-dimensional channels of porous MOFs that provide a pathway for oxygen molecules and the charge transfer process occurs easily.

The luminescent oxygen sensor is the most widely used sensor due to its fast response and high sensitivity; therefore, high levels of luminescence emission and long luminescence lifetimes are prerequisites for an effective oxygen sensor[85,86,90,122,126-144]. In recent decades, phosphorescent coordination complexes such as Ir^{3+}, Pt^{2+}, Pd^{2+}, and Ru^{2+} complexes have been studied as oxygen sensors[126-130]. Lin et al. developed a MOF (R-UiO) with two types of ligands possessing distinct oxygen sensitivities[128]. Pt-5,15-di(p-benzoato)porphyrin (DBP-Pt) is O_2-sensitive, but the rhodamine-B isothiocyanate (RITC)-conjugated quaterphenyldicarboxylate (QPDC) is O_2-independent. The MOF displays interesting phosphorescence/fluorescence dual-emission performance. The loading of different amounts of rhodamine-B produced R-UiO-1 (containing 0.6 mol% Rhodamine-B) and R-UiO-2 (containing 1.6 mol% rhodamine-B) by controlling the amount of RITC. As shown in Fig. 8, R-UiO-1 exhibits two emission peaks, one strong emission peak detected at 630 nm was attributed to DBP-Pt and the other weak emission peak located at 570 nm was ascribed to RITC. Interestingly, as the oxygen partial pressure gradually increased, the intensity of the 570 nm fluorescence emission peak stayed the same, while the intensity of the 630 nm phosphorescence emission peak was substantially reduced, achieving the excellent ratiometric sensing of oxygen, and the R_I^0/R_I ($R_I^0 = I_P^0/I_F^0$, $R_I = I_P/I_F$) displayed a good linear relationship with the oxygen pressure up to 80 mmHg. More importantly, R-UiO is the first NMOF that functions as an intracellular O_2 biosensor.

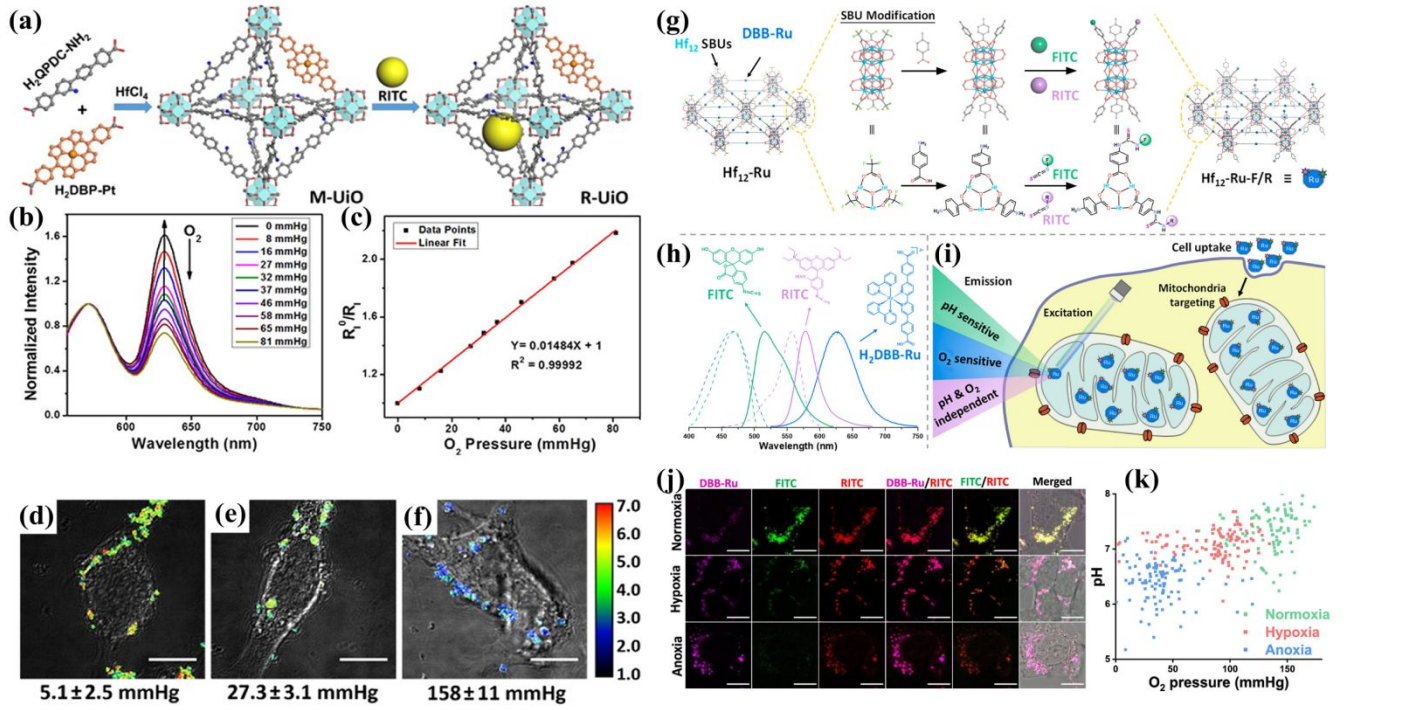

Fig. 8 (a) Synthesis of mixed-ligand M-UiO NMOF and its postsynthesis modification to afford R-UiO NMOF. (b) Emission spectra (λ_{ex} = 514 nm) of R-UiO-1 in HBSS buffer under various oxygen partial pressures. (c) Plot of R_I^0/R_I ($R_I^0 = I_P^0/I_F^0$, $R_I = I_P/I_F$) as a function of oxygen pressure. Ratiometric luminescence imaging (λ_{ex} = 514 nm) of CT26 cells after incubation with R-UiO-2 under (d) hypoxia, (e) normoxia, and (f) aerated conditions. Scale bar: 10 μm. Reproduced with permission from ref. 128. Copyright 2016, American Chemical Society. Schematic showing the synthesis of multifunctional Hf_{12}-Ru-F/R. (g) Surface modification of Hf_{12}-Ru by exchanging TFA capping groups on Hf_{12}SBUs with p-aminobenzoate groups and covalent conjugation of FITC and RITC to Hf_{12}SBUs by forming thiourea linkages. (h) Chemical structures and excitation/emission spectra of FITC, RITC, and H_2DBB-Ru. (i) Positively charged Hf_{12}-Ru-F/R targets mitochondria and allows ratiometric sensing of intramitochondrial pH and oxygen via the luminescence ratios of pH-sensitive FITC to pH-independent RITC and O_2-sensitive DBB-Ru to O_2-independent RITC, respectively. (j) Ratiometric luminescence imaging of CT26 cells after incubation with Hf_{12}-Ru-F/R under normoxia, hypoxia, and anoxia conditions. Scale bar = 10 μm. (k) Scatter plot showing a positive correlation between pH and P_{O_2} in mitochondria as sensed by Hf_{12}-Ru-F/R. Statistical analysis gave a Pearson correlation coefficient (r) of 0.66. Reproduced with permission from ref. 129. Copyright 2019, American Chemical Society.

The authors further investigated another oxygen sensor with a nanoscale MOF $Hf_{12}(\mu_3\text{-}O)_8(\mu_3\text{–}OH)_8(\mu_2\text{-}OH)_6(DBB\text{-}Ru)_6(TFA)_6$ (Hf_{12}-Ru, H_2DBB-Ru = $Ru(H_2DBB)(bpy)_2^{2+}$, DBB = 4,4′-di(4-benzoato)-2,2′-bipyridine, bpy = 2,2′-bipyridine, TFA = trifluoroacetic acid)[129], and covalent conjugation of fluorescein isothiocyanate (FITC) and RITC to Hf_{12}-Ru to produce Hf_{12}-Ru-F/R. Hf_{12}-Ru-F/R functions as a ratiometric pH sensor in the unique mitochondria environment based on the luminescence ratios of FITC to RITC for their different response properties (Fig. 8g-i), and O_2 sensing is achieved by calculating the ratio of the fluorescence of the O_2-sensitive DBB-Ru to O_2-independent RITC in live cells (Fig. 8j and k). This study provided the first quantitative evidence for a positive correlation between the pH value in the mitochondria and the local O_2 concentration.

Another type of MOF with excellent luminescence is d^{10} transition metal-based MOFs, such as Zn^{2+}-, Cu^{+}-, and Cd^{2+}-based MOFs[131-134]. Zhang et al. creatively constructed a highly porous and fluorescent MOF $[Zn_4O(bpz)_2(abdc)]$·guest (bpz = 4-(3,5-dimethylpyrazol-1-id-4-yl)-3,5-dimethyl -pyrazol-1-ide, H_2abdc = 2-aminoterephthalic acid)[131]. The good stability and bright blue photoluminescence suggest that the MOF has potential applications in sensing, which was confirmed by further luminescent tests in the presence of different gases. The fluorescence of MOF was selectively quenched by O_2, and the photoluminescence experiments performed at different O_2 pressures revealed an ultrafast response speed and ultrashort response time. The MOF displays a unique high oxygen-sensing efficiency as the fluorescence intensity is quenched by 96.5% at 1 bar of O_2. The fluorescence circulating tests under the alternating conditions of 1 bar of O_2 and a vacuum reveal that the O_2 sensing process is rapid, reversible, and highly stable (Fig. 9a-e). The O_2 sorption experiments indicate that O_2 with an appropriate molecular size effectively enters the cavity. The efficient quenching of fluorescence derived from a singlet excited state is potentially explained by several quenching pathways, such as the charge transfer between singlet excited state and triplet oxygen.

Chen and colleagues published several meaningful studies of oxygen sensors in succession. They prepared a fluorescent MOF $[Zn_7(ip)_{12}](OH)_2$·guest (Hip = 1H-imidazo-[4,5-f][1,10]phenanthroline)[132]. The MOF was doped with very small amounts of Ru^{2+}, resulting a highly efficient and tunable oxygen quenching material that functions as a chromism-based oxygen sensor (Fig. 9f and g). However, the only disadvantage is that Ru^{2+} is noble metal, and thus their next study encapsulated organic molecules into a metal-organic zeolite framework. Pyrene was selected for its high photoluminescence quantum yield, appropriate sensitivity and photostability characteristics; at the same time, $[Zn(mim)_2]$ (Hmim = 2-methylimidazole, MAF-4) was chosen as carrier[85]. The pyrene@MAF-4 was prepared using an *in situ* loading method, which exhibits fast response as a fluorescence O_2 sensor, and the use of different loading ratios of pyrene affects the diffusion coefficients of oxygen and resulting tunable sensitivity of

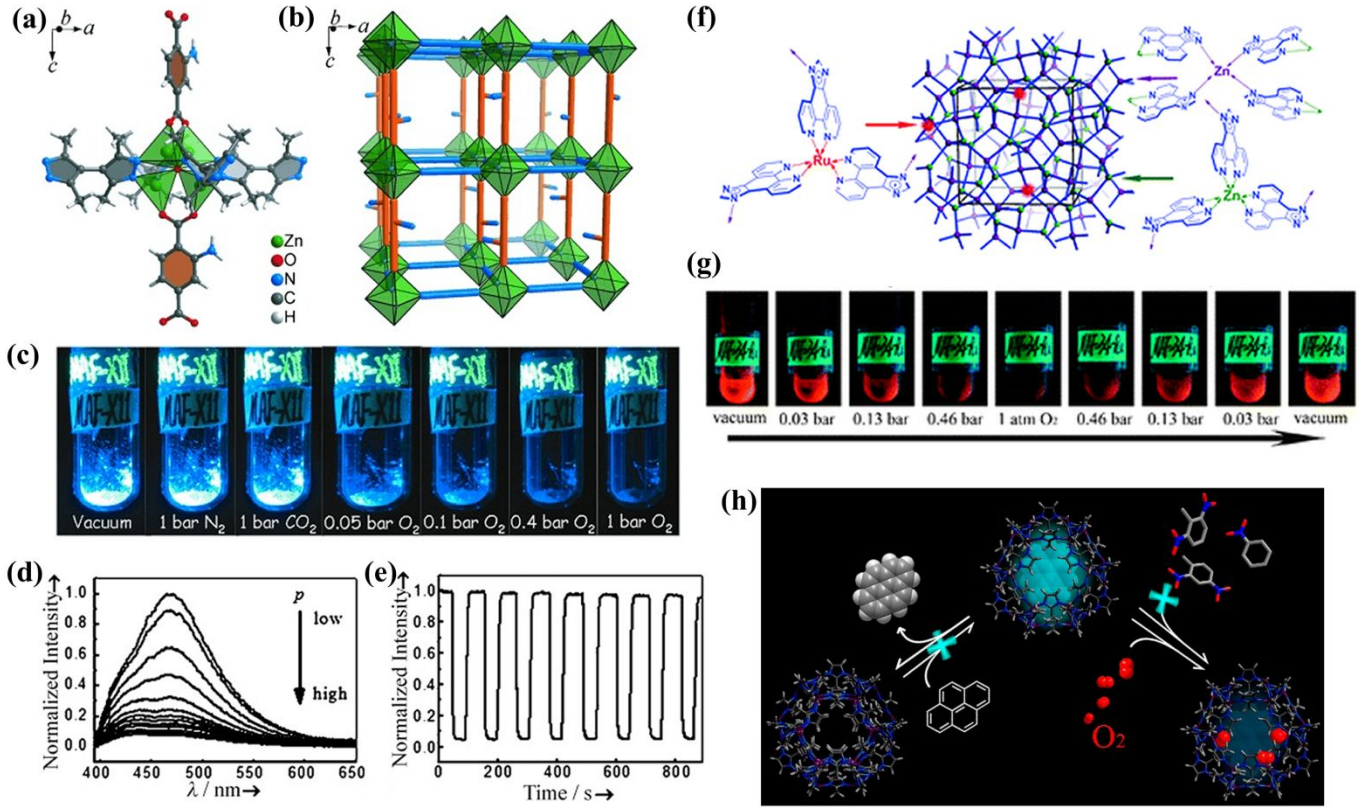

Fig. 9 (a) The $\{Zn_4O(Rpz)_4(RCOO)_2\}$ cluster. (b) A simplified view of the 3D framework structure. (c) Photographs of compound in different gas atmospheres after exposure to 365 nm UV light. (d) Emission spectra recorded at different O_2 pressures (excitation at 345 nm). (e) Reversible quenching/recovery of luminescence of compound upon alternating exposure to O_2 and a vacuum. Reproduced with permission from ref. 131. Copyright 2013, John Wiley and Sons. (f) Doping the MAF-34 host matrix with Ru^{2+}. (g) Photographs of 0.16 Ru:MAF-340 under the sequentially changing O_2 atmospheric pressure (under a 365 nm UV light). Reproduced with permission from ref. 132. Copyright 2013, Royal Society of Chemistry. (h) Encapsulating pyrene in MAF-4 as an optical sensor of molecular oxygen. Reproduced with permission from ref. 85. Copyright 2015, American Chemical Society.

the O_2 sensor (Fig. 9h). The pyrene@MAF-4 selectively allows the oxygen molecules to enter the framework and react with the encapsulated guest pyrene molecules. Moreover, pyrene@MAF-4 is easy to fabricate as a thin film that also maintains the good oxygen sensing property.

A porous Cu^+-based MOF [Cu(detz)] (MAF-2, Hdetz = 3,5-diethyl-1,2,4-trizole) was investigated by Chen et al[136], which is the first Cu^+-based PCP displaying an optical oxygen-sensing property. The Cu^+-based PCPs show good water stability, an excellent phosphorescent lifetime as long as 115.9 (2) μs, which surpasses most luminescent dye-based oxygen sensors, and considerable oxygen permeability under ambient conditions, indicating that MAF-2 is a good oxygen sensor. The luminescence quenching efficiency is as high as 99.7% at 1 bar of O_2, and no luminescence was lost after more than 10 cycles, indicating the good photochemical stability and excellent reversibility. Inspired by this work, a few interesting Cu^+-based MOFs for oxygen sensing applications were studied [137-140].

Lanthanide MOFs are a prime candidate sensor material due to their excellent luminescent properties and high sensitivity to stimuli in the surrounding environment[122,141-144]. Qian et al. investigated two Tb-based LMOF films, CPM-5⊃Tb^{3+} and MIL-100(In)⊃Tb^{3+} ($[(CH_3)_2NH_2][In_3O(BTC)_2(H_2O)_3]_2[In_3(BTC)_4]$, CPM-5; $In_3O(OH)(H_2O)_2[BTC]_2$; MIL-100(In))[122], which were constructed using the postfunctionalization method. Both films display ultrafast and reversible detection of O_2, but the MIL-100(In)⊃Tb^{3+} films show higher sensitivity, with a short response/recovery time and higher oxygen sensitivity (K_{SV} = 7.59, Fig. 10b). The interaction between the suspended carboxylic acid and terbium ion incorporated in MIL-100(In)⊃Tb^{3+} improve the energy transfer efficiency (Fig. 10a). Rosi et al. also fabricated LMOFs, $[Zn_8(ad)_4(BPDC)_6O•2(Me_2NH_2)•8DMF•11H_2O]$ (bio-MOF-1, ad = adeninate; BPDC = biphenyldicarboxylate)[141]. Ln^{3+}@bio-MOF-1 was obtained through a further cation exchange reaction with different

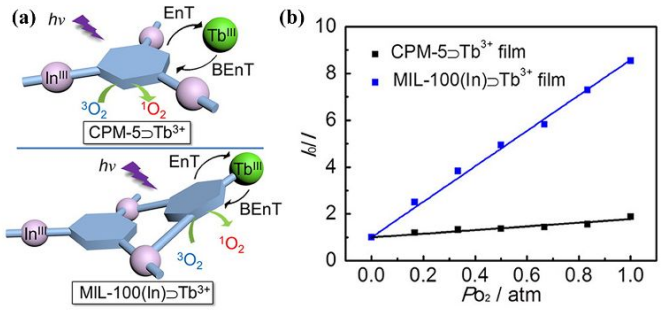

Fig. 10 (a) Energy transfer processes and O_2 quenching processes of CPM-5⊃Tb^{3+} and MIL-100(In)⊃Tb^{3+}. (b) Stern-Volmer plots showing I_0/I vs oxygen partial pressure P_{O_2} for the activated MOF films. Bio-MOF-1 encapsulation and sensitization of lanthanide cations. Reproduced with permission from ref. 122. Copyright 2014, American Chemical Society.

ions, such as Tb^{3+}, Sm^{3+}, Eu^{3+}, or Yb^{3+}. Yb^{3+}@bio-MOF-1 displays NIR emission and the MOF effectively serves as an antenna for sensitizing the lanthanide cation. Yb^{3+}@bio-MOF- 1 responds to the presence of O_2 gas with an approximately 40% decrease in the luminescence signal. Notably, the oxygen sensor displays good reversibility because no decrease in the luminescent intensity is observed after alternating exposure to O_2 and N_2 for several cycles.

Recently, a few new types of MOFs have been reported to function as sensor materials. Zang et al. creatively combined the silver(I) chalcogenide/chalcogenolate clusters (SCCs) with a metal-organic framework to construct rigid SCC-based MOFs (SCC-MOFs) $[(Ag_{12}(S^tBu)_8(CF_3COO)_4(bpy)_4)]_n$ (Ag_{12}bpy, bpy = 4,4′-bipyridine)[90] (Fig. 11a). SCC-MOFs successfully solve the inherent instability and poor room-temperature luminescence quantum yield of SCCs by assembling of SCCs and rigid organic ligands. The SCCs remain stable in air for more than one year and the RT quantum yield shows an approximately 60-fold increase to reach 12.1%, which is ascribed to the effective reduction of the non-radiative decay process for the high structural rigidity of the framework and the ordered arrangement of chromophores. Importantly, Ag_{12}bpy functions as an ultrafast visual fluorescence turn-off oxygen sensor. As shown in Fig. 11b, a fast fluorescence on/off process between the nonemissive (off) state and bright green emission (on) state was achieved by exposing Ag_{12}bpy to alternating air/vacuum conditions. At 21 kPa of O_2 pressure, the luminescent intensity is quenched by as much as 93.6% and the LOD is as low as 32 Pa with 1% quenching. The response time was less than 1 s and the luminescent response can undergo more than 100 cycles without an obvious loss of performance (Fig. 11c and d). The subsequent mechanistic study revealed that the highly permeable channels for O_2 of framework allow free access to molecular O_2 and weak interactions permit molecular O_2 to efficiently interact with the excited electronic state and transfer its energy.

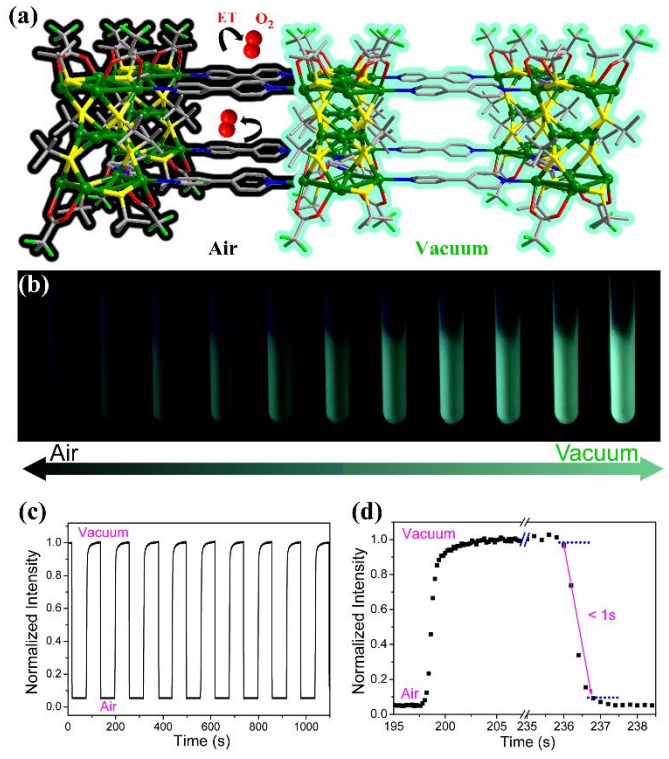

Fig. 11 (a) The structure of Ag_{12}bpy. Ag, green; C, grey; O, red; S, yellow; F, turquoise. H atoms are omitted for clarity. ET = Energy Transfer. (b) Photographs of Ag_{12}bpy excited by a 365 nm light in a glass tube from a vacuum to air. (c) Reversible luminescence during on–off cycles under alternating exposure to air/vacuum for Ag_{12}bpy. (d) Enlargement of the response transient curves of Ag_{12}bpy in air. The air-quenching response time was less than 1 s (the response time is defined as the time corresponding to a 90% decrease in emission intensity when the gas phase is changed from vacuum to air). Reproduced with permission from ref. 90. Copyright 2017, Springer Nature.

3.2 Water Vapor Sensing

Water is an important element that is closely related to almost all conditions required to sustain human life. Water vapor in the atmosphere affects the physical, chemical and biological processes of the natural environment. Humidity affects the thermal, electrical and optical transmission characteristics of gases. Water sensors are widely applied in chemical industrial processes, environmental monitoring, food inspection, and pharmaceutical processes. Thus, an easy, rapid and highly sensitive water sensor is indispensable.

Magnetic MOF-based water sensors have been widely studied in the past few years[72,74,103-107,145-150]. Ohkoshi et al. presented a cyanido-bridged bimetal MOF[72], $\{[Dy^{III}(H_2O)_2][Co^{III}(CN)_6]\}\cdot 2.2H_2O$, and it undergoes a SCSC transformation upon dehydration to generate its dehydrated form of $\{Dy^{III}[Co^{III}(CN)_6]\}$ (Fig. 12a). Both compounds are composed of two alternately arranged metal centres with different magnetic properties for paramagnetic Dy^{3+} centres and diamagnetic hexacyanidocobaltate(III). Upon dehydration and rehydration, a substantial change in the coordination geometry from eight-coordinated square antiprism geometry to the six-coordinated trigonal prism geometry of Dy^{3+} occurs. This reversible change in coordination geometry results in a switch in the SMM behaviour. The hydrated compound does not show SMM behaviour due to the lack of magnetic interactions,

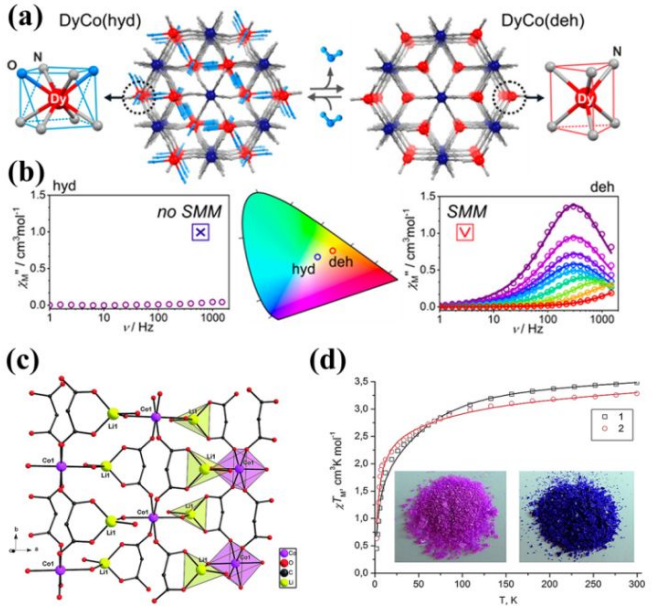

Fig. 12 Crystal structure (a) and single-molecule magnet behavior (b) of Co-MOF and dehydration compounds. Reproduced with permission from ref. 72. Copyright 2019, American Chemical Society. (c). Fragment of the 2D layer of $[Li_2Co(H_2O)_4(Me_2MaI)_2]_n$. (d). The magnet and color changing of $[Li_2Co(H_2O)_4(Me_2MaI)_2]_n$. Reproduced with permission from ref. 147. Copyright 2017, John Wiley and Sons.

while the dehydrated compound displays the SMM property arising from the single-ion anisotropy of the incorporated Dy^{3+} complexes (Fig. 12b). Zhou et al. synthesized eight MOFs based on copper(II) tetrazolate-5-carboxylate (tzc) with 1,3-di(4-pyridyl)propane as the ligand, and these MOFs display solvent-mediated, temperature-induced phase transitions[74]. All crystal structures show the same framework topology and the same octahedral geometry of Cu^{2+} centre; thus, the $Cu^{2+}\cdots Cu^{2+}$ connected to the tzc ligand builds the proper pathway to tune the magnetic properties. Importantly, the switching between ferro- and antiferromagnetic coupling was achieved for subtle guest-induced structural changes accompanying the structural phase transitions. Zorina-Tikhonova et al. reported a Co-MOF $[Li_2Co(H_2O)_4(Me_2Mal)_2]_n$ (Li_2Me_2Mal = lithium dimethylmalonate), which shows an interesting reversible dehydration/rehydration process with a distinct reversible colour change between pink and violet[147]. Interestingly, accompanying the dehydration/rehydration process, the magnetic susceptibility χ_M displays a reversible response, and the magnetic. The change in the magnetic properties is directly related to the cleavage of coordinated bonds of guest molecules, alters the Co^{2+} coordination environment susceptibility of dehydrated compounds is decreased approximately 6% (Fig. 12c and d)

Ferroelectric MOF-based water sensors are based on changing the polarity of the MOF through the loss of coordinated or guest water molecules[75,76,151]. Zang et al. investigated a polar chiral Co-MOF, $Co_2(L)$-(bpe)$(H_2O)\}\cdot 5H_2O]_n$ (H_4L = N-(1,3-dicarboxy-5-benzyl)carboxymethylglycine, bpe = 1,3-bis(4-pyridyl)ethane)[75]. The MOF contains two interesting coaxial double-helical chains, induces the formation of helical bpe and helical H-bonded water columns, and undergoes a two-step fast and reversible SCSC transformation. The MOF displays excellent spontaneous polarization and ferroelectric properties induced by the characteristic polar infinitely hydrogen bonded water molecules. In the first step of the SCSC transformation, the ferroelectric switch is achieved by the desorption/adsorption of free polar water molecules. The second step of the SCSC transformation includes the removal/uptake of coordinating water molecules, which changes the coordination mode of the cobalt centre from octahedral to trigonal bipyramidal, resulting in a change in the colour from red to dark brown. Additionally, these two-step SCSC transformations are fast and reversible (Fig. 13a-c). Thus, this MOF is an excellent bifunctional water sensor with ferroelectric and optical colour properties.

Li et al. reported an indium MOF material with guest water molecules in the nanochannels that endows the MOF with a ferroelectric property[151]. Upon changes in the sample temperature, the hydrogen-bonding interactions are destroyed, and the guest water molecules are removed, thus significantly altering the ferroelectric properties of the MOF. Natarajan et al. prepared a Co-MOF, $[H_3O][Co_2(dat)(sdba)_2]\cdot H_2sdba\cdot 5H_2O$ (dat = 3,5-diamino-1,2,4-triazole; H_2sdba = 4,4′-sulfonyldibenzoic acid)[76], which crystallizes in the noncentrosymmetric space group $P_{na}2_1$. The MOF shows an interesting ferroelectric property that may originate from the formation of an electric dipole due to the obvious charge separation inside the structure (Fig. 13d-g). The hydrogen bonds between water molecules and the host framework tune the dipoles. In addition, the loss of water molecules will destroy the hydrogen bond interactions, resulting in the disappearance of the ferroelectric property.

Colorimetric water sensors have been investigated by some groups[110-112,152,153]. Bu et al. prepared blue block Co-based MOF with the formula of $[Co_{1.5}(tipb)(SO_4)(pta)_{0.5}]\cdot(DMF)_{1.7}$ (1,3,5-tris(pimidazol-ylphenyl)benzene = tipb, terephthalic acid = H_2pta)[110]. The MOF undergoes a reversible SCSC transformation to form a red crystal with the formula of $[Co_{1.5}(tipb)(SO_4)(H_2O)_{3.6}]\cdot(pta)_{0.5}$ (solvent)$_n$. The colour changes in the MOF are caused by the coordinated configuration of the Co^{2+} ions changing from a four-coordinate tetrahedral coordination geometry to a six-coordinate octahedron coordination geometry. The reversible response of the MOF to water makes it a good choice as a colorimetric water-sensing material. Allendorf et al.

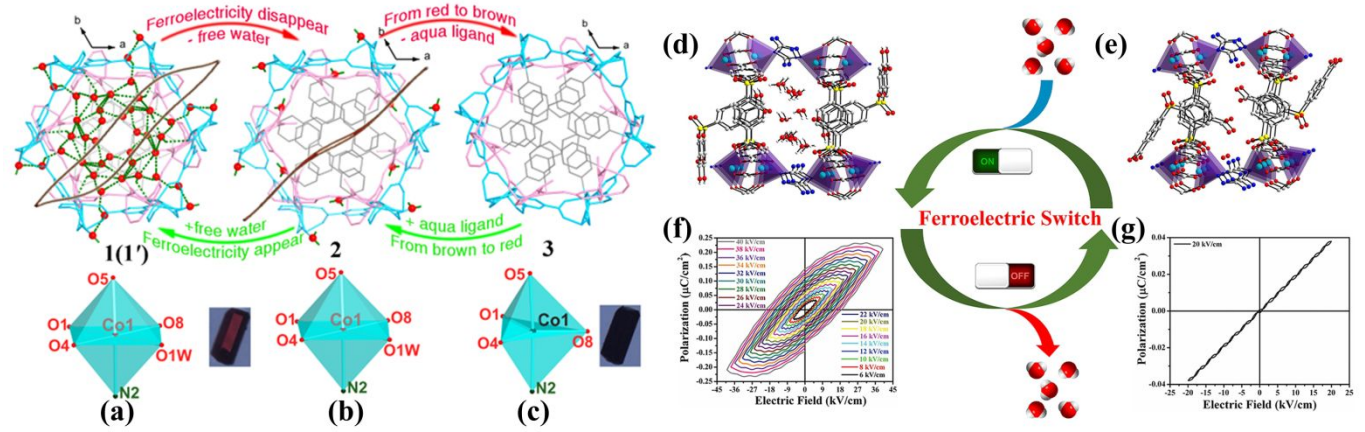

Fig. 13 Schematic representation of the two-step reversible SCSC transformation between compounds 1, 2, and 3 and concomitant changes in the structures and properties; H_2O molecules are shown as large red spheres; hydrogen bonds are indicated by green dashed lines. The first step (1–2–1′) in the transformation between structures (a) and (b) involves the desorption/adsorption of free water molecules and disappearance/appearance of ferroelectricity. The coordination environment of Co^{2+} and colour of the single crystal remain unchanged. The second step [2–3–(2′)1′] in the transformation between structures (b) and (c) involves the desorption/adsorption of aqua ligands, transformation of coordination environment of Co1 from octahedral to trigonal bipyramidal, and change in the colour of the single crystal from red to dark brown. Reproduced with permission from ref. 75. Copyright 2013, American Chemical Society. The structures of the parent compound (d) and the dehydrated compound (e) are shown. (f) The electric hysteresis loops (P–E curves) for the as-synthesized compound under different applied electric fields. (g) P–E curve for the dehydrated compound. Reproduced with permission from ref. 76. Copyright 2016, John Wiley and Sons.

synthesized $Cu_3(BTC)_2$ (also known as HKUST-1, H_3BTC = 1,3,5-benzenetricarboxylate)-based thin films using the spin coating method, and these films functioned as a colorimetric water sensor[112]. The mechanism underlying the colour change is attributed to the alterations in the d-d transitions by the coordinated interaction between water and the paddlewheel metal centre. Hatakeyama et al. prepared a copper-based 3D-MOF $[Cu(HL)(DMSO)\cdot(MeOH)]_n$ (H_3L = triphosphaazatriangulene) that facilitates the reversible stimuli-responsive SCSC transformation[152]. The MOF can transform to a 1D-columnar assembled material $H_3L\cdot0.5[Cu_2\text{-}(OH)_4\cdot6H_2O]\cdot4H_2O$ upon stimulation with water guest molecules. When the MOF is exposed to water, the colour of the crystal slowly changes from yellow to blue-green, resulting from the coordination of the H_2O molecules by the Cu^{2+} centre and the phosphonate groups, while the coordinated DMSO molecules and phosphonate groups in the MOF are cleaved from the Cu^{2+} centre. Furthermore, stimuli-responsive transformations are reversible, even within the single crystal, upon exposure to DMSO/MeOH or H_2O vapor.

LMOF-based water vapor sensors are the most widely studied sensors[84,154-165]. Su et al. reported a microporous Zn-MOF ($Zn(hpi_2cf)(DMF)(H_2O)$, LIFM-CL1-H_2O, H_2hpi_2cf = (5-(2-(5-fluoro-2-hydroxyphenyl)-4,5-bis(4-fluorophenyl)-1H-imidazol-1-yl)isophthalic acid))[84]. The ligand displays a characteristic excited state intramolecular proton transfer (ESIPT). Interestingly, the Zn-MOF undergoes a reversible water-driven SCSC structural transformation under extremely facile conditions (blown with dry gas or moderate heating at 70 °C). The reversible cleavage/formation of coordinating bonds of water molecules changes the intramolecular H-bonding interactions and turns the ligand ESIPT process on or off, resulting in a distinct shift in the emission from blue at 463 nm to a cyan colour at 493 nm (Fig. 14). The gas blowing test indicated that the blue emission rapidly shifts to a cyan colour in a matter of seconds when blowing dry gases, and the colour is easily restored upon exposure to wet gases or air. The MOF films are blown through pure N_2 gas and further indicate the emission change accompanying the water release/uptake processes. In particular, Zn-MOF displays excellent selectivity towards water in the presence of interference from any other small molecules. Based on these results, Zn-MOF is a convenient, ultrafast, and selective luminescent water-sensing material.

Chi et al. used europium metal–organic frameworks (Eu-MOF, $[Ln(btc)(H_2O)]\cdot$guest) with red light-emitting and encapsulated blue light-emitting nitrogen and sulfur-codoped carbon-based dots (N,S-CDs)[154]. When the Eu-MOFs/N,S-CDs were dispersed in water, the blue emission of encapsulated N,S-CDs appeared due to release into the solution and the emission of Eu-MOF is quenched by the host-guest interaction. Thus, the different fluorescent responses of two chromophore upon exposure to water indicates that Eu-MOFs/N,S-CDs represents a good ratiometric sensor of water. Another ratiometric fluorescence sensor of water was achieved by Yin et al[155]. The authors used a simple one-pot method and successfully constructed a guest-encapsulated MOF, Ru@MIL–NH_2. Dual emission peaks at 465 and 615 nm were attributed to BDC–NH_2 and $Ru(bpy)_3^{2+}$, respectively. Interestingly, Ru@MIL–NH_2 displays the ratiometric fluorescence sensing of water through the stepwise increase in the emission at 465 nm and the unchanged emission at

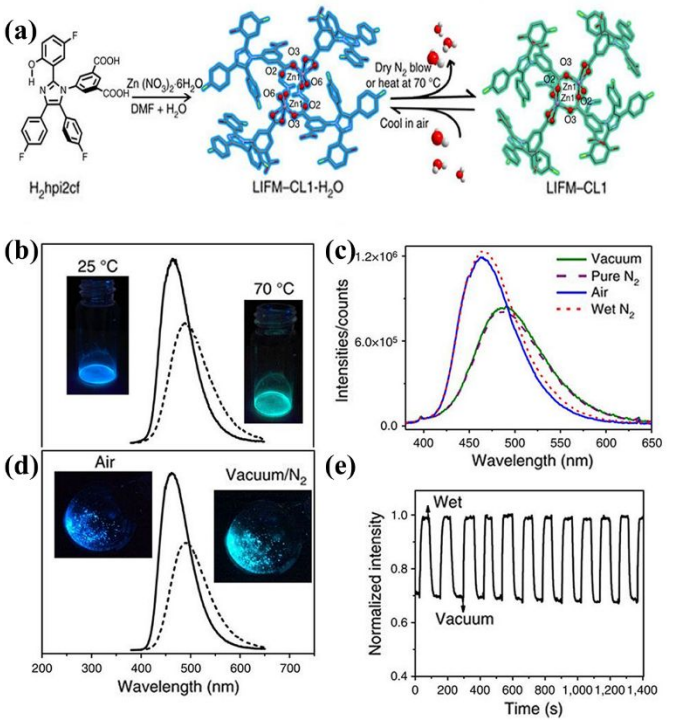

Fig. 14 (a) Ligand, hydrated LIFM-CL1-H_2O (blue) and dehydrated LIFM-CL1 (cyan), showing coordination environmental change around Zn centres. (b-d) PL emission spectra and photographs of hydrated LIFM-CL1-H_2O and dehydrated LIFM-CL1 tuned by heating, gases and vacuum, showing PL switch between blue E-emission and cyan K-emission based on ESIPT process of ligand H_2hpi_2cf. (e) Time-dependent PL intensity cycles between LIFM-CL1 and LIFM-CL1-H2O microcrystals under vacuum and 1 bar air (RH = 45%) at 25 °C (λ_{ex} = 365 and λ_{em} = 463 nm). Reproduced with permission from ref. 84. Copyright 2017, Springer Nature.

615 nm. Further mechanistic studies revealed that BDC–NH_2 is susceptible to water due to the ease of protonation of the nitrogen atom and change in the energy of the π-conjugate system of Ru@MIL–NH_2 to result in a change in emission.

Yuan et al. constructed a Tb^{3+}/Eu^{3+} mixed-lanthanide MOF **$Tb_{97.11}Eu_{2.89}$-L1** (H_6L1 = (4-carboxylatophenoxy)cyclotriphosphazene) capable of the ratiometric detection of trace amounts of water in CH_3CN[157]. As the water content increases from 0% to 2.5% (v/v%), the characteristic luminescence of Eu^{3+} and Tb^{3+} exhibits different responses and variable colour changes in **$Tb_{97.11}Eu_{2.89}$-L1**. Additionally, the colour response of **$Tb_{97.11}Eu_{2.89}$-L1** occurs in only a few seconds for the hydrophilic cavity of **$Tb_{97.11}Eu_{2.89}$-L1**, and the reversible fluorescence colour change process is achieved by absorbing/releasing water molecules. Manos et al. reported a Mg^{2+} MOF $[Mg(H_2dhtp)(H_2O)_2]\cdot$DMAc, (AEMOF-1 = alkaline earth MOF-1; H_4dhtp = 2,5-dihydroxy-terepthalic acid)[158]. Remarkably, the guest DMAC is removed under facile conditions and the guest-free MOF rapidly detects trace amounts of water (0.05–5% v/v) in different organic solvents through a luminescence light-on sensing mechanism.

Some interesting MOFs based other properties for water vapor detection have been investigated, including mass change (quartz crystal microbalances)[166-168], impedance[169-172], capacitance[173,174], dielectric properties[175]. Wagner et al. investigated three CAU-10-type MOFs (CAU-10-H/S = $[Al(OH)(m\text{-BDC-H})_{0.76}(m\text{-BDC-SO}_3H)_{0.24}]\cdot 1.5\,H_2O\cdot 0.2$ DMF; CAU-10-N/S = $[Al(OH)(m\text{-BDC-NO}_2)_{0.79}(m$-BDC-

$SO_3H)_{0.21}$] · 2.93 H_2O; CAU-10-O/S = [Al(OH)(*m*-BDC-OH)$_{0.89}$(*m*-BDC-$SO_3H)_{0.11}$] · 4.7H_2O, H_2BDC = 1,3-benzenedicarboxylic acid) that function as excellent impedance-based humidity sensors[171]. The CAU-10-N/S was further studied in an air environment to estimate the sensing application potential. The MOF-based humidity sensor displays comparable sensing properties to a commonly used commercial humidity sensor.

3.3 Toxic Industrial Gases Sensing

Toxic industrial gases such as H_2S, SO_2, NH_3, CO, NO, and NO_2 are destructive to the environment and human health. Thus, the detection of these destructive gases or vapors is a significant component of air quality monitoring.

3.3.1 Hydrogen Sulfide

Hydrogen sulfide (H_2S) is a poisonous gas with no colour and a rotten egg smell. On the one hand, H_2S is a dangerous industrial pollutant that forms an explosive mixture in the air and might explode upon exposure to open flames or high temperatures[176,177]. On the other hand, H_2S gas, nitric oxide (NO) and carbon monoxide (CO) have been recognized as the three largest biological messengers in the human body. The normal concentration of H_2S gas in many organizations and human plasma is approximately 50 μmol/L, and abnormal H_2S production in the human body will increase the incidence of Alzheimer's disease, cancer, and diabetes complications. The H_2S sensor is useful and desperately needed.

Due to the rapid development of EC-MOFs, chemiresistive MOF-based sensors have become the research hotspot[93,94]. Mirica et al. exploited an easy and fast method for preparing multifunctional electronic textiles (e-textiles) based on conductive MOFs Ni-CAT (Ni-CAT was constructed by 2,3,6,7,10,11-hexahydroxytriphenylene (HHTP) ligand, and contains two different types of stacked layers, one layer is an extended honeycomb structure, the other layer is composed of the discrete units[178]) or $Ni_3(HITP)_2$ (HATP = 2,3,6,7,10,11-hexaaminotriphenylene)[93], representing the first use of direct self-assembly to combine the conductive MOFs and textiles. The MOF-based e-textiles display several unique characteristics, such as enhanced porosity by combing the mesoporous feature of the textile and microporous characteristic of conductive MOF, excellent flexibility, thermal stability, and wash ability (in water and acetone) (Fig. 15a and b). Furthermore, the conductivity and gas-sensing capability were retained, and the self-organized frameworks on textiles (SOFT) devices function as chemiresistive sensors for sensing the toxic gaseous analytes H_2S and NO at ppm levels, retain their

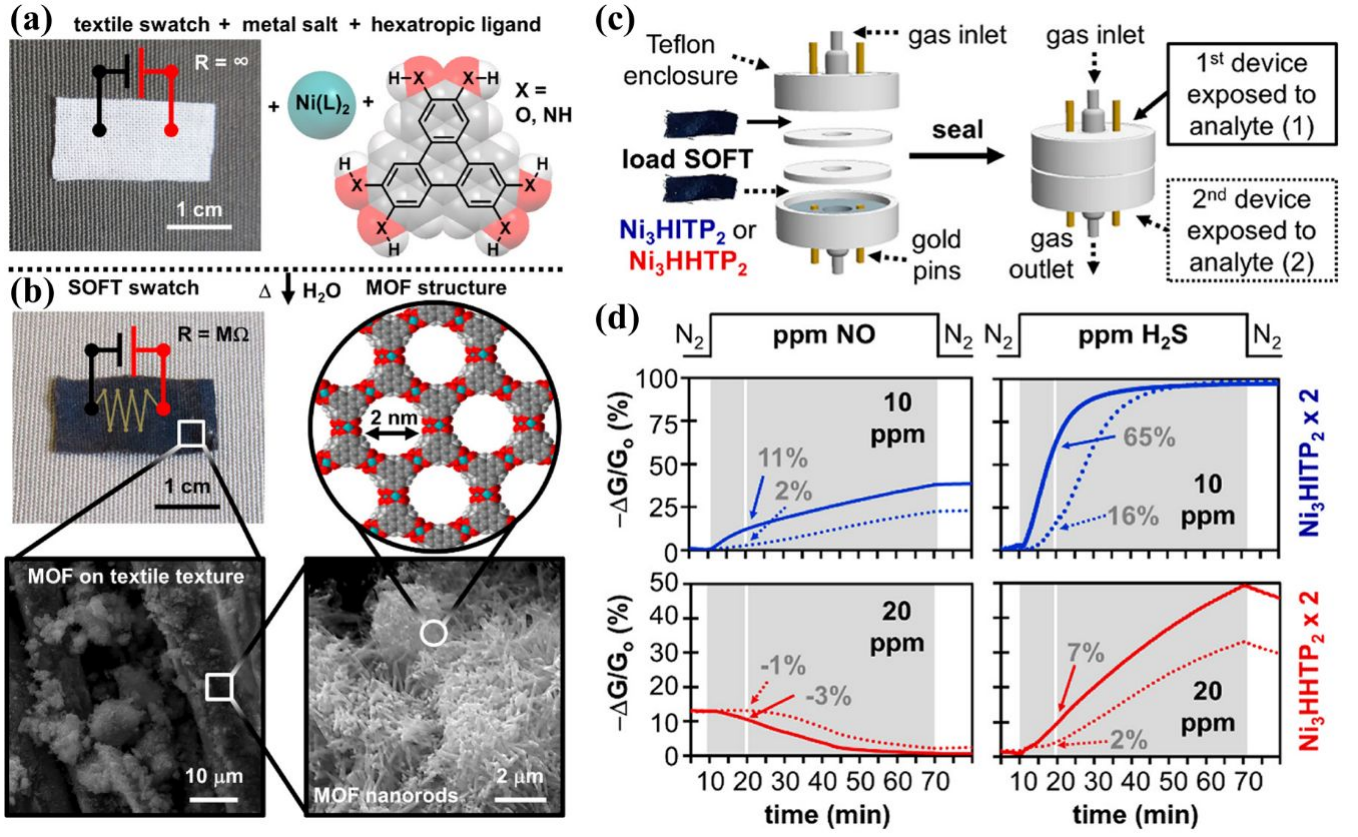

Fig. 15 Fabrication of MOF devices and sheet resistance of SOFT sensor devices. (a) Starting materials for SOFT-sensors from organic triphenylene-based ligand (HHTP or HATP), metallic node (Ni-$(OAc)_2$ or $NiCl_2$), and fabric swatch (cotton shows no conductivity). Photograph of cotton swatch is shown. (b) Solvothermal condensation of these reagents in water produces conductive SOFT devices: textiles coated with nanoporous MOF. Macroscopic through molecular level detail is shown, from a photograph of cotton SOFT sensor postreaction (top left), to scanning electron micrographs detailing MOF coating on fibers (bottom left), and characteristic MOF nanorod texture (bottom right), to space-filling model of MOF (top right). Breakthrough studies for simultaneous detection and capture of analytes. (c) Custom Teflon enclosure used to determine membrane breakthrough for SOFT-devices. Two devices are loaded such that the diameter of the inner bore for gas flow is completely covered by SOFT-devices. Spring loaded gold pins immobilize the sensors and serve as electrodes. The enclosure is then completely sealed for leak-free flow. (d) Representative breakthrough sensing traces for SOFT-devices. The first device exposed to analyte is represented by a solid line, the second device by a dashed line. The delayed response of the second device reflects gas capture by the first device. Reproduced with permission from ref. 93. Copyright 2017, American Chemical Society.

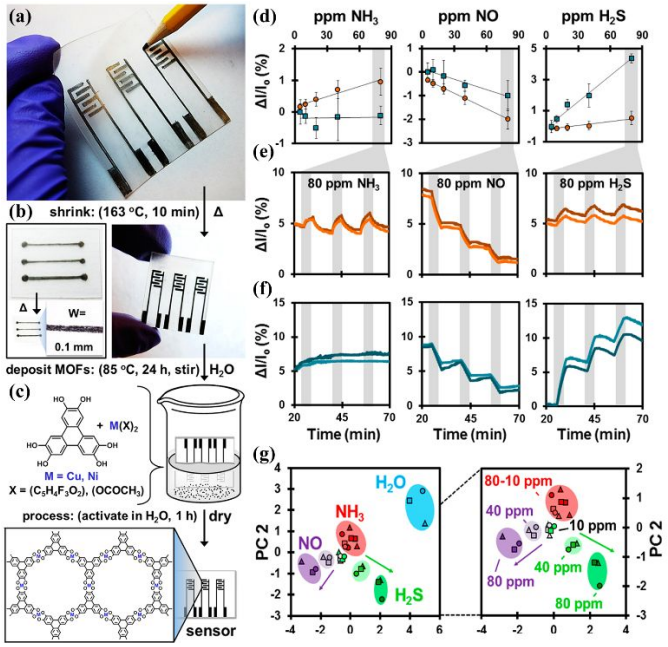

Fig. 16. Stepwise methodology for the fabrication of MOF-based chemiresistors on shrinkable polymer films equipped with graphitic electrodes. (a) Photograph showing the process of drawing electrodes on a shrinkable polymeric film with a commercial HB pencil. (b) Shrinking of the film (10 min, 163 °C) miniaturizes lateral features of the electrodes (W = wire width). (c) Templated growth of MOFs into the device. (d) Concentration dependent sensing response (left to right, NH_3, NO, and H_2S) for Cu_3HHTP_2 and Ni-CAT orange and blue, respectively. Error bars represent standard deviation from average exposures (3 × 80 ppm, 9 devices). (e) Representative sensing traces (3 × 80 ppm) for Cu_3HHTP_2 and (f) representative traces (3 × 80 ppm) for Ni-CAT. (g) Principal component analysis demonstrating differentiation of analytes (3 arrays, 2 sensors each); NH_3 shown in red, NO in purple, H_2S in green, and H_2O in blue, whereas Array #1 markers are circular, Array #2 are square, and Array #3 are triangular. Right Expanded detail of quantitative array responses to NH_3, H_2S, and NO. Reproduced with permission from ref. 94. Copyright 2016, American Chemical Society.

performance in 18% relative humidity (RH) and are completely recoverable and washable. Moreover, the theoretical LOD of Ni_3HITP_2 and Ni-CAT for H_2S (1–80 ppm) were 0.52 and 0.23 ppm, respectively (Fig. 15c and d). The chemiresistive gas-sensing property may be attributed to the charge transport mechanism caused by the host–guest interactions.

Mirica et al. established a fast and simple method for fabricating of chemiresistive sensors[94]; they utilized two conductive MOFs Cu_3HHTP_2 and Ni-CAT, and performed direct self-assembly of MOFs on shrinkable films (Fig. 16a-c). The sensors are able to detect different gases, such as H_2S, NH_3, and NO, at the ppm level. After exposure to H_2S, an increase in resistivity was obtained for Cu_3HHTP_2 by 0.5 ± 0.3% and $_2$ by 4.2 ± 1.0% (Fig. 16d-g). This study describes a new method to rapidly fabricate MOF-based chemiresistive sensors and expand the utility of sensors.

An interesting colorimetric sensor of H_2S was investigated by Xu et al[114]. An amphoteric MOF $Pb_6O_2(C_{69}H_{48}O_{12}S_4)_2(DMA)_3(H_2O)_2$ (DMA=N,N-dimethylacetamide) was prepared using a backfolded molecule (pentaeryhritol tetra-2-(4-ethynylphenyl)methylsulfane-*p*-methyl benzoic acid) and Pb^{2+} ions. The MOF combines distinct donor (free-standing sulfur) and acceptor (labile capped Pb^{2+} centres) characteristics, which endows it with the ability to effectively sense both Lewis acid and Lewis base guests (such as $PdCl_2$ and H_2S). Upon exposure to H_2S gas, the colour of MOFs immediately changes from yellow to dark red, due to the binding of H_2S species as a strong electron donor onto the Pb centres. The distinct colour changes of MOFs in response to H_2S binding indicate their potential utility in sensing applications.

H_2S as an electron donor reacts with MOF to cause a colour change in the MOF and alter the luminescence of the MOF[179-197]. Qian et al. used flexible MOF-based mixed-matrix membranes (MMMs) as a sensor for hydrogen sulfide with a fluorescent turn-on mechanism[179]. For the first time, MOFs and polymers were

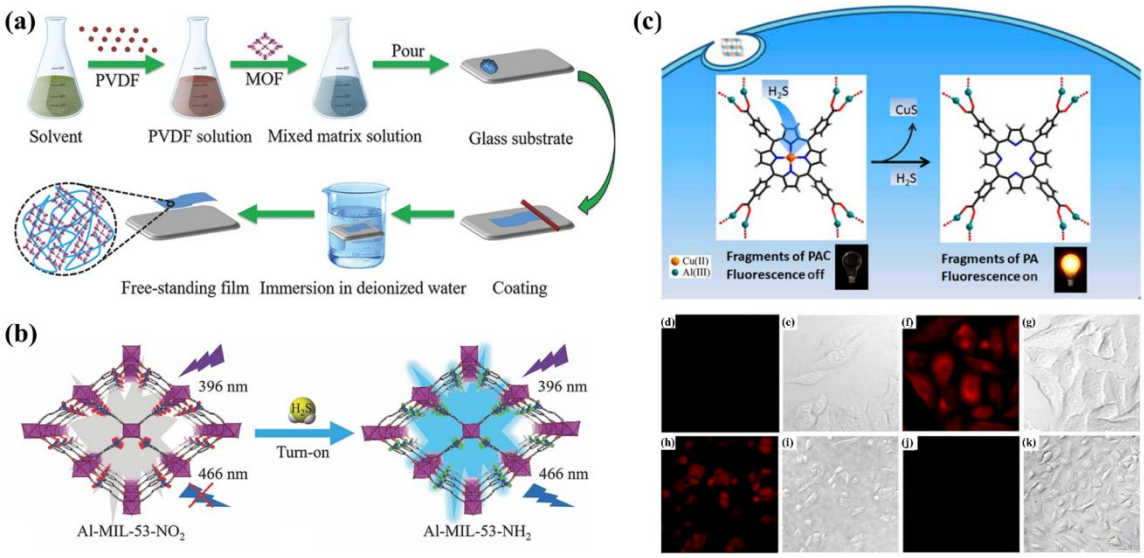

Fig. 17 (a) Process for formation of MMMs. (b) Illustration of nitro (-NO_2)-functionalized MOF as a fluorescence based turn-on probe for H_2S. Reproduced with permission from ref. 179. Copyright 2018, John Wiley and Sons. (c) Structural fragment of nano-MOF PAC and the proposed strategy for fluorescent variation of PAC upon reactive metal centers (Cu^{2+} ions) as the H_2S-responding site. The corresponding product is referred to as luminophor nano-MOF PA. Confocal fluorescence images in living cells: (d) image of HepG2 cells incubated with 10 μM PAC; (e) bright-field image of (d); (f) image of HepG2 cells incubated with 10 μM PAC and 50 μM NaHS; (g) bright-field image of (d); (f) image of A549 cells incubated with 500 μM SNP and 10 μM PAC; (i) bright-field image of (h); (j) image of A549 cells incubated with 250 mg·L^{-1} PPG and 10 μM PAC; (k) bright field image of (i). Reproduced with permission from ref. 180. Copyright 2014, American Chemical Society.

combined into MMMs to construct sensors (Fig. 17a). Nanocrystals of Al-MIL-53-NO_2 were synthesized using the solovothermal method with 2-nitroterephthalic acid ligands; these noncoordinated -NO_2 groups point towards the channels and endow MOFs with the ability to sense H_2S through a reaction with -NO_2 groups and H_2S. Al-MIL-53-NO_2 displays very weak fluorescence due to the presence of the electron-withdrawing nitro groups. After H_2S reduces the nitro groups to amine functionalities, Al-MIL-53-NH_2 shows bright blue emission (Fig. 17b). The MMMs sensor shows an excellent detection selectivity and sensitivity for H_2S, with a low detection limit of 92.31 × 10^{-9} M. Ghosh et al. also reported nitro (-NO_2)-functionalized MOF that functions as a fluorescence light-on probe for sensing H_2S through interactions between nitro groups and H_2S[196]. Tang et al. presented a porous porphyrin-based MOF {CuL-$[AlOH]_2$}$_n$ (H_6L = *meso*-tetrakis(4-carboxylphenyl)porphyrin)[180]. Interestingly, the presence of paramagnetic Cu^{2+} ions connected to the organic ligand completely quenched the ligand-based fluorescence (Fig. 17c). In addition, the exposure of the MOF to H_2S immediately increased the luminescence of the ligand by removing Cu^{2+} ions from the porphyrin centres. More importantly, the probe functions in aqueous solutions buffered at physiological pH (pH 7.4) through a light-on sensing mechanism with a detection limit of 16 nM. Due to the sensing property at physiological pH, biological imaging in living cells was performed (Fig. 17d-k). Increases in intracellular fluorescence were observed in both aHepG2 cells and A549 cells, indicating that the MOF probe was capable of sensing H_2S in living cells. The same sensing mechanism was reported by the Qian and Gao laboratories[181,182].

The H_2S chemicapacitive sensor and cataluminescence sensor have been studied in recent years[198,199]. Eddaoudi et al. fabricated rare-earth (RE)-based MOFs with the **fcu** topology (fum-**fcu**-MOF, $[(CH_3)_2NH_2]_2[RE_6(\mu_3\text{-}OH)_8(FUM)_6(H_2O)_6]$, RE, i.e., Eu^{3+}, Tb^{3+}, and Y^{3+}, FUM = fumarate) and then constructed a MOF-based sensor through the *in situ* growth of the MOF thin film on capacitive interdigitated electrodes (IDEs) (Fig. 18a)[198]. Next, the sensing properties were investigated in the presence of various gases/vapors, including CH_4, NO_2, H_2, toluene (C_7H_8), and H_2S. Fortunately, the MOF sensors displayed an excellent detection H_2S with the capacitive response, and the MOF sensors have the ability to detect H_2S at concentrations ranging from 1 to 100 ppm with a linear response (Fig. 18b and c).

Most interestingly, the sensor displayed a distinctive detection sensitivity for H_2S, with a detection limit as low as 5 ppb. Excellent stability of the sensor for sensing H_2S at room temperature was achieved; the reproducibility experiments indicated the stable detection of H_2S at 1 ppm and 10 ppm for more than three months. The reproducibility cycling experiments revealed the excellent stability over a range of different cycles. The experiments comparing this framework with other types of MOF (fum-fcu-MOF, ZIF-8, and Cu(bdc)·xH_2O)-coated sensors indicate that fum-**fcu**-MOF is more stable than other types of MOFs, such as ZIF-8 and Cu(bdc)·xH_2O. The high stability of fum-**fcu**-MOF derived from the stable RE hexanuclear cluster assembly with rigid linkers prevents the formation of a metal sulfide. The H_2S selectivity of the fum-**fcu**-MOF sensor was investigated, and the results reveal that the fum-**fcu**- MOF is a unique and selective sensitivity sensor of H_2S. This

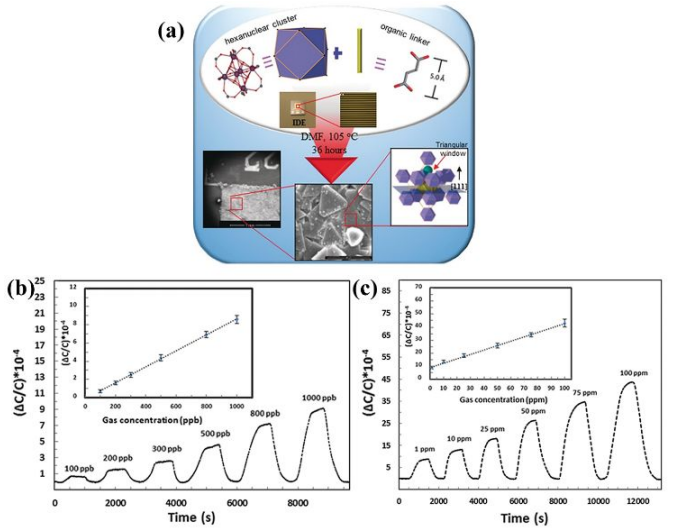

Fig. 18 (a) Schematic representation of the optimized solvothermal approach used to prepare the fumarate-based fcu-MOF (fum-fcu-MOF) thin film on the interdigitated electrode (IDE). Detection of H_2S in different ranges of concentrations: (b) 100–1000 ppb, (c) 1–100 ppm. Insets: linear response for the corre-sponding range. Reproduced with permission from ref. 193. Copyright 2016, John Wiley and Sons.

sensing property of the fum-**fcu**-MOF provides an opportunity for the deployment of MOFs as effective sensors for different applications.

3.3.2 Ammonia

Ammonia (NH_3) is a toxic, colourless gas that exerts stimulatory and corrosive effects on the skin and mucosa but is utilized extensively in chemical industries. Low concentrations of ammonia can cause ocular irritation and upper respiratory tract infection, while exposure to high concentrations may produce serious consequences, such as reflex respiratory arrest and cardiac arrest. Thus, the ability to sense NH_3 is required in different fields, such as environmental monitoring and chemical control in the human health, industrial and agricultural fields.

Chemiresistive MOF-based ammonia sensors have been widely investigated for the efficient charge transport between a conductive MOF host and ammonia guest[95-98,200-203]. Dincă et al. synthesized a 2D EC-MOF, $Cu_3(HITP)_2$ (HITP=2,3,6,7,10,11-hexaiminotriphenylene), with a high electrical conductivity of 0.2 S cm^{-1} that is potentially caused by the extended π-conjugation and in-plane charge delocalization of the 2D sheets[95]. Depending on the excellent electrical conduction, a convenient device was fabricated as a chemiresistive sensor for the reversible sensing of ammonia vapor for the first time (Fig. 19a and b). As shown in Fig. 19c, the current rapidly increased a few seconds after exposure to an ammonia/N_2 mixture, although ammonia concentrations were as low as 0.5 ppm. The current was restored to the stable baseline value when the ammonia flow was replaced with pure N_2, and the reversible process is reproducible for more than 10 cycles, indicating that $Cu_3(HITP)_2$-based devices are highly sensitive and reversible sensors of ammonia vapor. A study of the sensing mechanism revealed that the decrease in the conductance is caused by the hole quenching under the exposure to ammonia gas.

For single-ligand based EC-MOFs, the tunability in fields of both conductivity and topology is limited, and thus Kitagawa et al.

developed dual-ligand based EC-MOFs[96], Cu_3(HHTP)(THQ) (THQ = tetrahydroxy-1,4-quinone). Importantly, Cu_3(HHTP)(THQ) not only displayed tunable conductivity (ca. 2.53 × 10^{-5} S cm^{-1}) and high porosity (ca. 441.2 m^2 g^{-1}) but also exhibited semiconductor behaviour. All these characteristics endow Cu_3(HHTP)(THQ) with good room-temperature chemiresistive gas-sensing properties, and thus a Cu_3(HHTP)(THQ) nanowire thick film sensor was fabricated (Fig. 19d-g). Notably, the Cu_3(HHTP)(THQ) nanowire thick film sensor exhibited good chemiresistive sensing of NH_3 over a large range of NH_3 concentrations (1 ppm to saturated vapor) and displayed fine response–recovery properties of 1.65 and 2.57 min, respectively.

EC-MOF functioning as an ammonia sensor was further investigated by Xu et al[97]. The authors reported the controllable high quality fabrication of a thin film of an EC-MOF, Cu_3-$(HHTP)_2$, using a spray layer-by-layer liquid-phase epitaxial method (Fig. 19h and i). This method produces a superior film with a smooth surface, good crystallinity, and highly oriented structure, which shows high sensitivity and selectivity towards ammonia at room temperature. The $Cu_3(HITP)_2$ thin film only responds to NH_3 in the presence of different interfering gases with a LOD of approximately 0.5 ppm, an ultrafast response time, and excellent long-term stability and reproducibility, as it retained 88.4% of its original response after 3 months. The mechanism underlying the sensing performance may be mediated by the powerful interactions between ammonia and the framework (Fig. 19j).

Martí-Gastaldo et al. attempted to investigate a possible underlying mechanism by combining experimental data with computational modelling[98]. They fabricated ultrathin (10 nm) and highly oriented Cu_3-$(HHTP)_2$ films (Cu-CAT-1) using a bottom-up approach, and incorporated Cu-CAT-1 films into devices. The electrical conductivity mainly relies on the coordination interactions of the guest molecules to the active metal sites. Guest molecules such as NH_3 and H_2O capable of stronger interaction can cause a slight change of the coordination mode that has a significant influence on the electronic structure. To rationalize this phenomenon, the solvent-dependent electronic structure of Cu-CAT-1 was calculated by using dispersion-corrected density functional theory (DFT-D3). Importantly, the calculations reveal that there is a stronger interaction between H_2O and NH_3 molecules with open metal sites. The coordination geometry of the Cu^{2+} centres change from the square planar geometry to the distorted

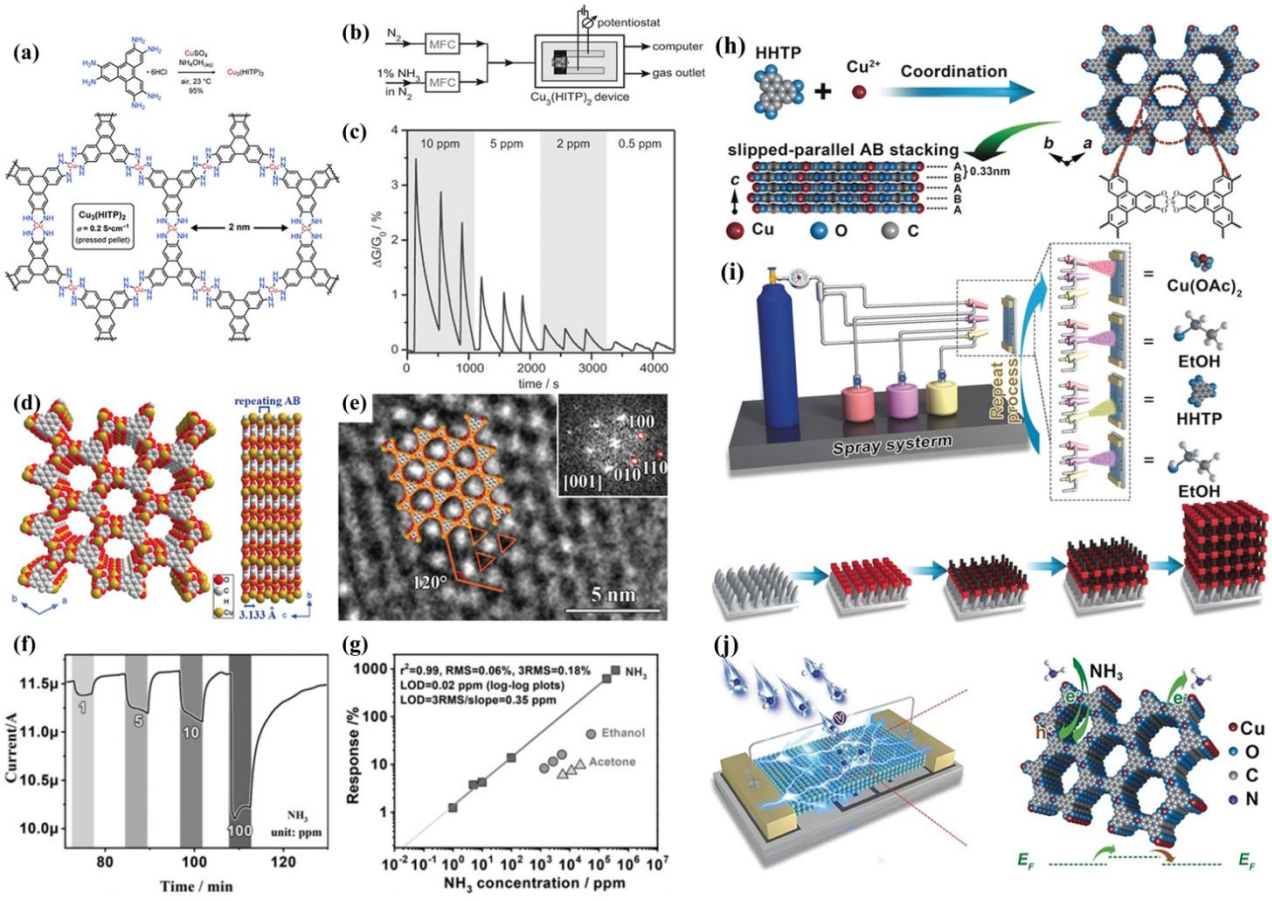

Fig. 19 (a) Synthesis and 2D chemical structure of $Cu_3(HITP)_2$. (b) Schematic of the experimental apparatus; MFC = mass flow controller. (c) Relative responses of a $Cu_3(HITP)_2$ device to 0.5, 2, 5, and 10 ppm ammonia diluted with nitrogen gas. Reproduced with permission from ref. 95. Copyright 2015, John Wiley and Sons. Characterization of Cu_3(HHTP)(THQ). (d) Space-filling model of the crystal structure (Cu gold, C gray, O red; hydrogen atoms are omitted for clarity). (e) HRTEM images viewed from the [001] direction; the inset in (e) shows the corresponding FFT analysis. Room-temperature gas-sensing performance of the thick-film gas sensor based on Cu_3(HHTP)(THQ) nanowires. (f) Response–recovery curve toward NH_3 at different concentrations. (g) Response–concentration log–log plot for NH_3 (plots for ethanol and acetone are also shown, in which case their concentration is shown on the *x*-axis). Reproduced with permission from ref. 96. Copyright 2020, John Wiley and Sons. Illustration of (h) the crystal structure of $Cu_3(HHTP)_2$ and (i) the preparation of $Cu_3(HHTP)_2$ thin film gas sensors. (j) The gas sensor and possible gas-sensing mechanism. Reproduced with permission from ref. 97. Copyright 2017, John Wiley and Sons.

trigonal prism with distinct difference of Cu-X distances with 2.7 Å and 2.2 Å, respectively. The strong interaction has a remarkable influence on the electronic structure. These DFT-calculations were further verified macroscopic Kelvin probe measurements, infrared reflection absorption spectroscopy, and powder X-ray diffraction experiments.

The interactions between ammonia and host framework can also induce the changing of coordination environments of metal centres[78,79,115]. Xiang et al. performed a MOF ($[Co(H_{0.27}L)]\cdot 4H_2O\cdot 0.5DMF$, H_3L = tris-(4-tetrazolyl-phenyl) amine) with mixed-valence Co centre[78]. Interestingly, the colour of MOF changes from red to brown upon exposure to ammonia, which is caused by the interactions between adsorbed ammonia molecules and active nitrogen sites that change the coordination mode of the Co centre. The MOF functions as a colorimetric sensor of ammonia with a LOD of approximately 1.38 ppm.

Dincă et al. incorporated fluorescent molecules into porous MOFs to construct two MOFs[204], Zn_2(TCPE) (TCPE = tetrakis(4-carboxyphenyl)ethylene) and Mg(H_2DHBDC) (H_2DHBDC^{2-} = 2,5-dihydroxybenzene-1,4-dicarboxylate). One of the limits about using of luminescence-based devices is the decrease in fluorescence observed upon melting or glassifying at high temperatures. Unusually, for the effective bonding in rigid MOFs, vibrational modes attributed to the decrease in fluorescence are minimized. Zn_2(TCPE) maintains its fluorescence at temperatures as high as 350 °C, which provides an advantageous condition to function as selective sensors for ammonia at high temperature. As shown in Fig. 20, when activated Zn_2(TCPE) is exposed to ammonia, ethylenediamine and various gas phase analytes at 100 °C, only ammonia exposure results in a significant shift in the emission peak from 487 to 511 nm, thus confirming the good sensing selectivity for NH_3. Unfortunately, this material does not display reversible sensing for high concentrations of ammonia, as its strong binding results in an irreversible phase change. In addition, the other candidate material, Mg(H_2DHBDC), also exhibits remarkable sensing for NH_3, as exposure of Mg(H_2DHBDC) to NH_3 gas at 100 °C induced a shift in the emission peak for only approximately 1 min. Notably, evacuating the samples for 15 min restored the emission, suggesting that selective sensing of NH_3 is reversible. The mechanistic studies reveal that the NH_3 sensing properties of Mg(H_2DHBDC) originate from molecular sieving and chemical selectivity. This mechanism was further examined for other luminescence-based MOF sensors[205-209]. Yan et al. generated a Eu^{3+} post-functionalized MOF (Eu^{3+}@Ga(OH)bpydc)[205], which exhibits excellent selectively and sensitivity for ammonia sensing among different indoor air pollutants. Interestingly, it also exhibits a high selectivity, short response time (<5 min) and excellent reproducibility for urea sensing in human urine.

Ammonia sensors based on chemical capacitance and impedance properties have been studied in recent years[210-213]. Salama et al. developed an interesting chemicapacitive sensor of ammonia based on a naphthalene-based RE MOF (RE-fcu-MOF) thin film deposited on a capacitive interdigitated electrode (IDE)[210]. The MOF thin film displayed distinctive NH_3 detection, even at low concentrations of 1 ppm (Fig. 21), with a LOD of approximately 100 ppb, even in the presence of various gases, including H_2O, NO,

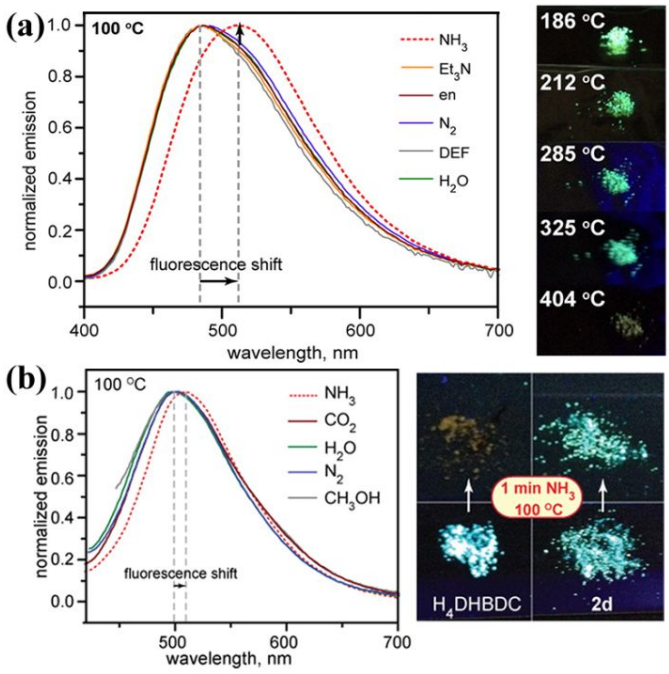

Fig. 20 (a) In situ normalized emission spectra (λ_{ex} = 350 nm) of Zn_2(TCPE) exposed to various analytes at 100 °C. The optical micrographs show fluorescent Zn_2(TCPE) (λ_{ex} = 350 nm) upon heating at various temperatures in air. (b) In situ emission spectra of Mg(H_2DHBDC) when exposed to various analytes at and 100 °C. The optical micrographs display the changes in the luminescence response upon exposure of H_4DHBDC and Mg(H_2DHBDC) to ammonia for 1 min at 100 °C. Reproduced with permission from ref. 204. Copyright 2013, American Chemical Society.

CH_3OH, and CO_2. The interactions between NH_3 long pairs and active metal sites and the hydrogen bonding of ammonia molecules may be responsible for the good sensing property.

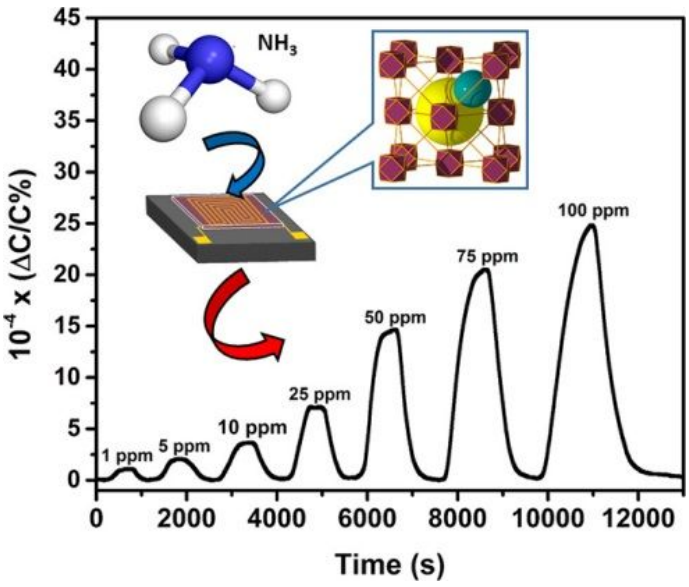

Fig. 21 Detection of NH_3 in different ranges of ppm concentrations: from (1-100 ppm). Inset: solvothermal preparation approach of naphthalene-based fcu-MOF (NDC-Y-fcu-MOF) thin film on IDE substrate. Reproduced with permission from ref. 210. Copyright 2017, American Chemical Society.

3.3.3 Sulfur Dioxide

Sulfur dioxide is one of the most abundant and widely distributed gas pollutants in the atmosphere that substantially affects human life and property. Together with nitrogen oxides, carbon monoxide, hydrocarbons and particulate matter, sulfur dioxide is considered the first of the five major pollutants in the atmosphere. Sulfur dioxide in the atmosphere mainly originates from two sources: natural sources and man-made sources. Over the years, due to the development of the global economy, the demand and consumption of energy and natural resources are increasing annually worldwide, leading to the increasingly serious pollution of sulfur dioxide in the atmosphere. Sulfur dioxide is the main cause of acid rain, and it causes substantial damage to the environment, human health, animals and plants. Therefore, fast and sensitive sensors of SO_2 are very important for environmental protection and human health[214].

Some interesting sulfur dioxide sensors have been investigated based on different properties of MOFs, including chemiresistive[215,216], magnetism[217], luminescence[218,219], mass change (quartz crystal microbalances)[220], and capacitance[221]. Kalidindi et al. chose a Zr-NH_2-benzenedicarboxylate MOF (NH_2-UiO-66) as a sulfur dioxide sensor due to its remarkable absorption of sulfur dioxide[216]. An excellent chemiresistive sensor of sulfur dioxide has been fabricated by taking advantage of the interactions between functional groups of ligands and guest molecules and the formation of a charge transfer complex. Cao et al. used an amino-functionalized LMOF (MOF-5-NH_2) material as a luminescent SO_2 sensor[218]. The guest sulfur dioxide molecules react with functional amino groups to hinder the charge transfer process. In addition, the MOF-5-NH_2-based test paper also displays excellent sensing of SO_2, which provides a possibility for use in practical sensing applications (Fig. 22).

Schröder et al. synthesized a novel framework $[Al_2(OH)_2(C_{16}O_8H_6)](H_2O)_6$ ($C_{16}O_8H_6$ = biphenyl-3,3′,5,5′-tetracarboxylic acid)[222]. The Al–OH groups are located in the channel of the MOF, which easily participate in the formation of various interactions with SO_2. The hydrogen bond interactions between hydroxyl groups and SO_2 were further examined using *in situ* inelastic neutron scattering, powder X-ray diffraction and modelling experiments. At the same time, weak supramolecular interactions between guest molecules and C–H atoms on the aromatic rings reinforce the interactions to improve the sensing property.

3.3.4 Nitrous Oxides

In recent years, with rapid development of society, air pollution has become a very serious problem. As a greenhouse gas, nitrogen dioxide (NO_2) exerts a substantial negative effect on the environment by promoting the formation of ozone and acid rain. In addition, nitrogen dioxide is a harmful chemical that exerts toxic effects on human health. Some researchers have focused on NO_2 gas sensors[223-229].

Huang et al. presented a flexible and wearable sensor device based on MOFs (e.g., ZIF-67-Co and MIL-88-Fe) combined with conductive multiwalled carbon nanotubes (MWCNTs) as an NO_2 gas sensor[223]. Due to the large surface area, unique structure features, and functional fibres loaded with MOF, these devices are gas sensors with excellent sensitivity. ZIF-67-Co/MWCNT hybrid fibres showed a desirable gas-sensing property with a detection limit for NO_2 as low as 0.1 ppm, without external heating to induce a distinct negative resistance response. Additionally, MOF-derived metal oxides (MOs)/MWCNTs hybrid fibres display synergistic enhanced gas-sensing behaviours for the similar negative responsive nature of both Co_3O_4 and MWCNT. The mechanism of NO_2 sensing was

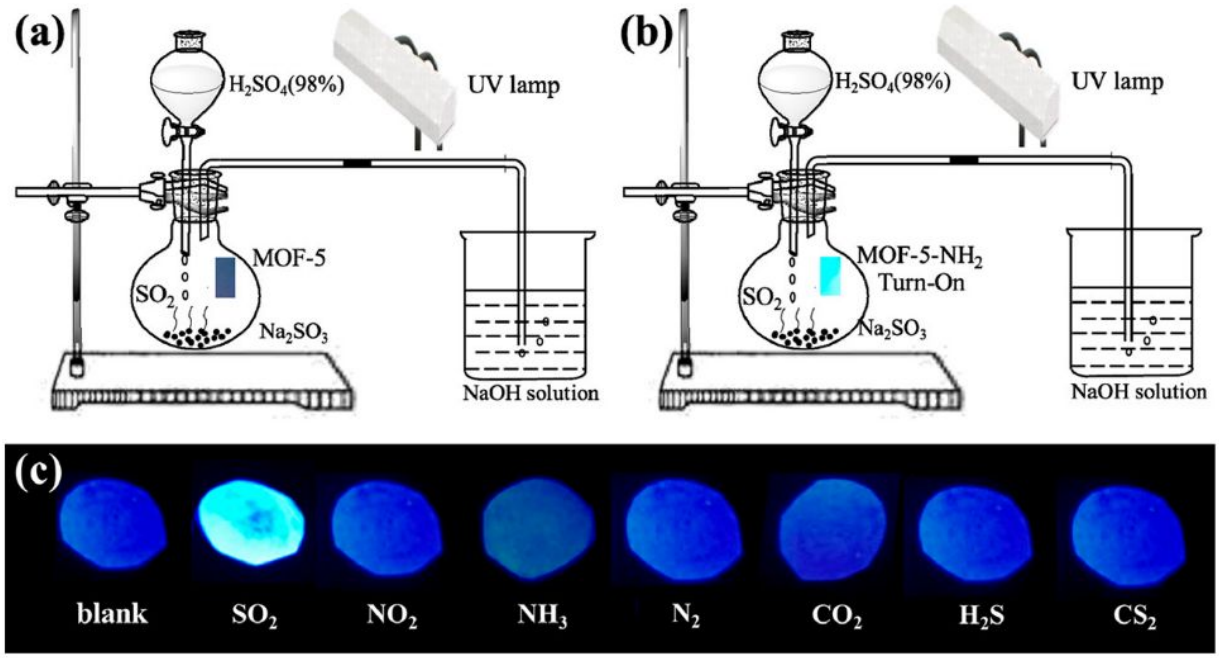

Fig. 22 (a, b) Schematic diagrams of the device for detecting SO_2 gas using MOF-5 and MOF-5-NH_2 luminescent test paper, respectively. (c) Luminescence response photographs of MOF-5-NH_2 luminescent test paper after exposure to various gas species under a 365 nm UV lamp. The final concentrations of SO_2, NO_2, NH_3, N_2, CO_2, and H_2S were 2 ppm, while CS_2 gas was saturated vapor of liquid-state CS_2. Reproduced with permission from ref. 218. Copyright 2018, American Chemical Society.

further investigated. The resistance of the sensor device decreased immediately upon exposure to NO_2, as adsorbed NO_2 attracts electrons from its surface oxygen ion to increase the hole concentration and the conductivity.

A calixarene-based MOF (Zr-cal, $[Zr_6O_4(OH)_4(FA)_6]_2(cal)_3]$, FA = formate, *cal* = 1,3-alt-25,26,27,28-tetrakis[(carboxy)methoxy]calixarene) was constructed by Schaate et al[225]. Interestingly, the calixarene cavities are accessible to the guest molecules. The exposed calixarenes functioned as a visual sensor of NO_2 based on the charge–transfer complexes formed between guest molecules and the MOF (Fig. 23a-c). More importantly, the MOF was coated on glass slides and placed in a homemade sensor cell for use as a sensor material and showed high sensitivity for NO_2 in air (Fig. 23d and e).

Salama et al. reported a highly selective and ultrasensitive OFET (Organic field-effect transistor) sensor for NO_2, which combined an ultrathin and stable PDVT-10 organic semiconductor and a 3D porous MOF $[Ni(TiF_6)(TPyP)]_n$[228]. The $[Ni(TiF_6)(TPyP)]_n$ layer can specifically preconcentrate NO_2 gas in the sensor device, achieving an unprecedented enhancement (700%-fold) of NO_2 sensitivity in contrast to the pristine PDVT-10. Furthermore, owing to the synergistic combination, this OFET sensor device showed an excellent sensitivity of 680 nA/ppb, a remarkable lowest detection limit of 8.25 ppb, and a high stability for 6 months under ambient condition. This work indicated that the synergistic combination from proper receptor materials can highly improve the sensing performance of an OFET sensor.

Nitric oxide (NO) is an extremely toxic gas and is widely regarded as an important signalling agent of bioactive substances. It displays strong oxidizability and is easy to ignite when it is in contact with combustible organic matter. NO mainly damages the respiratory tract, with only mild eye and respiratory irritation symptoms reported after inhalation.

The NO chemicapacitive sensor and luminescent sensor have been studied in recent years[230-234]. A chemiresistive MOF-based nitric oxide sensor has been reported by Mirica et al. The authors described an efficient strategy for the combination of nickel phthalocyanine-based building units and nickel naphthalocyanine-based bimetallic conductive two-dimensional MOFs[230]. The resulting 2D mesh structures exhibit excellent conductivity, a large surface area, low-dimensionality, and highly ordered active sites that endow the device with the potential property of a chemiresistive gas sensor. Devices show an excellent capacity to detect gaseous analytes, and the LOD are as low as 1.0−1.1 ppb for NO at room temperature upon exposure to vapor for approximately 1.5 min. The performance of all devices is maintained in a humidified gas stream (18% relative humidity). The chemiresistive sensing mechanism may arise from the surface reaction between the analyte molecules and the active sites on the surface of the materials, namely, the charge-transfer or redox process occurring between the host and guest, which may ultimately induce a change in the conductive property of the materials. The sensing mechanism was further confirmed by the results of XPS and EPR experiments, as the metal centres were oxidized from Cu^+ to Cu^{2+} after the MOF sample was exposed to NO.

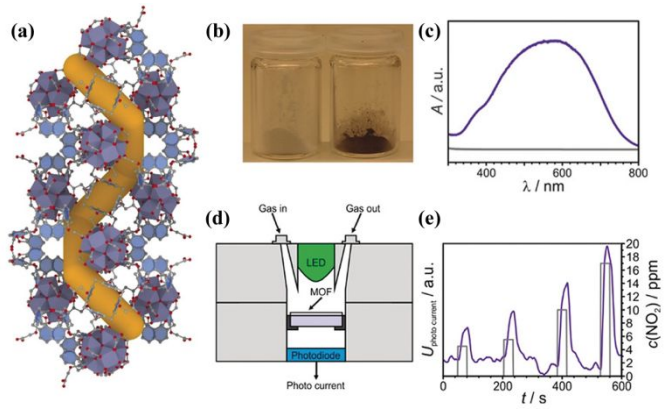

Fig. 23 (a) An image of the environment surrounding one helical channel of one pore system showing the direct connection between calixarene cavities and the pore system (dark blue polyhedra: Zr; red: oxygen; grey: carbon). (b) Photograph of the Zr-*cal* MOF before (left panel) and after (right panel) NO_2 exposure. (c) UV/Vis spectra of the Zr-*cal* MOF before (gray) and after prolonged NO_2 exposure (purple). (d) Schematic diagram of the sensor setup. (e) Response to different NO_2 concentrations in purified air. Reproduced with permission from ref. 226. Copyright 2018, John Wiley and Sons.

3.3.5 Carbon Oxides

Carbon monoxide (CO) is a notorious pollutant that is colourless, tasteless and odourless, and it is produced when any carbon-containing fuel is not burned adequately. It is toxic to humans at relatively low concentrations, as 50 ppm of CO rapidly binds to haemoglobin, decreases the oxygen capacity of the blood and then causes tissue hypoxia. CO will poison people and even cause life-threatening consequences when people are exposed to concentrations greater than 50 ppm for long periods or concentrations of 200 ppm for any duration. For this reason, a reusable and selective sensor for CO is desirable; chemical sensors are ideal devices to detect CO, and several examples of CO sensors have been reported[235-238].

Long et al. synthesized a Fe-based MOF, $Fe_3[(Fe_4Cl)_3(BTTri)_8]_2{\cdot}18CH_3OH$ (Fe-BTTri, H_3BTTri = 1,3,5-tris(1H-1, 2,3-triazol-5-yl)benzene)[235], which features high-spin Fe^{2+} centres. The MOF showed significant CO adsorption capacity and readily reversible CO binding, accompanied by a reversible changeover of the spin states of Fe^{2+} centres from HS to LS. The Mössbauer spectroscopy and dc magnetic susceptibility tests evidence the variation of spin states. The Mössbauer spectroscopy of Fe-BTTri reveals several HS Fe^{2+} species, while both HS and LS Fe^{2+} species are observed in the CO-dosed framework (Fig. 24), suggesting the reversible change of the electron configuration of Fe^{2+} upon binding CO. The magnetic measurements also indicate the conversion of Fe^{2+} centres. Importantly, the spin state change of Fe-BTTri displays highly selective of CO, which originate from the unprecedentedly high selectivity for CO adsorption of Fe-BTTri.

Wilton-Ely et al. reported a simple, inexpensive system based on ruthenium(II) and osmium(II) vinyl complexes $[M(CH=CHR)Cl(CO)(BTD)(PPh_3)_2]$ (R = aryl, BTD = 2,1,3-benzothiadiazole)[236]. The authors constructed eight ruthenium(II) and osmium(II) vinyl complexes containing different vinyl ligands and the BTD chromophore. Most showed a colour change, some displayed remarkable colour modulations from orange to yellow, and others showed colour changes from purple to yellow. A subsequent time-dependent density functional theory (TDDFT) computational study and single-crystal X-ray diffraction investigation analysed on these modulations in colour. More

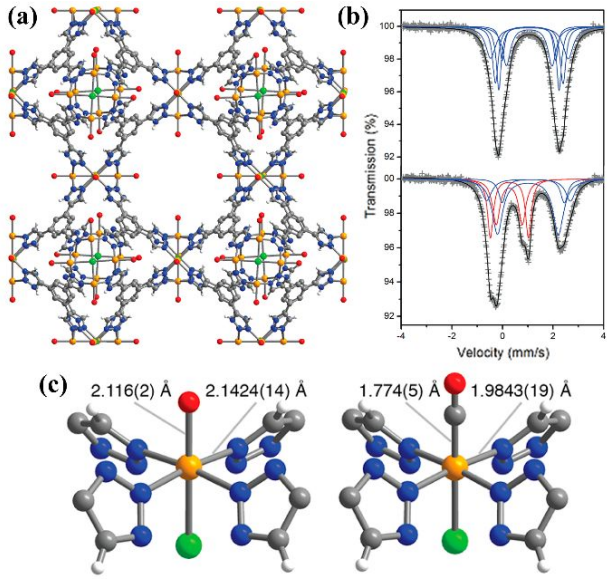

Fig. 24 (a) Portion of the structure of DMF-solvated Fe-BTTri (left) as determined by analysis of single-crystal X-ray diffraction data. (b) Mössbauer spectra collected at 100 K for Fe-BTTri (upper) and CO-dosed Fe-BTTri (lower), with the experimental data in gray plusses and the total fit in black. In both spectra, the blue components are assigned to high-spin Fe^{2+}. In CO-dosed Fe-BTTri, the red components are assigned to low-spin Fe^{2+}. (c) Portion of the structure of DMF-solvated Fe-BTTri (left) and CO-dosed Fe-BTTri-$(CO)_{24}$ (right), as determined by analysis of single-crystal X-ray diffraction data, with selected bond lengths highlighted. Numbers in parentheses give the estimated standard deviation in the final digits of the number. Orange, gray, red, blue, green, and white spheres represent Fe, C, O, N, Cl, and H atoms, respectively. Reproduced with permission from ref. 235. Copyright 2016, American Chemical Society.

importantly, the unusual selectivity for CO over water vapor and all organic solvents tested provides a new potential application of these devices.

CO is a common greenhouse gas, and it is mainly derived from the burning of fossil fuels, emissions from chemical production processes, and automobile exhaust, among other processes. In recent years, the sensing of carbon dioxide has become an important research topic. However, the sensing of ambient CO_2 is difficult to achieve due to the complexity of the atmosphere. Some notable studies representing the great efforts of some groups have been published[239-247]. Dincă et al. reported a chemiresistive sensor for ambient CO_2 composed of 2D EC-MOFs, namely, Cu_3(hexaiminobenzene)$_2$[239]. The MOF is selective for sensing ambient CO_2, and the sensing property is virtually unaffected by humidity in a broad RH range from 10% RH to 80% RH. The spontaneously formed hydrated adsorption sites and the binding interactions between CO_2 and the host are responsible for the RH-independent sensing property of MOF.

Jeong et al. prepared a cyclodextrin-based MOF as an electrochemical sensor of CO_2, the numerous hydroxyl groups in the MOF form abundant interactions between the guest and host[244]. Interestingly, the electrochemical impedance of MOF shows a significant decrease in the presence of CO_2 due to the interaction between CO_2 and the hydroxyl group.

3.3.6 Carbon Disulfide

Carbon disulfide (CS_2), a harmful volatile organic solvent, causes a serious threat to industrial safety and human health. CS_2 is involved in photochemical reactions and is oxidized to carbonyl sulfide and sulfur dioxide to produce acid rain. CS_2 is a widespread enzyme inhibitor with cytotoxic effects that disrupt the normal metabolism of cells and cause vascular and neurological diseases, such as Parkinson's disease, peripheral neuropathy, arteriosclerosis, and coronary heart disease. In addition, carbon disulfide also displays embryonic toxicity and reproductive toxicity. The ability to sense carbon disulfide gas is very important for pollution emission control and safety assurance. Carbon disulfide sensors are mainly based on the LMOF[248-252]. Huang et al. fabricated a novel magnesium MOF[249], $Mg_5(OH)_2(BTEC)_2(H_2O)_4{\cdot}11H_2O$ (H_4BTEC = 1,2,4,5-benzenetetracarboxylic acid). The MOF exhibited blue-purple emission and significant quenching of the luminescence intensity upon exposure to CS_2. Interestingly, the fluorescence intensities are only completely quenched in the presence of a CS_2 content of 0.8 vol%. The absorption band of the ligand overlaps with carbon disulfide, and thus energy transfer may be the mechanism underlying the luminescent quenching of carbon disulfide.

3.4 Volatile Organic Compounds (VOCs) Sensing

VOCs are a new type of organic pollutant that easily volatilize into air under normal atmospheric conditions and are very damaging to human health and environment. VOCs mainly contain aromatic hydrocarbons (benzene, toluene, xylene, etc.), aliphatic hydrocarbons (ethane, ethylene, and acetylene), ketone (acetone and butanone), alcohols (methanol, ethanol, butanol, etc.), aldehydes (formaldehyde, acetaldehyde, etc.), and chlorinated hydrocarbons (dichloromethane, chloroform, etc.). The study of explosive materials is mainly focused on solids and liquids[52], while the gas is relatively less frequently studied[253-255], and thus it is not included in the scope of our review. Most of the VOCs are toxic air/water pollutants that substantially endanger human health and pose threats to the ecosystem. At the same time, they are widely applied in numerous ways by various industries. Therefore, the rapid detection of VOCs is attracting increasing attention.

3.4.1 Aromatic Hydrocarbons

The aromatic hydrocarbons are mainly derived from industrial emissions, and these types of VOCs are often toxic and environmentally harmful. Different properties of MOF-based sensors of aromatic hydrocarbons have been extensively studied in recent years, including chemiresistive[99,101,256,257], magnetism[108,109,258], luminescence[259-272], mass change (quartz crystal microbalances)[273-276], and capacitance[277].

Dincă et al. selected a group of conductive 2D MOFs that were structurally analogous but chemically diverse to investigate the relationships between the different sensing responses of different types of molecules and the chemical modifications[99]. Three materials were used in this research, $Cu_3(HHTP)_2$, $Cu_3(HITP)_2$, and $Ni_3(HITP)_2$, to fabricatecross-reactive chemiresistive sensor arrays. The different MOF-based sensor arrays display various responses to five characteristic VOCs (aliphatic hydrocarbons, alcohols, ketones/ethers, aromatic hydrocarbons, and amines). As shown in Fig. 25a, each MOF often shows a different response in the direction and/or the magnitude for a particular analyte. Charge transfer, swelling/solvation, and Schottky barrier modulation are the common sensing mechanisms in chemiresistive devices. For these MOF-based chemiresistors, the rigid crystalline structures are

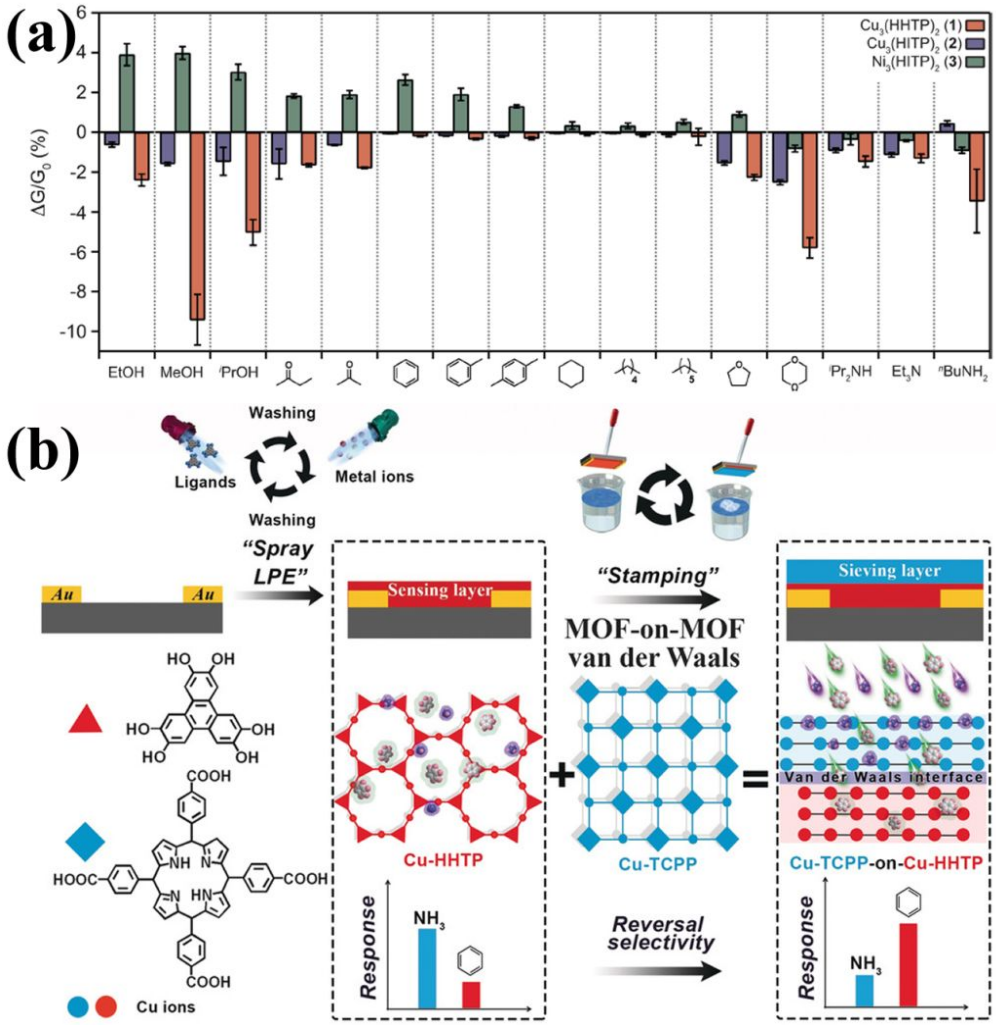

Fig. 25 (a) Sensing responses of the MOF array to representative examples from different categories of VOCs, where ΔG/G0 is the relative response (change in conductance) upon a 30 s exposure to 200 ppm of the VOC vapor; each response is the average of 12 measurements (4 exposures to 3 separate devices for each MOF); error bars indicate one standard deviation. Reproduced with permission from ref. 99. Copyright 2015, American Chemical Society. (b) Illustration of the method used to prepare MOF-on-MOF thin films with vdW integration and application of the films as highly selective benzene-sensing materials. Reproduced with permission from ref. 101. Copyright 2019, John Wiley and Sons.

not susceptible to swelling effects; moreover, all of MOF devices exhibit ohmic contacts, excluding Schottky barrier modulation.

In addition, the inherent charge density of the MOF plays a key role in sensing with a charge transfer mechanism. In addition to the charge transfer mechanism, hydrogen bonding may be a factor contributing to the observed sensing response.

Occasionally, a single MOF is unable to meet the requirements of the sensor device; therefore, Xu et al. developed heterostructured MOF-on-MOF thin films combining the various properties of different MOF layers using the Van der Waals (vdW) integration method[101]. Two lattice-mismatched MOF layers, Cu-TCPP (TCPP = 5,10,15,20-tetrakis-(4-carboxyphenyl)porphyrin) and Cu-HHTP, were chosen to assemble highly quality MOF-on-MOF thin films by integrating a molecular sieving Cu-TCPP layer onto a chemiresistive sensing Cu-HHTP layer with a tunable thickness. Cu-TCPP was carefully chosen as the gas molecular sieving layer due to the abundant coordination-unsaturated Cu ions that exhibit stronger interactions with NH_3 than with benzene in the 2D structure, and Cu-HHTP served as the sensing layer to produce a highly sensitive and selective gas sensor (Fig. 25b). The Cu-TCPP-on-Cu-HHTP sensor achieved excellent selectivity and the highest response to benzene. Furthermore, it also detected and distinguished five representative human breath biomarkers, such as NH_3, benzene, hexane, carbon monoxide, and acetone.

An interesting LMOF-based sensor of aromatic hydrocarbons was reported by Zhao et al[260]. The authors used a tetraphenylethene (TPE) derivative with an aggregation-induced emission (AIE) characteristic as an organic ligand to construct a LMOF (NUS-1) (Fig. 26a). Two dangling phenyl rings were incorporated into the MOF, which served as functional group to detect guest molecules through the interactions between the host and guest. Interestingly, NUS-1 functions as a luminescent sensor for aromatic hydrocarbons (Fig. 26b and c). Different types of aromatic hydrocarbons induce various emission peaks by altering the conformation of the AIE ligand.

3.4.2 Aliphatic Hydrocarbons

Aliphatic hydrocarbons are the most widely used raw material in industrial synthesis and production, and most of them exert different environmental and toxicological effects[278-284]. Long et

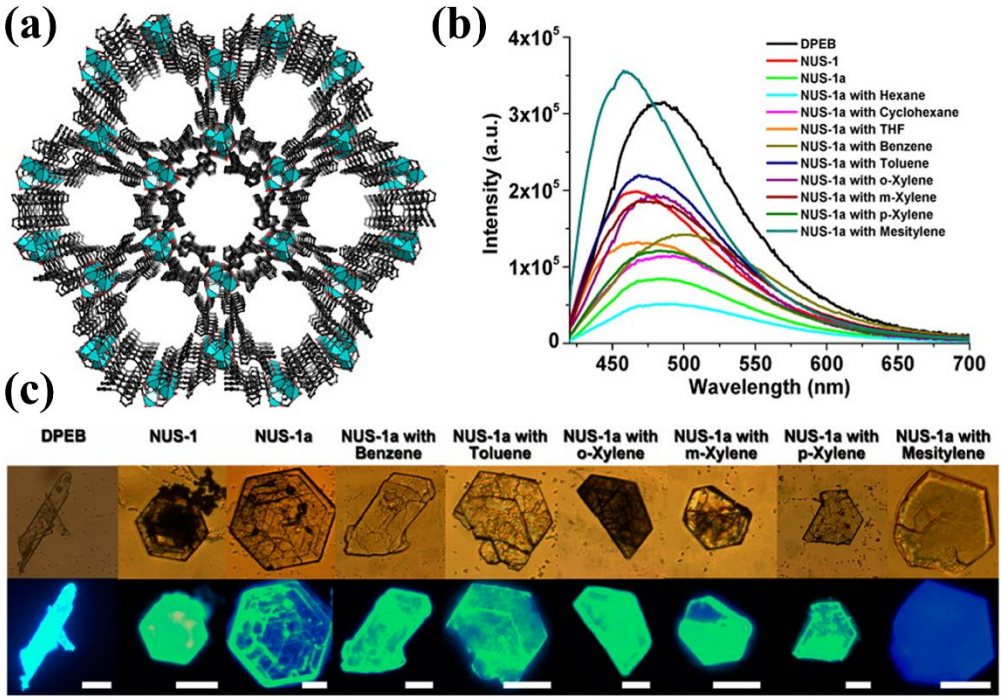

Fig. 26 Crystal structure of NUS-1 viewed along the [001] direction. (b) Fluorescent emission spectra. (c) Fluorescence microscopy images (first row, optical images; second row, fluorescence images; scale bar, 30 μm). Reproduced with permission from ref. 260. Copyright 2014, American Chemical Society.

al. investigated the reported 3D conductive MOF Cu[Ni(pdt)$_2$] (pdt^{2-} = pyrazine-2,3-dithiolate) (Fig. 27a), whose conductivity is remarkably sensitive to the solvation state[278]. The conductive property is very sensitive to guest inclusion, as the conductivity of an acetonitrile-solvated framework Cu[Ni(pdt)$_2$]·nCH$_3$CN is increased 200-fold. Moreover, Cu[Ni(pdt)$_2$] displays excellent chemiresistive detection of gaseous hydrocarbons (ethane, ethylene, acetylene, propane, propylene, and cis-2-butene) due to its impressive adsorption of hydrocarbons and show different changes in conductivity in response to various hydrocarbon (Fig. 27b). Finally, the change in Cu[Ni(pdt)$_2$] conductance mainly relies on the gas-phase specific heat capacity of the analyte, but not on the binding strength, for all gases tested. This contribution may be appropriate for all physisorption-based chemiresistive materials.

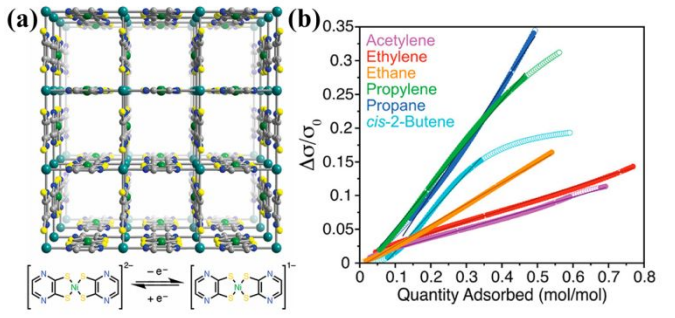

Fig. 27 (a) (Top panel) A portion of the crystal structure of Cu[Ni(pdt)$_2$] illustrating the one-dimensional pore structure normal to the page. Teal, green, yellow, blue, and grey spheres represent Cu, Ni, S, N, and C atoms, respectively; H atoms are omitted for clarity. (Bottom panel) Illustration of the redox-active Ni(pdt)$_2$ subunit. (b) Conductivity–composition profiles in Cu[Ni(pdt)$_2$]·nC$_x$H$_y$. Coloured circles indicate the estimated linear regime used to determine the sensitivity, S. Empirical fits to the data are shown as lines. The units for quantity adsorbed are moles of adsorbate per mole of Cu[Ni(pdt)$_2$]. Reproduced with permission from ref. 278. Copyright 2019, American Chemical Society.

Another interesting study of Cu[M(pdt)$_2$] as an acetylene sensor was reported by Zaworotko et al[279]. Due to the high water stability and thermal stability of Cu[M(pdt)$_2$], it is a good platform for preparing functional materials. In addition, Cu[M(pdt)$_2$] contains numerous active metal sites, which is beneficial for sensing. Fortunately, it displays good selectivity for acetylene attributed to the binding affinity between the guest and active metal sites and interactions between acetylene and the ligand, such hydrogen bonding and π–π interactions.

3.4.3 Ketones

Acetone is the most frequently studied ketone VOC. Acetone has been widely employed in many fields, such as the laboratory, medical fields, and chemical industry, for the development of modern science and technology. Acetone not only is convenient in our daily lives and industrial production but also potentially causes many healthy problems, such as irritating the eyes, skin and respiratory tract, and inducing dizziness, intoxication, drowsiness, nausea, and vomiting, while high concentrations may cause unconsciousness, coma or even death. At the same time, acetone is a volatile chemical reagent, and its steam and air will form an explosive mixture that may cause combustion, explosion and other accidents, resulting in serious economic losses and even endangering life and safety. Therefore, a high-quality acetone gas sensor must be constructed for personal and environmental protection purposes.

Chemiresistive MOF-based acetone sensors have been studied by Xu et al[285]. They prepared a MOX@catalytic MOF core–sheath nanowire array using a new design strategy reported for the first time (Fig. 28a), and this array functions as an acetone sensor. This

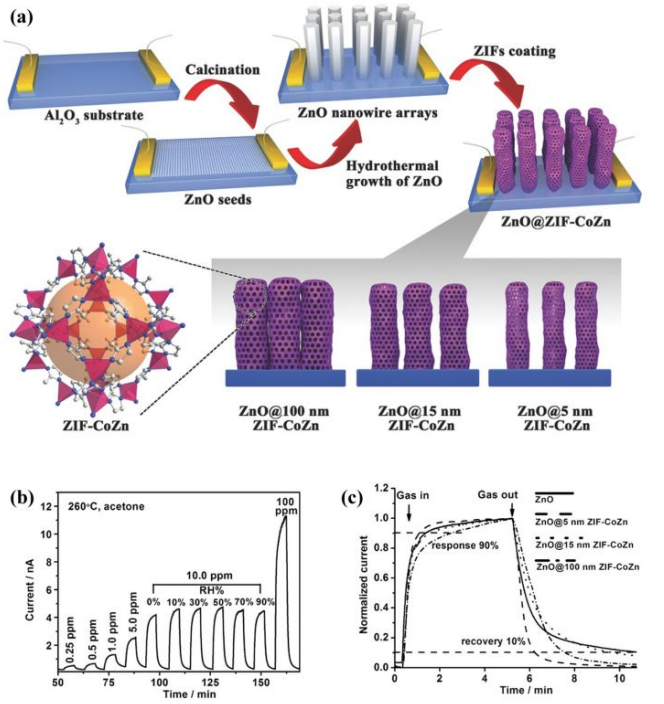

Fig. 28 (a) A new strategy for preparing ZnO@ZIF-CoZn gas sensors. (b) Response-recovery curves of ZnO@5 nm ZIF-CoZn to acetone with different concentrations in dry air and to 10 ppm acetone with different relative humidity levels. (c) Response-recovery curves to 100 ppm acetone at 260 °C. Reproduced with permission from ref. 285. Copyright 2016, John Wiley and Sons.

new material exhibits significantly enhanced performance compared with the material without the MOF sheath. The selectivity, response intensity, detection limit, reversibility and operating temperature are all substantially improved (Fig. 28b and c). The sensing property relies on the surface reaction between the acetone molecules and oxygen species, and the produced electron improves the conductivity of MOX.

LMOF-based acetone sensors have been widely studied due to their inherent characteristics, such as a short response time, fast response speed, and good sensitivity[286-311]. The first porous metal-organic framework-based acetone sensor was reported by Qian et al[286]. They investigated a Eu-MOF formulated as $Eu(BTC)(H_2O)\cdot 1.5H_2O$, which exhibits characteristic Eu^{3+} emission peaks. Notably, its PL spectrum shows a significant quenching effect upon exposure to acetone. Further fluorescence studies indicate that the quenching mechanism is controlled by diffusion. Next, several acetone sensors based on LMOFs were studied. Zhang et al. also investigated a Eu-MOF (Fig. 29a) where Lewis-base sites and coordinated water molecules were incorporated into the MOF, which served as a signal transmission media for the sensing of guests at the molecular level[287]. As shown in Fig. 29b, the intensities depended on the solvent molecules, specifically for acetone, which displays the most effective quenching after excitation at 320 nm. The observable absorption intensity at 320 nm of acetone is responsible for the quenching effect, which was further verified by the lack of change in the emission intensity upon excitation at 362 nm and lack of absorption of acetone at this wavelength. Most LMOF-based acetone sensors employ the luminescent quenching mechanism, and only a few employ an increase in fluorescence

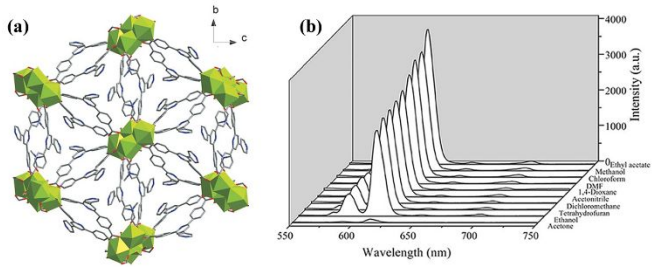

Fig. 29 (a) Packing representation of compound viewed along the *a* axis. (d) PL spectra of the compound introduced into various pure solvents. Excitation: 320 nm. Reproduced with permission from ref. 286. Copyright 2014, John Wiley and Sons.

a luminescent redshift and tremendous increase in luminescence upon exposure to acetone. The mechanism underlying the increase in luminescence is energy transfer between acetone molecules and carboxylic groups[292].

3.4.4 Alcohols

Alcohols are commonly used solvents in industrial production and by-products of some industrial reactions. The widespread use of alcohols also makes them a common environmental pollutant.

Mass change (quartz crystal microbalances)[312], chemiresistive[313,314], magnetism[315-320], chromism[116,117,321], luminescence[322-328], and capacitance[329-334] dependent MOF sensors for sensing alcohols have been investigated. Tong et al. reported a Hofmann-type MOF, [Fe(4-abpt){Ag(CN)$_2$}$_2$]·2DMF·EtOH (1·2DMF·EtOH, 4-abpt = 4-amino-3,5-bis(4-pyridyl)-1,2,4-triazole), which exhibits an interesting hysteretic four-steps SCO property (Fig. 30a)[315]. Altering the guest molecules can transform the spin transitions property of MOF, a one-step SCO system is produced by ethanol exchange, and N,N'-dimethylformamide and acetonitrile exchange result in a two-step

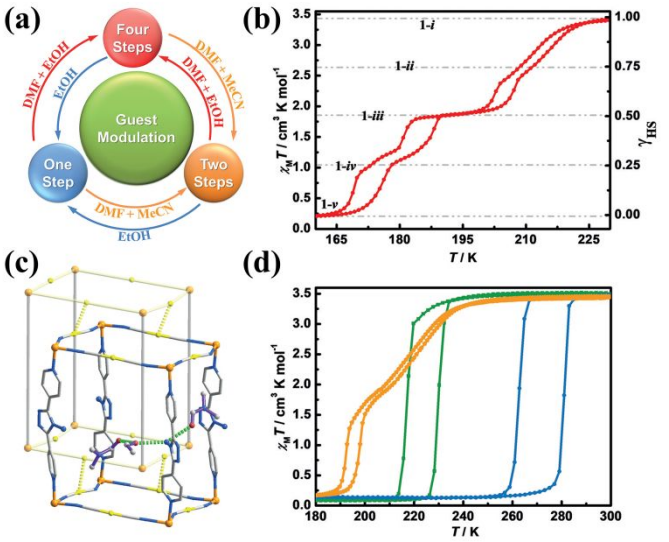

Fig. 30 (a) Graphical representation of the reversible modulation of four-, two-, and one-step spin-crossover behaviours through guest exchange. (b) Temperature dependence of $\chi_M T$ at 2 K min^{-1} for 1·2DMF·EtOH. Dashed lines are provided for different HS fractions. (c) Structural representations of 1·2DMF·EtOH at 240 K with conventional hydrogen-bonding interactions (green dashed lines) and argentophilic interactions (yellow dashed lines) highlighted. The two-fold interpenetrated framework has been simplified for clarity. Fe: orange, Ag: yellow, N: blue, O: red, and C: grey. (d) Temperature dependence of $\chi_M T$ at 2 K min^{-1} for 1·2DMF·MeCN (orange), 1·*x*EtOH (blue), and 1·*y*MeCN (green). Reproduced with permission from ref. 315. Copyright 2017, John Wiley and Sons.

SCO behaviour. The guest-dependant SCO property originates from the different host and guest interactions and hydrogen bond interactions of different guest molecules (Fig. 30b-d). The solvent-induced magnetic switching has been investigated by the Gao and Sato laboratories.

Ghosh et al. used a tridentate ligand to construct two MOFs: $([In(L)(Cl)_3]_n$ and $[Mn_2(L)_2(Cl)_4]_n$, L = Tris(4-(1H-imidazol-1-yl)phenyl)amine)[328]. The luminescent emission of both MOFs displays a remarkable shift upon exposure to allyl alcohol, indicating a good sensing property. High selectivity has been achieved for the unique π-electrons of allyl alcohol. The relatively matched energy of the MOF and allyl alcohol promote the formation of a MOF–allyl alcohol complex may be the mechanism underlying the sensing behaviour. A capacitive sensor for methanol was investigated by Gascón et al. The authors chose MIL-96(Al) MOF to construct thin films and fabricate a sensor device on the IDE chips. The MOF-based thin films show wonderful selectivity for methanol, a fast response time (approximately 10-15 min), good reproducibility and stability.

3.4.5 Aldehyde

Formaldehyde (HCHO) is a colourless gas that is toxic and characterized by a pungent, irritating odor. The main toxic effect of formaldehyde is the irritation to skin mucous membrane. The wide use of formaldehyde makes it one of the most harmful indoor pollutants, and formaldehyde in indoor air has become a major pollutant affecting human health. Thus, an effective and convenient method for detecting HCHO has significant practical interest[100,113,123,335-341].

A chemiresistive MOF-based sensor was studied for the first time by Zhang and collegues[100]. They chose a large surface area and highly stable zeolitic imidazolate framework (ZIF), ZIF-67, as the platform for sensing formaldehyde gas (Fig. 31a). Good selectivity and high sensitivity to formaldehyde were successfully achieved. Upon exposing ZIF-67 to diverse gases (formaldehyde, methanol, acetone, ammonia, and methane) at the same concentration and different operating temperatures, the sensor displays different responses and shows the highest response (13.9) to formaldehyde at 150 °C (Fig. 31b). The response-recovery experiments reveal that the ZIF-67 gas sensor detects formaldehyde at concentrations as low as 5 ppm. It may be a promising candidate for formaldehyde detection in practical applications.

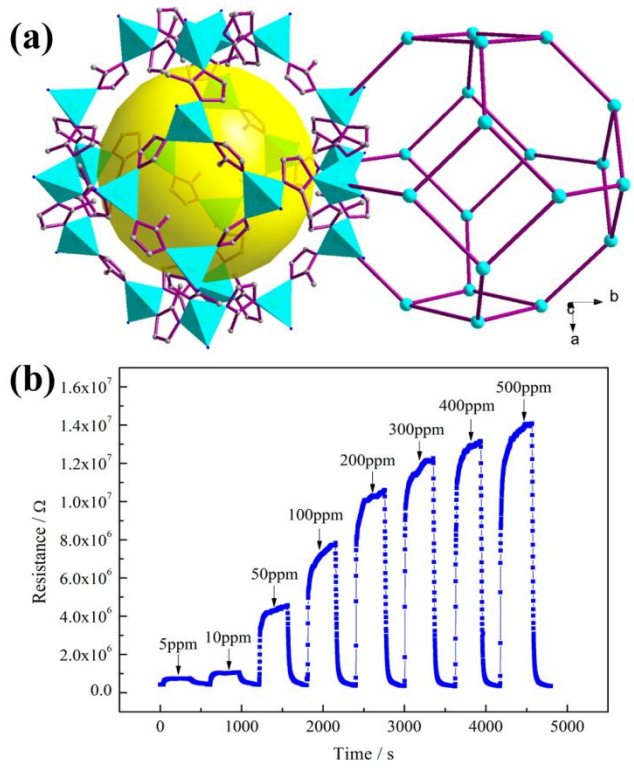

Fig. 31 (a) The structure of ZIF-67. (b) Response–recovery curve of the ZIF-67 sensor. ref. 100. Copyright 2014, American Chemical Society.

Yan et al. fabricated a dual-emission 4d–4f Ag^+–Eu^{3+}-functionalized MOF that serves as a self-calibrating luminescent probe for detecting indoor formaldehyde (FA) for the first time[335]. A UiO Nano-MOF was synthesized with two uncoordinated carbonyl groups per ligand, and further postfunctionalization with the transition metal cations Eu^{3+} and Ag^+ was achieved. The luminescence properties of the free ligands and the characteristic sharp emission bands of the encapsulated Eu^{3+} ions enable it to function as a self-calibrating luminescent probe for detecting FA. Upon the exposure of MOFs to various concentrations of FA vapors, the emission intensity of Eu^{3+} regularly increased, while the emission from the ligand centre at 490 nm decreased, revealing a good linear relationship between I_{Eu}/I_L and the FA concentration and indicating that Ag^+–Eu^{3+} MOF is an excellent ratiometric luminescent sensor for the quantitative analysis of FA. The mechanism of FA sensing is studied; the Ag^+ doping changes the electric structure of the organic ligands and then affects the ligand-to-Eu energy transfer process. After treatment with FA, the interaction between Ag^+ and FA alters the emission of MOF.

3.4.6 Chlorinated Hydrocarbons

As an important organic solvent and product intermediate, chlorinated hydrocarbons are widely used in many industries, but they are often carcinogenic, teratogenic and mutagenic substances. After chlorinated hydrocarbons are absorbed through the skin, they invade the nervous system or the internal organs, causing poisoning.

The luminescent[91,342-343] and chromism-based[344,345] MOF sensors for chlorinated hydrocarbons have been studied. Zheng et al. presented a MOF $\{[(WS_4Cu_4)I_2(dptz)_3]\ 3DMF\}_n$ (dptz = 3,6-di-(pyridin-4-yl)-1,2,4,5-tetrazine) featuring interesting nanotubes[342]. The desolvated MOF displays a solvent polarity-dependent colour change, and the absorption bands of MOF which treated with $CHCl_3$ are redshifted by approximately 245 nm. The strong π-acceptor property of the organic ligand and electronic structure are easily disturbed by solvent molecules and play an important role in the sensing property.

An interesting luminescent sensor with a guest-lock-induced light-up mechanism was reported for the first time. Lang et al. prepared a MOF $([Cu_4I_4(Py_3P)_2]_n)$ with a Cu_4I_4 cluster as the node and Tris(2-pyridyl)phosphine as linker[343]. The MOF exhibits large channels that allow the guest molecules access and show weak emission attributed to the characteristic luminescence of copper iodide compounds (Fig. 32a and b). Interestingly, the luminescence is increased by chloroalkane molecules (chloroform or dichloromethane), and the luminescence of MOF was significant increased after the treatment with vapor (Fig. 32c). According to

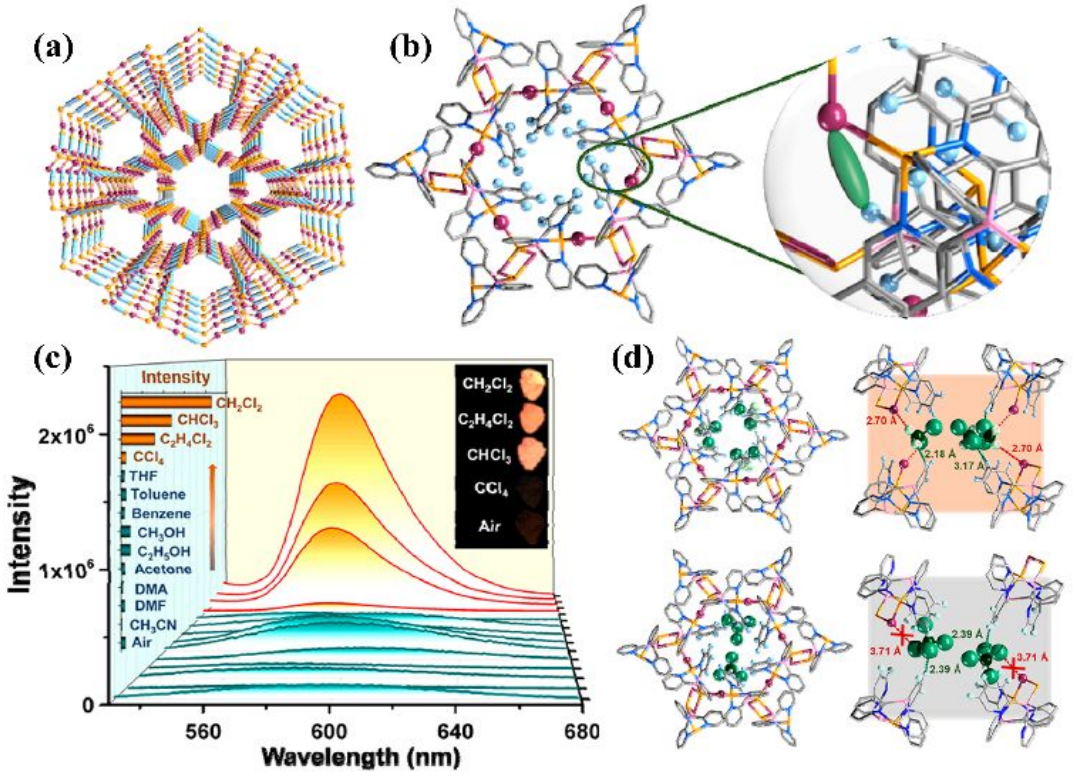

Fig. 32 (a) View of the open channels available for guest molecules along the *c*-axis. (b) Potential binding sites in the open channel. (c) Emission spectra of $[Cu_4I_4(Py_3P)_2]_n$ after an incubation for 30 min in various solvent vapors. Inset: the emission intensity of $[Cu_4I_4(Py_3P)_2]_n$ after exposure to various solvent vapors and air at 580 nm and the photographs of $[Cu_4I_4(Py_3P)_2]_n$ after an incubation for 30 min with chloroalkane vapors under UV light irradiation. (d) Close-up views of the geometries of MOF–guest complexes of CH_2Cl_2 (top panel) and CCl_4 (bottom panel) obtained from the SCXRD measurements. Colour code: orange, Cu; purple, I; dark blue, N; pink, P; grey, C; light blue, H; green, guest molecules. ref. 343 Copyright 2020, American Chemical Society.

the mechanism study, the strong hydrogen bonding interactions between guest molecules and host increase the binding to the structure. Further theoretical calculations also indicated that guest molecules will lock the vibrations of the organic ligand, and thus the nonradiative decay will be decreased and the luminescence will be increased (Fig. 32d). Han et al. prepared a Cd-MOF $\{Cd_3(L)(bbib)\cdot 6DMF\}_n$ (NBU-18, H_6L = hexa[4-(carboxyphenyl)oxamethyl]-3-oxapentane acid, bbib = 1,4-bis(1H-benzo[*d*]imidazol-1-yl)benzene) which exhibit good thermal and chemical stability[345]. The NBU-18 displays a highly selective sensing of CCl_4 vapor based on a turn-off mechanism. The *in situ* luminescence measurement reveals that the sensing response time is as short as 30 seconds and the fluorescence quenching is diffusion-controlled. The partially overlap between the adsorption bands of NBU-18 and CCl_4 indicated the energy-transfer between host framework and guest molecules may be responsible for the quenching of luminescence.

3.4.7 N,N′-Dimethylformamide

N,N′-Dimethylformamide (DMF) is not only a chemical raw material but also an excellent solvent, and thus it is widely used in industry. Currently, the most widely used method for detecting DMF vapors in the air requires a long procedure, including physical absorption/desorption of air samples and testing with gas chromatography. Recently, a convenient and fast sensing method was investigated on a platform of MOF[71,348-352].

Long et al. investigated the DMF-dependent magnetic property[71]. The authors constructed a new MOF system featuring binuclear Dy^{3+} single-molecule magnets as nodes and $Dy_2(INO)_4(NO_3)_2\cdot 2$solvent (HINO = isonicotinic acid N-oxide; solvent = DMF (Dy_2-DMF), and CH_3CN (Dy_2-CH_3CN)). Importantly, the switching of the magnetic property was achieved by the guest-induced reversible SCSC transformation (Fig. 33). The effective magnetic relaxation barriers of Dy_2-CH_3CN are 76 cm^{-1}, but only a negligible value is observed for Dy_2-DMF, resulting from different solvent

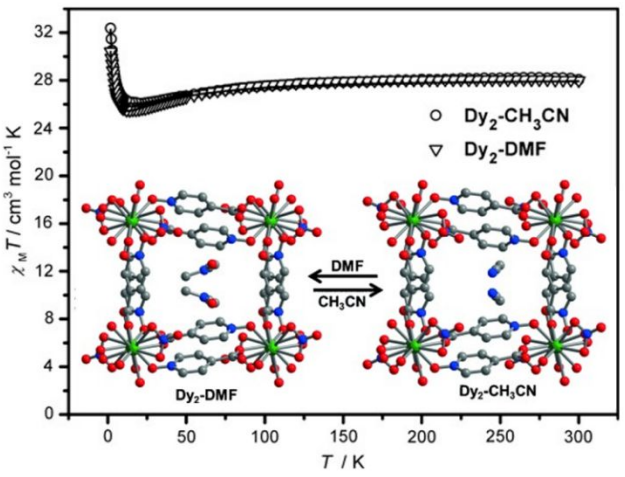

Fig. 33 Temperature dependence of the $\chi_M T$ value at 1000 Oe for Dy_2-DMF (○) and Dy_2-CH_3CN (○). Inset: Synthetic route and single-crystal to single-crystal transformation between Dy_2-DMF and Dy_2-CH_3CN. Atom colours: Dy = green, O = red, N = blue, C = grey. H atoms have been omitted for clarity. ref. 71. Copyright 2015, John Wiley and Sons.

molecules adjusting the dipole–dipole interactions and thereby tuning the relaxation rate of incoherent quantum tunnelling.

Song et al. successfully fabricated a LMOF-based DMF sensor with a luminescent LnMOF $[Eu_2L_3(H_2O)_4]\cdot 3DMF$ (L = 2′,5′-bis(methoxymethyl)-[1,1′:4′,1′′-terphenyl]-4,4′′-dicarboxylate) that exhibits excellent selectivity for DMF vapor through the luminescence turn-on response[348]. Subsequent NMR, XRD and luminescence lifetime analyses suggest that DMF-ligand interactions probably shift the excited state energy level of the ligand and therefore facilitate the LMET process, which explains the turn-on in response to DMF vapor. This study confirmed a turn-on mechanism and provided a new possibility to construct turn-on LMOF sensors using a targeting ligand and analytes through ligand-analyte interactions. Yi et al. investigated a non-fluorescent 3d-4f heterobimetallic $\{Cu_3Eu_2(PBA)_6(NO_3)_6\cdot H_2O\}_n$ (NBU-8, HPBA = 4-(pyrimidin-5-yl)benzoic acid) sensor and the fluorescence quencher Cu^{2+} ions endow CuEu-MOF non-luminescent property[349]. Interestingly, NBU-8 realizes selective luminescence recovery and fluorescence enhancement toward DMF molecules even in the presence of other amide molecules as well as other solvents containing different functional groups. Furthermore, an *in situ* luminescence measurement was implemented and the results demonstrate the diffusion-controlled detective mechanism. The NBU-8 shows high sensitivity (0.8 vol%) and fast response time (2 min) make it a promising sensor material toward DMF molecules.

Conclusions

The development of effective gas and VOC sensors has attracted great attention in the recent years due to the increasing and stringent environmental safety regulations on indoor and outdoor air quality, on various industrial processes and agro-industries, as well as for early diagnosis of diseases, to name a few. MOFs represent one of the most promising sensor materials because of their superior sensing performances as a result of large surface areas, adjustable pore sizes, tunable functional sites and interesting chemical and physical properties.

This comprehensive review highlights the recent advances in MOF sensors. The main focus is laid on electricity, magnetism, ferroelectricity and chromism based sensing of gases and VOCs, while an up-to-date information is also provided on the most recent research progress of luminescence-based MOF sensors. The different operating mechanisms of chemiresistive, magnetic, ferroelectric, colorimetric and luminescent responses in MOF-based sensing materials are elucidated in Section 2. Possible applications of MOF-based sensors for oxygen, water vapor, toxic industrial gases (such as H_2S, NH_3, SO_2, NO_x, CO_x, and CS_2) and VOCs (such as aromatic and aliphatic hydrocarbons, ketones, alcohols, and aldehydes) are discussed in Section 3, with an emphasis on the sensing performance in terms of the sensitivity, selectivity, response time, LOD and reusability.

With the emergence of EC-MOFs, chemiresistive sensing of MOFs is attracting increasing interest due to the low-cost fabrication and ease of miniaturization. However, this research field is still early in its development. There is much room to improve sensing performance of these MOF materials through exploration of novel redox-active ligands and/or guest molecules. Magnetic and ferroelectric sensing of MOFs mainly rely on SCSC transformations and have only been used as sensing switches. In addition, the success in obtaining MOF ferroelectric switches so far has been mostly accidental, due to stringent synthesis and testing conditions. As such, the available information and insight for this research field is limited but we anticipate greater efforts will be devoted to this area. Colorimetric sensors are more sensitive with lower detection limits and better selectivity due to the specific colour changes in the presence of target analytes based on host-guest interactions. Based on these advantages, the colorimetric sensor arrays for fast detection of complicated gases or VOC mixtures would be a promising future direction of MOF-based colorimetric sensors.

MOF-based luminescent sensors typically show luminescence “turn-off” or “turn-on” responses mediated by various sensing mechanisms, such as photoelectron transfer (PET), intermolecular charge transfer (ICT), resonant energy transfer (FRET) and competitive adsorption, which have been discussed in many excellent reviews. In this article, we provide a summary on MOF-based luminescent chemodosimeters and illustrate that their excellent selectivity is due to the specific organic reactions with target gases or VOCs. However, the irreversible reactions and limited target analytes increase their cost. Thus, MOF-based luminescent sensors with new sensing mechanisms need to be explored not only for improving the sensing performance and lowering the cost, but also for expanding the scope of detectable analytes. In addition, the performance of MOF-based luminescent sensors/switches can be further enhanced through the following approaches: 1) constructing LMOFs with multiple emission centres that facilitate the construction of ratiometric sensors with highly improved sensitivity and selectivity; 2) developing phosphorescent MOFs with long lifetimes to increase the sensitivity; and 3) fabricating AIE-MOFs utilizing aggregation-induced emission luminogens (AIEgens) as organic linkers to improve the sensibility, aiming at “turn-on” responses for analytes.

Currently, MOF-based gas and VOC sensors with different physical or chemical responses are relatively independent of each other. Multifunctional MOF-based materials in which two or more chemical (or physical) properties coexist or are coupled, such as chirality, porosity, luminescence, conductivity, magnetism, ferroelectricity, etc., would facilitate the development of new types of sensors. These target materials can be produced by integrating metal nodes, functional ligands and guest molecules with different properties. To date, some multifunctional MOFs with different properties, such as luminescence-electricity, luminescence-magnetism and luminescence-ferroelectricity, have been reported. However, in most of these multifunctional MOFs, different properties coexist but not correlated. Thus, further studies are needed to develop MOF-based sensors and switches that couple two or more properties and to examine their applications in multiple anti-counterfeiting and barcode sensors.

Although excellent sensing performance has been achieved for some MOF-based gas and VOC sensors and the field is rapidly expanding, many challenges for commercial applications remain to be overcome. First, a prominent challenge is to fabricate MOF-based sensing materials into workable devices. The development of MOF membranes and MOF-based thin films have come closer to practical applications, but this field is still in its nascent stages.

Second, the stability of MOFs under different environments (humidity, temperature, acidic or basic conditions, pressure, etc.) is always a key issue to consider for real-time applications. Continued efforts are necessary to design robust MOF sensors capable of retaining high performance over multiple cycles. Third, although the sensing performance of MOFs has been constantly improved under laboratory conditions further development is required to make them suitable for real-world commercial applications. Finally, the high cost of large-scale production of MOFs has substantially hampered their widespread practical applications. Clearly, great and collective efforts are essential to address these challenges, but we believe that MOF-based sensing materials have a true potential for use as gas and VOC sensors.

List of acronyms and abbreviations

4-abpt	4-Amino-3,5-bis(4-pyridyl)-1,2,4-triazole
ad	Adeninate
AIE	Aggregation-induced emission
bbib	1,4-Bis(1H-benzo[d]imidazol-1-yl)benzene
BPDC	Biphenyldicarboxylate
bpe	1,3-Bis(4-pyridyl)ethane
bpy	4,4′-bipyridine/2,2′-bipyridine
bpz	4-(3,5-Dimethylpyrazol-1-id-4-yl)-3,5-dimethyl -pyrazol-1-ide
BTD	2,1,3-Benzothiadiazole
cal	1,3-alt-25,26,27,28-tetrakis[(carboxy)methoxy]calixarene
$C_{16}O_8H_6$	Biphenyl-3,3′,5,5′-tetracarboxylic acid
dat	3,5-Diamino-1,2,4-triazole
DBB	4,4′-Di(4-benzoato)-2,2′-bipyridine
DBP-Pt	Pt-5,15-di(p-benzoato)porphyrin
DFT	Density functional theory
DMA	N,N-Dimethylacetamide
dobdc	2,5-Dioxido-1,4-benzenedicarboxylate
dptz	3,6-Di-(pyridin-4-yl)-1,2,4,5-tetrazine
EC-MOFs	Electrically conductive metal-organic frameworks
ESIPT	Excited state intramolecular proton transfer
FA	Formate
FITC	Fluorescein isothiocyanate
FRET	Förster resonant energy transfer
FUM	Fumarate
H_2abdc	2-Aminoterephthalic acid
HATP	2,3,6,7,10,11-Hexaaminotriphenylene
H_2BDC	1,3-Benzenedicarboxylic acid
H_3BTC	1,3,5-Benzenetricarboxylate
H_4BTEC	1,2,4,5-Benzenetetracarboxylic acid
H_3BTTri	1,3,5-Tris(1H-1, 2,3-triazol-5-yl)benzene
Hdetz	3,5-Diethyl-1,2,4-trizole
H_2DHBDC^{2-}	2,5-Dihydroxybenzene-1,4-dicarboxylate
H_4dhtp	2,5-Dihydroxy-terepthalic acid
H_2hpi_2cf	5-(2-(5-Fluoro-2-hydroxyphenyl)-4,5-bis(4-fluorophenyl)-1H-imidazol-1-yl)isophthalic acid)
HHTP	2,3,6,7,10,11-Hexahydroxytriphenylene
HINO	Isonicotinic acid N-oxide
Hip	1H-Imidazo-[4,5-f][1,10]phenanthroline
HITP	2,3,6,7,10,11-hexaiminotriphenylene
H_3L	Tris-(4-tetrazolyl-phenyl) amine
H_4L	N-(1,3-Dicarboxy-5-benzyl)carboxymethylglycine
H_6L	*meso*-Tetrakis(4-carboxylphenyl)porphyrin
H_6L1	(4-Carboxylatophenoxy)cyclotriphosphazene
Hmim	2-Methylimidazole
HPBA	4-(Pyrimidin-5-yl)benzoic acid
H_2pta	Terephthalic acid
HS	High spin
H_2sdba	4,4′-sulfonyldibenzoic acid
ICT	Intermolecular charge transfer
IDEs	Interdigitated electrodes
L	Tris(4-(1H-imidazol-1-yl)phenyl)amine
LLCT	Ligand-to-ligand charge transfer
LMCT	Ligand-to-metal charge transfer
Li_2Me_2Mal	Lithium dimethylmalonate
LMOFs	Luminescent metal-organic frameworks
LOD	Limit of detection
LS	Low spin
MLCT	Metal-to-ligand charge transfer
MMCT	Metal-to-metal charge transfer
MMMs	Mixed-matrix membranes
MOFs	Metal-organic frameworks
MWCNTs	Multiwalled carbon nanotubes
NIR	Near-infrared
N,S-CDs	nitrogen and sulfur-codoped carbon-based dots
pdt^{2-}	Pyrazine-2,3-dithiolate
PET	Photoelectron transfer
Py_3P	Tris(2-pyridyl)phosphine
QPDC	Quaterphenyldicarboxylate
QY	Quantum yield
RITC	Rhodamine-B isothiocyanate
SCC	Silver(I) chalcogenide/chalcogenolate clusters
SCO	Spin crossover
SCSC	Single-crystal-to-single-crystal
SIM	Single-ion magnet
SMM	Single-molecule magnet
SOFT	Self-organized frameworks on textiles
TCPE	Tetrakis(4-carboxyphenyl)ethylene
TCPP	5,10,15,20-Tetrakis-(4-carboxyphenyl)porphyrin
TDDFT	Time-dependent density functional theory
TFA	Trifluoroacetic acid
THQ	Tetrahydroxy-1,4-quinone
tipb	1,3,5-Tris(pimidazol-ylphenyl)benzene
TPE	Tetraphenylethene
tzc	Tetrazolate-5-carboxylate
UV	Ultraviolet
VOCs	Volatile organic compounds
ZIF	Zeolitic imidazolate framework

Conflicts of interest

There are no conflicts to declare.

Acknowledgements

This work was supported by the National Science Fund for Distinguished Young Scholars (21825106), the National Natural Science Foundation of China (No. 21671175, 21801227), the Program for Innovative Research Team (in Science and Technology) in Universities of Henan Province (19IRTSTHN022) and Zhengzhou University. JL acknowledges the partial support from the U.S. Department of Energy, Office of Science, Office of Basic Energy Sciences under Award DE-SC0019902.

Notes and references

1. C. He, J. Cheng, X. Zhang, M. Douthwaite, S. Pattisson and Z. Hao, *Chem. Rev.*, 2019, **119**, 4471-4568.
2. E. Barea, C. Montoro and J. A. R. Navarro, *Chem. Soc. Rev.*, 2014, **43**, 5419-5430.
3. M. Woellner, S. Hausdorf, N. Klein, P. Mueller, M. W. Smith and S. Kaskel, *Adv. Mater.*, 2018, **30**, 1704679.
4. T. Rasheed and F. Nabeel, *Coord. Chem. Rev.*, 2019, **401**, 213065.
5. O. S. Wenger, *Chem. Rev.*, 2013, **113**, 3686-3733.
6. H. Wang, W. P. Lustig and J. Li, *Chem. Soc. Rev.*, 2018, **47**, 4729-4756.
7. M. Eddaoudi, J. Kim, N. Rosi, D. Vodak, J. Wachter, M. O'Keeffe and O. M. Yaghi, *Science*, 2002, **295**, 469-472.
8. A. Schoedel, M. Li, D. Li, M. O'Keeffe and O. M. Yaghi, *Chem. Rev.*, 2016, **116**, 12466-12535.
9. T. Tian, Z. Zeng, D. Vulpe, M. E. Casco, G. Divitini, P. A. Midgley, J. Silvestre-Albero, J.-C. Tan, P. Z. Moghadam and D. Fairen-Jimenez, *Nat. Mater.*, 2018, **17**, 174-179.
10. M. Zhao, K. Yuan, Y. Wang, G. Li, J. Guo, L. Gu, W. Hu, H. Zhao and Z. Tang, *Nature*, 2016, **539**, 76-80.
11. C. Avci, I. Imaz, A. Carné-Sánchez, J. A. Pariente, N. Tasios, J. Pérez-Carvajal, M. I. Alonso, A. Blanco, M. Dijkstra, C. López and D. Maspoch, *Nat. Chem.*, 2017, **10**, 78-84.
12. A. Cadiau, K. Adil, P. M. Bhatt, Y. Belmabkhout and M. Eddaoudi, *Science*, 2016, **353**, 137-140.
13. A. M. Rice, C. R. Martin, V. A. Galitskiy, A. A. Berseneva, G. A. Leith and N. B. Shustova, *Chem. Rev.*, 2019, DOI: 10.1021/acs.chemrev.9b00350.
14. A. Kirchon, L. Feng, H. F. Drake, E. A. Joseph and H.-C. Zhou, *Chem. Soc. Rev.*, 2018, **47**, 8611-8638.
15. E. Li, K. Jie, M. Liu, X. Sheng, W. Zhu and F. Huang, *Chem. Soc. Rev.*, 2020, **49**, 1517-1544.
16. B. Li, H.-T. Fan, S.-Q. Zang, H.-Y. Li and L.-Y. Wang, *Coord. Chem. Rev.*, 2018, **377**, 307-329.
17. M. Pan, W.-M. Liao, S.-Y. Yin, S.-S. Sun and C.-Y. Su, *Chem. Rev.*, 2018, **118**, 8889-8935.
18. C.-Y. Sun, X.-L. Wang, X. Zhang, C. Qin, P. Li, Z. M. Su, D.-X. Zhu, G.-G. Shan, K.-Z. Shao, H. Wu and J. Li, *Nat. Commun.*, 2013, **4**, 2717.
19. H.-Q. Yin and X.-B. Yin, *Acc. Chem. Res.*, 2020, **53**, 485-495.
20. G. M. Espallargas and E. Coronado, *Chem. Soc. Rev.*, 2018, **47**, 533-557.
21. A. E. Thorarinsdottir and T. D. Harris, *Chem. Rev.*, 2020, DOI: 10.1021/acs.chemrev.9b00666.
22. C. Yang, R. Dong, M. Wang, P. S. Petkov, Z. Zhang, M. Wang, P. Han, M. Ballabio, S. A. Bräuninger, Z. Liao, J. Zhang, F. Schwotzer, E. Zschech, H. H. Klauss, E. Cánovas, S. Kaskel, M. Bonn, S. Zhou, T. Heine and X. Feng, *Nat. Commun.*, 2019, **10**, 3260.
23. X. Xiao, L. Zou, H. Pang and Q. Xu, *Chem. Soc. Rev.*, 2020, **49**, 301-331.
24. H.-F. Wang, L. Chen, H. Pang, S. Kaskel and Q. Xu, *Chem. Soc. Rev.*, 2020, **49**, 1414-1448.
25. A. A. Talin, A. Centrone, A. C. Ford, M. E. Foster, V. Stavila, P. Haney, R. A. Kinney, V. Szalai, F. E. Gabaly, H. P. Yoon, F. Léonard and M. D. Allendorf, *Science*, 2014, **343**, 66-69.
26. R. Dong, P. Han, H. Arora, M. Ballabio, M. Karakus, Z. Zhang, C. Shekhar, P. Adler, P. S. Petkov, A. Erbe, S. C. B. Mannsfeld, C. Felser, T. Heine, M. Bonn, X. Feng and E. Cánovas, *Nat. Mater.*, 2018, **17**, 1027-1032.
27. A. Pathak, J.-W. Shen, M. Usman, L.-F. Wei, S. Mendiratta, Y.-S. Chang, B. Sainbileg, C.-M. Ngue, R.-S. Chen, M. Hayashi, T.-T. Luo, F.-R. Chen, K.-H. Chen, T.-W. Tseng, L.-C. Chen and K.-L. Lu, *Nat. Commun.*, 2019, **10**, 1721.
28. W. Zhang and R.-G. Xiong, *Chem. Rev.*, 2012, **112**, 1163-1195.
29. M. Mon, J. Ferrando-Soria, M. Verdaguer, C. Train, C. Paillard, B. Dkhil, C. Versace, R. Bruno, D. Armentano and E. Pardo, *J. Am. Chem. Soc.*, 2017, **139**, 8098-8101.
30. H. Furukawa, K. E. Cordova, M. O'Keeffe and O. M. Yaghi, *Science*, 2013, **341**, 1230444.
31. T. Rodenas, I. Luz, G. Prieto, B. Seoane, H. Miro, A. Corma, F. Kapteijn, F. X. Llabres i Xamena and J. Gascon, *Nat. Mater.*, 2015, **14**, 48-55.
32. M. Ding, R. W. Flaig, H.-L. Jiang and O. M. Yaghi, *Chem. Soc. Rev.*, 2019, **48**, 2783-2828.
33. B. Li, H.-M. Wen, W. Zhou, J. Q. Xu and B. Chen, *Chem*, 2016, **1**, 557-580.
34. C. A. Trickett, T. M. Osborn Popp, J. Su, C. Yan, J. Weisberg, A. Huq, P. Urban, J. Jiang, M. J. Kalmutzki, Q. Liu, J. Baek, M. P. Head-Gordon, G. A. Somorjai, J. A. Reimer and O. M. Yaghi, *Nat. Chem.*, 2019, **11**, 170-176.
35. Q. Wang and D. Astruc, *Chem. Rev.*, 2020, **120**, 1438-1511.
36. A. Dhakshinamoorthy, Z. Li and H. Garcia, *Chem. Soc. Rev.*, 2018, **47**, 8134-8172.
37. Q. Yang, Q. Xu and H.-L. Jiang, *Chem. Soc. Rev.*, 2017, **46**, 4774-4808.
38. D. Li, M. Kassymova, X. Cai, S.-Q. Zang and H.-L. Jiang, *Coord. Chem. Rev.*, 2020, **412**, 213262.
39. V. Stavila, A. A. Talin and M. D. Allendorf, *Chem. Soc. Rev.*, 2014, **43**, 5994-6010.
40. W. P. Lustig and J. Li, *Coord. Chem. Rev.*, 2018, **373**, 116-147.
41. Y. Cui, J. Zhang, H. He and G. Qian, *Chem. Soc. Rev.*, 2018, **47**, 5740-5785.
42. Y. Cui, Y. Yue, G. Qian and B. Chen, *Chem. Rev.*, 2012, **112**, 1126-1162.
43. H. Zhang, J. Hou, Y. Hu, P. Wang, R. Ou, L. Jiang, J. Z. Liu, B. D. Freeman, A. J. Hill and H. Wang, *Sci. Adv.*, 2018, **4**, eaaq0066.
44. J. Zhou and B. Wang, *Chem. Soc. Rev.*, 2017, **46**, 6927-6945.
45. L. Kong, M. Zhong, W. Shuang, Y. Xu and X.-H. Bu, *Chem. Soc. Rev.*, 2020, **49**, 2378-2407.
46. H. Wang, Q.-L. Zhu, R. Zou and Q. Xu, *Chem*, 2017, **2**, 52-80.
47. S. Yuan, L. Feng, K. Wang, J. Pang, M. Bosch, C. Lollar, Y. Sun, J. Qin, X. Yang, P. Zhang, Q. Wang, L. Zou, Y. Zhang, L, Zhang, Y. Fang, J. Li and H.-C. Zhou, *Adv. Mater.*, 2018, **30**, 1704303.
48. M. Ding, X. Cai and H.-L. Jiang, *Chem. Sci.*, 2019, **10**, 10209-10230.
49. L. E. Kreno, K. Leong, O. K. Farha, M. Allendorf, R. P. Van Duyne and J. T. Hupp, *Chem. Rev.*, 2012, **112**, 1105-1125.
50. W.-T. Koo, J.-S. Jang and I.-D. Kim, *Chem*, 2019, **5**, 1938-1963.
51. D. J. Wales, J. Grand, V. P. Ting, R. D. Burke, K. J. Edler, C. R. Bowen, S. Mintova and A. D. Burrows, *Chem. Soc. Rev.*, 2015, **44**, 4290-4321.
52. Z. Hu, B. J. Deibert and J. Li, *Chem. Soc. Rev.*, 2014, **43**, 5815-5840.
53. W. P. Lustig, S. Mukherjee, N. D. Rudd, A. V. Desai, J. Li and S. K. Ghosh, *Chem. Soc. Rev.*, 2017, **46**, 3242-3285.
54. X.-D. Wang and O. S. Wolfbeis, *Chem. Soc. Rev.*, 2014, **43**, 3666-3761.
55. N. S. Bobbitt, M. L. Mendonca, A. J. Howarth, T. Islamoglu, J. T. Hupp, O. K. Farha and R. Q. Snurr, *Chem. Soc. Rev.*, 2017, **46**, 3357-3385.
56. I. Stassen, N. Burtch, A. Talin, P. Falcaro, M. Allendorf and R. Ameloot, *Chem. Soc. Rev.*, 2017, **46**, 3185-3241.
57. R.-B. Lin, S.-Y. Liu, J.-W. Ye, X.-Y. Li and J.-P. Zhang, *Adv. Sci.*, 2016, **3**, 1500434.
58. B. Yan, *Acc. Chem. Res.*, 2017, **50**, 2789-2798.
59. A. Karmakar, P. Samanta, A. V. Desai and S. K. Ghosh, *Acc. Chem. Res.*, 2017, **50**, 2457-2469.
60. E. A. Dolgopolova, A. M. Rice, C. R. Martin and N. B. Shustova, *Chem. Soc. Rev.*, 2018, **47**, 4710-4728.
61. D. Zhao, Y. Cui, Y. Yang and G. Qian, *CrystEngComm*, 2016, **18**, 3746-3759.

62. L. Sun, M. G. Campbell and M. Dincă, *Angew. Chem. Int. Ed.*, 2016, **55**, 3566-3579.
63. Z. Meng, R. M. Stolz, L. Mendecki and K. A. Mirica, *Chem. Rev.*, 2019, **119**, 478-598.
64. M. G. Campbell and M. Dincă, *Sensors*, 2017, **17**, 1108.
65. M. A. H. Khan, M. V. Rao and Q. Li, *Sensors*, 2019, **19**, 905.
66. L. Liu, Y. Zhou, S. Liu and M. Xu, *ChemElectroChem*, 2018, **5**, 6-19.
67. W.-H. Li, W.-H. Deng, G.-E. Wang and G. Xu, *EnergyChem*, 2020, **2**, 100029.
68. C.-S. Liu, J. Li and H. Pang, *Coord. Chem. Rev.*, 2020, **410**, 213222.
69. A. Chidambaram and K. C. Stylianou, *Inorg. Chem. Front.*, 2018, **5**, 979-998.
70. J.-P. Zhang, P.-Q. Liao, H.-L. Zhou, R.-B. Lin and X.-M. Chen, *Chem. Soc. Rev.*, 2014, **43**, 5789-5814.
71. X. Zhang, V. Vieru, X. Feng, J.-L. Liu, Z. Zhang, B. Na, W. Shi, B.-W. Wang, A. K. Powell, L. F. Chibotaru, S. Gao, P. Cheng and J. R. Long, *Angew. Chem. Int. Ed.*, 2015, **54**, 9861-9865.
72. Y. Xin, J. Wang, M. Zychowicz, J. J. Zakrzewski, K. Nakabayashi, B. Sieklucka, S. Chorazy and S.-I. Ohkoshi, *J. Am. Chem. Soc.*, 2019, **141**, 18211-18220.
73. Z.-P. Ni, J.-L. Liu, M. N. Hoque, W. Liu, J.-Y. Li, Y.-C. Chen and M.-L. Tong, *Coord. Chem. Rev.*, 2017, **335**, 28-43.
74. M. Wriedt, A. A. Yakovenko, G. J. Halder, A. V. Prosvirin, K. R. Dunbar and H.-C. Zhou, *J. Am. Chem. Soc.*, 2013, **135**, 4040-4050.
75. X.-Y. Dong, B. Li, B.-B. Ma, S.-J. Li, M.-M. Dong, Y.-Y. Zhu, S.-Q. Zang, Y. Song, H.-W. Hou and T. C. W. Mak, *J. Am. Chem. Soc.*, 2013, **135**, 10214-10217.
76. S. Bhattacharya, S. Pal and S. Natarajan, *ChemPlusChem*, 2016, **81**, 733-742.
77. S.-L. Li, M. Han, Y. Zhang, G.-P. Li, M. Li, G. He and X.-M. Zhang, *J. Am. Chem. Soc.*, 2019, **141**, 12663-12672.
78. J. Zhang, J. Ouyang, Y. Ye, Z. Li, Q. Lin, T. Chen, Z. Zhang and S. Xiang, *ACS Appl. Mater. Interfaces*, 2018, **10**, 27465-27471.
79. X.-P. Zhou, Z. Xu, J. He, M. Zeller, A. D. Hunter, R. Clerac, C. Mathoniere, S. S. Chui and C.-M. Che, *Inorg. Chem.*, 2010, **49**, 10191-10198.
80. Y. Zhang, S. Yuan, G. Day, X. Wang, X. Yang and H.-C. Zhou, *Coord. Chem. Rev.*, 2018, **354**, 28-45.
81. S. Wu, H. Min, W. Shi and P. Cheng, *Adv. Mater.*, 2020, **32**, 1805871.
82. F.-Y. Yi, D. Chen, M.-K. Wu, L. Han and H.-L. Jiang, *ChemPlusChem*, 2016, **81**, 675-690.
83. J. He, J. Xu, J. Yin, N. Li and X.-H. Bu, *Sci. China Mater.*, 2019, **62**, 1655-1678.
84. L. Chen, J.-W. Ye, H.-P. Wang, M. Pan, S.-Y. Yin, Z.-W. Wei, L.-Y. Zhang, K. Wu, Y.-N. Fan and C.-Y. Su, *Nat. Commun.*, 2017, **8**, 15985.
85. J.-W. Ye, H.-L. Zhou, S.-Y. Liu, X.-N. Cheng, R.-B. Lin, X.-L. Qi, J.-P. Zhang and X.-M. Chen, *Chem. Mater.*, 2015, **27**, 8255-8260.
86. J. Yang, Z. Wang, Y. Li, Q. Zhuang and J. Gu, *Chem. Mater.*, 2016, **28**, 2652-2658.
87. W. Zhang, D. Wang, L. Zhu, F. Zhai, L. Weng, J. Sun, Y. Ling, Z. Chen and Y. Zhou, *Dalton Trans.*, 2016, **45**, 10510-10513.
88. J. Zhang, W.-B. Yang, X.-Y. Wu, X.-F. Kuang and C.-Z. Lu, *Dalton Trans.*, 2015, **44**, 13586-13591.
89. C.-W. Zhao, J.-P. Ma, Q.-K. Liu, X.-R. Wang, Y. Liu, J. Yang, J.-S. Yang and Y.-B. Dong, *Chem. Commun.*, 2016, **52**, 5238-5241.
90. R.-W. Huang, Y.-S. Wei, X.-Y. Dong, X.-H. Wu, C.-X. Du, S.-Q. Zang and T. C. W. Mak, *Nat. Chem.*, 2017, **9**, 689-697.
91. X.-Y. Dong, H.-L. Huang, J.-Y. Wang, H.-Y. Li and S.-Q. Zang, *Chem. Mater.*, 2018, **30**, 2160-2167.
92. X.-H. Wu, P. Luo, Z. Wei, Y.-Y. Li, R.-W. Huang, X.-Y. Dong, K. Li, S.-Q. Zang and B. Z. Tang, *Adv. Sci.*, 2019, **6**, 1801304.
93. M. K. Smith and K. A. Mirica, *J. Am. Chem. Soc.*, 2017, **139**, 16759-16767.
94. M. K. Smith, K. E. Jensen, P. A. Pivak and K. A. Mirica, *Chem. Mater.*, 2016, **28**, 5264-5268.
95. M. G. Campbell, D. Sheberla, S. F. Liu, T. M. Swager and M. Dincă, *Angew. Chem. Int. Ed.*, 2015, **54**, 4349-4352.
96. M.-S. Yao, J.-J. Zheng, A.-Q. Wu, G. Xu, S. S. Nagarkar, G. Zhang, M. Tsujimoto, S. Sakaki, S. Horike, K. Otake and S. Kitagawa, *Angew. Chem. Int. Ed.*, 2020, **59**, 172-176.
97. M.-S. Yao, X.-J. Lv, Z.-H. Fu, W.-H. Li, W.-H. Deng, G.-D. Wu and G. Xu, *Angew. Chem. Int. Ed.*, 2017, **56**, 16510-16514.
98. V. Rubio-Giménez, N. Almora-Barrios, G. Escorcia-Ariza, M. Galbiati, M. Sessolo, S. Tatay and C. Martí-Gastaldo, *Angew. Chem. Int. Ed.*, 2018, **57**, 15086-15090.
99. M. G. Campbell, S. F. Liu, T. M. Swager and M. Dincă, *J. Am. Chem. Soc.*, 2015, **137**, 13780-13783.
100. E.-X. Chen, H. Yang and J. Zhang, *Inorg. Chem.*, 2014, **53**, 5411-5413.
101. M.-S. Yao, J.-W. Xiu, Q.-Q. Huang, W.-H. Li, W.-W. Wu, A.-Q. Wu, L.-A. Cao, W.-H. Deng, G.-E. Wang and G. Xu, *Angew. Chem. Int. Ed.*, 2019, **58**, 14915-14919.
102. L.-F. Wang, W.-M. Zhuang, G.-Z. Huang, Y.-C. Chen, J.-Z. Qiu, Z.-P. Ni and M.-L. Tong, *Chem. Sci.*, 2019, **10**, 7496-7502.
103. A. Tissot, X. Kesse, S. Giannopoulou, I. Stenger, L. Binet, E. Riviere and C. Serre, *Chem. Commun.*, 2018, **55**, 194-197.
104. D. Shao, L. Shi, L. Yin, B.-L. Wang, Z.-X. Wang, Y.-Q. Zhang and X.-Y. Wang, *Chem. Sci.*, 2018, **9**, 7986-7991.
105. J. E. Clements, P. R. Airey, F. Ragon, V. Shang, C. J. Kepert and S. M. Neville, *Inorg. Chem.*, 2018, **57**, 14930-14938.
106. D.-Q. Wu, D. Shao, X.-Q. Wei, F.-X. Shen, L. Shi, D. Kempe, Y.-Z. Zhang, K. R. Dunbar and X.-Y. Wang, *J. Am. Chem. Soc.*, 2017, **139**, 11714-11717.
107. S. Chorazy, J. J. Zakrzewski, M. Reczyński, K. Nakabayashi, S.-i. Ohkoshi and B. Sieklucka, *J. Mater. Chem. C*, 2019, **7**, 4164-4172.
108. J. Vallejo, F. R. Fortea-Pérez, E. Pardo, S. Benmansour, I. Castro, J. Krzystek, D. Armentano and J. Cano, *Chem. Sci.*, 2016, **7**, 2286-2293.
109. J.-Y. Ge, L. Cui, J. Li, F. Yu, Y. Song, Y.-Q. Zhang, J.-L. Zuo and M. Kurmoo, *Inorg. Chem.*, 2017, **56**, 336-343.
110. Q. Chen, Z. Chang, W.-C. Song, H. Song, H.-B. Song, T.-L. Hu and X.-H. Bu, *Angew. Chem. Int. Ed.*, 2013, **52**, 11550-11553.
111. L.-H. Cao, Y.-S. Wei, H. Xu, S.-Q. Zang and T. C. W. Mak, *Adv. Funct. Mater.*, 2015, **25**, 6448-6457.
112. A. M. Ullman, C. G. Jones, F. P. Doty, V. Stavila, A. A. Talin and M. D. Allendorf, *ACS Appl. Mater. Interfaces*, 2018, **10**, 24201-24208.
113. Y. Yu, X.-M. Zhang, J.-P. Ma, Q.-K. Liu, P. Wang and Y.-B. Dong, *Chem. Commun.*, 2014, **50**, 1444-1446.
114. J. Cui, Y.-L. Wong, M. Zeller, A. D. Hunter and Z. Xu, *Angew. Chem. Int. Ed.*, 2014, **53**, 14438-14442.
115. A- Gładysiak, T. N. Nguyen, J. A. R. Navarro, M. J. Rosseinsky and K. C. Stylianou, *Chem. Eur. J.*, 2017, **23**, 13602-13606.
116. R. Li, X. Ren, H. Ma, X. Feng, Z. Lin, X. Li, C. Hu and B. Wang, *J. Mater. Chem. A*, 2014, **2**, 5724-5729.
117. L. Li, X. Jiao, D. Chen, B. V. Lotsch and C. Li, *Chem. Mater.*, 2015, **27**, 7601-7609.
118. W. Shi, F. Xing, Y.-L. Bai, M. Hu, Y. Zhao, M. X. Li and S. Zhu, *ACS Appl. Mater. Interfaces*, 2015, **7**, 14493-14500.
119. C. Zhang, L. Sun, Y. Yan, Y. Liu, Z. Liang, Y. Liu and J. Li, *J. Mater. Chem. C*, 2017, **5**, 2084-2089.
120. Y.-N. Gong and T.-B. Lu, *Chem. Commun.*, 2013, **49**, 7711-7713.
121. S.-L. Li, M. Han, B. Wu, J. Wang and X.-M. Zhang, *Cryst. Growth Des.*, 2018, **18**, 3883-3889.
122. Z. Dou, J. Yu, Y. Cui, Y. Yang, Z. Wang, D. Yang and G. Qian, *J. Am. Chem. Soc.*, 2014, **136**, 5527-5530.
123. Y. Zhang and B. Yan, *J. Mater. Chem. C*, 2019, **7**, 5652-5657.
124. S. Han, H. Kim, J. Kim and Y. Jung, *Phys. Chem. Chem. Phys.*, 2015, **17**, 16977-16982.

125. J. Park, H. Kim and Y. Jung, *J. Phys. Chem. Lett.*, 2013, **4**, 2530-2534.
126. K. Y. Zhang, P. Gao, G. Sun, T. Zhang, X. Li, S. Liu, Q. Zhao, K. K. Lo and W. Huang, *J. Am. Chem. Soc.*, 2018, **140**, 7827-7834.
127. Z. Xie, L. Ma, K. E. deKrafft, A. Jin, and W. Lin, *J. Am. Chem. Soc.*, 2010, **132**, 922-923.
128. R. Xu, Y. Wang, X. Duan, K. Lu, D. Micheroni, A. Hu and W. Lin, *J. Am. Chem. Soc.*, 2016, **138**, 2158-2161.
129. G. Lan, K. Ni, E. You, M. Wang, A. Culbert, X. Jiang and W. Lin, *J. Am. Chem. Soc.*, 2019, **141**, 18964-18969.
130. Y.-T. Chen, C.-Y. Lin, G.-H. Lee and M.-L. Ho, *CrystEngComm*, 2015, **17**, 2129-2140.
131. R.-B. Lin, F. Li, S.-Y. Liu, X.-L. Qi, J.-P. Zhang and X.-M. Chen, *Angew. Chem. Int. Ed.*, 2013, **52**, 13429-13433.
132. X.-L. Qi, S.-Y. Liu, R.-B. Lin, P.-Q. Liao, J.-W. Ye, Z. Lai, Y. Guan, X.-N. Cheng, J.-P. Zhang and X.-M. Chen, *Chem. Commun.*, 2013, **49**, 6864-6866.
133. H.-L. Zhou, J. Bai, J.-W. Ye, Z.-W. Mo, W.-X. Zhang, J.-P. Zhang and X.-M. Chen, *ChemPlusChem*, 2016, **81**, 817-821.
134. R.-B. Lin, H.-L. Zhou, C.-T. He, J.-P. Zhang and X.-M. Chen, *Inorg. Chem. Front.*, 2015, **2**, 1085-1090.
135. G.-Y. Zhang, C. Cai, S. Cosnier, H.-B. Zeng, X.-J. Zhang and D. Shan, *Nanoscale*, 2016, **8**, 11649-11657.
136. S.-Y. Liu, X.-L. Qi, R.-B. Lin, X.-N. Cheng, P.-Q. Liao, J.-P. Zhang and X.-M. Chen, *Adv. Funct. Mater.*, 2014, **24**, 5866-5872.
137. S.-Y. Liu, D.-D. Zhou, C.-T. He, P.-Q. Liao, X.-N. Cheng, Y.-T. Xu, J.-W. Ye, J.-P. Zhang and X.-M. Chen, *Angew. Chem. Int. Ed.*, 2016, **55**, 16021-16025.
138. Y. Xu, S.-Y. Liu, J. Li, L. Zhang, D. Chen, J.-P. Zhang, Y. Xu, Z. Dai and X. Zou, *Anal. Chem.*, 2018, **90**, 9330-9337.
139. Y. Xu, S.-Y. Liu, J. Liu, L. Zhang, D. Chen, J. Chen, Y. Ma, J.-P. Zhang, Z. Dai and X. Zou, *Chem. Eur. J.*, 2019, **25**, 5463-5471.
140. D. Wang, W. Zhang, J. Sun, Y. Ling, Z. Chen and Y. Zhou, *ChemistrySelect*, 2016, **1**, 1917-1920.
141. J. An, C. M. Shade, D. A. Chengelis-Czegan, S. Petoud and N. L. Rosi, *J. Am. Chem. Soc.*, 2011, **133**, 1220-1223.
142. J.-W. Ye, J.-M. Lin, Z.-W. Mo, C.-T. He, H.-L. Zhou, J.-P. Zhang and X.-M. Chen, *Inorg. Chem.*, 2017, **56**, 4238-4243.
143. H. Weng, X.-Y. Xu and B. Yan, *J. Colloid Interface Sci.*, 2017, **502**, 8-15.
144. X.-Y. Xu and B. Yan, *J. Mater. Chem. C*, 2016, **4**, 8514-8521.
145. Q.-L. Wang, H. Southerland, J.-R. Li, A. V. Prosvirin, H. Zhao and K. R. Dunbar, *Angew. Chem. Int. Ed.*, 2012, **51**, 9321-9324.
146. Z.-Y. Li, X.-J. Li, X. Gao, F.-L. Zhang, C. Zhang and B. Zhai, *Cryst. Growth Des.*, 2020, **20**, 1103-1109.
147. E. N. Zorina-Tikhonova, N. V. Gogoleva, A. A. Sidorov, M. A. Kiskin, S. V. Kolotilov, T. M. Ivanova, K. I. Maslakov, Z. V. Dobrokhotova, N. N. Efimov, V. M. Novotortsev and I. L. Eremenko, *Eur. J. Inorg. Chem.*, 2017, **2017**, 1396-1405.
148. F. Ma, J. Xiong, Y.-S. Meng, J. Yang, H.-L. Sun and S. Gao, *Inorg. Chem. Front.*, 2018, **5**, 2875-2884.
149. Q. Zhou, F. Yang, B. Xin, G. Zeng, X. Zhou, K. Liu, D. Ma, G. Li, Z. Shi and S. Feng, *Chem. Commun.*, 2013, **49**, 8244-8246.
150. C. Qiao, L. Sun, S. Zhang, P. Liu, L. Chang, C. Zhou, Q. Wei, S. Chen and S. Gao, *J. Mater. Chem. C*, 2017, **5**, 1064-1073.
151. L. Pan, G. Liu, H. Li, S. Meng, L. Han, J. Shang, B. Chen, A. E. Platero-Prats, W. Lu, X. Zou and R.-W. Li, *J. Am. Chem. Soc.*, 2014, **136**, 17477-17483.
152. S. Nakatsuka, Y. Watanabe, Y. Kamakura, S. Horike, D. Tanaka and T. Hatakeyama, *Angew. Chem. Int. Ed.*, 2020, **59**, 1435-1439.
153. S. G. Dunning, A. J. Nuñez, M. D. Moore, A. Steiner, V. M. Lynch, J. L. Sessler, B. J. Holliday and S. M. Humphrey, *Chem*, 2017, **2**, 579-589.
154. Y. Dong, J. Cai, Q. Fang, X. You and Y. Chi, *Anal. Chem.*, 2016, **88**, 1748-1752.
155. Z. Wang, C.-Y. Zhu, Z.-W. Wei, Y.-N. Fan and M. Pan, *Chem. Mater.*, 2019, **32**, 841-848.
156. H.-Q. Yin, J.-C. Yang and X.-B. Yin, *Anal. Chem.*, 2017, **89**, 13434-13440.
157. B. Li, W. Wang, Z. Hong, E. M. El-Sayed and D. Yuan, *Chem. Commun.*, 2019, **55**, 6926-6929.
158. A. Douvali, A. C. Tsipis, S. V. Eliseeva, S. Petoud, G. S. Papaefstathiou, C. D. Malliakas, I. Papadas, G. S. Armatas, I. Margiolaki, M. G. Kanatzidis, T. Lazarides and M. J. Manos, *Angew. Chem. Int. Ed.*, 2015, **54**, 1651-1656.
159. J. M. Seco, E. San Sebastián, J. Cepeda, B. Biel, A. Salinas-Castillo, B. Fernández, D. P. Morales, M. Bobinger, S. Gómez-Ruiz, F. C. Loghin, A. Rivadeneyra and A. Rodriguez-Diéguez, *Sci. Rep.*, 2018, **8**, 14414.
160. F. Drache, V. Bon, I. Senkovska, M. Adam, A. Eychmüller and S. Kaskel, *Eur. J. Inorg. Chem.*, 2016, **2016**, 4483-4489.
161. J. M. Stangl, D. Dietrich, A. E. Sedykh, C. Janiak and K. Müller-Buschbaum, *J. Mater. Chem. C*, 2018, **6**, 9248-9257.
162. D. Wang, Q. Tan, J. Liu and Z. Liu, *Dalton Trans.*, 2016, **45**, 18450-18454.
163. J.-X. Wu and B. Yan, *Dalton Trans.*, 2017, **46**, 7098-7105.
164. T. Wehner, M. T. Seuffert, J. R. Sorg, M. Schneider, K. Mandel, G. Sextl and K. Müller-Buschbaum, *J. Mater. Chem. C*, 2017, **5**, 10133-10142.
165. Y. Zhou, D. Zhang, W. Xing, J. Cuan, Y. Hu, Y. Cao and N. Gan, *Anal. Chem.*, 2019, **91**, 4845-4851.
166. Z. Zhou, M.-X. Li, L. Wang, X. He, T. Chi and Z.-X. Wang, *Cryst. Growth Des.*, 2017, **17**, 6719-6724.
167. D. Zhang, H. Chen, X. Zhou, D. Wang, Y. Jin and S. Yu, *Sens. Actuators, A*, 2019, **295**, 687-695.
168. K. N. Chappanda, O. Shekhah, O. Yassine, S. P. Patole, M. Eddaoudi and K. N. Salama, *Sens. Actuators B*, 2018, **257**, 609-619.
169. A. Weiss, N. Reimer, N. Stock, M. Tiemann and T. Wagner, *Micro. Mesoporous Mater.*, 2016, **220**, 39-43.
170. P.-G. Su and X.-H. Lee, *Sens. Actuators B*, 2018, **269**, 110-117.
171. A. Weiss, N. Reimer, N. Stock, M. Tiemann and T. Wagner, *Phys. Chem. Chem. Phys.*, 2015, **17**, 21634-21642.
172. K. Roztocki, F. Formalik, A. Krawczuk, I. Senkovska, B. Kuchta, S. Kaskel and D. Matoga, *Angew. Chem. Int. Ed.*, 2020, **59**, 4491-4497.
173. C. Sapsanis, H. Omran, V. Chernikova, O. Shekhah, Y. Belmabkhout, U. Buttner, M. Eddaoudi and K. N. Salama, *Sensors*, 2015, **15**, 18153-18166.
174. M. Tian, Z.-H. Fu, B. Nath and M.-S. Yao, *RSC Adv.*, 2016, **6**, 88991-88995.
175. Y.-L. Liu and W. Zhang, *Chem. Commun.*, 2017, **53**, 6077-6080.
176. M. S. Shah, M. Tsapatsis and J. I. Siepmann, *Chem. Rev.*, 2017, **117**, 9755-9803.
177. R. Dalapati, S. N. Balaji, V. Trivedi, L. Khamari and S. Biswas, *Sens. Actuators B*, 2017, **245**, 1039-1049.
178. M. Hmadeh, Z. Lu, Z. Liu, F. Gándara, H. Furukawa, S. Wan, V. Augustyn, R. Chang, L. Liao, F. Zhou, E. Perre, V. Ozolins, K. Suenaga, X. Duan, B. Dunn, Y. Yamamto, O. Terasaki and O. M. Yaghi, *Chem. Mater.*, 2012, **24**, 3511-3513.
179. X. Zhang, Q. Zhang, D. Yue, J. Zhang, J. Wang, B. Li, Y. Yang, Y. Cui and G. Qian, *Small*, 2018, **14**, 1801563.
180. Y. Ma, H. Su, X. Kuang, X. Li, T. Zhang and B. Tang, *Anal. Chem.*, 2014, **86**, 11459-11463.
181. X. Zhang, Q. Hu, T. Xia, J. Zhang, Y. Yang, Y. Cui, B. Chen and G. Qian, *ACS Appl. Mater. Interfaces*, 2016, **8**, 32259-32265.
182. P. Ling, C. Qian, J. Yu and F. Gao, *Chem. Commun.*, 2019, **55**, 6385-6388.
183. S. S. Nagarkar, T. Saha, A. V. Desai, P. Talukdar and S. K. Ghosh, *Sci. Rep.*, 2014, **4**, 7053.
184. J. Zhang, F. Liu, J. Gan, Y. Cui, B. Li, Y. Yang and G. Qian, *Sci. China Mater.*, 2019, **62**, 1445-1453.
185. R. Song, L. Hou, Y. Wang, Y. Li, X. Wang, Y. Zang, Y. Zang, X. Wang and S. Yan, *Anal. Methods*, 2017, **9**, 3914-3919.

186. X. Zheng, R. Fan, Y. Song, A. Wang, K. Xing, X. Du, P. Wang and Y. Yang, *J. Mater. Chem. C*, 2017, **5**, 9943-9951.
187. A. Buragohain and S. Biswas, *CrystEngComm*, 2016, **18**, 4374-4381.
188. X. Zhang, J. Zhang, Q. Hu, Y. Cui, Y. Yang and G. Qian, *Appl. Surf. Sci.*, 2015, **355**, 814-819.
189. Y. Li, X. Zhang, L. Zhang, K. Jiang, Y. Cui, Y. Yang and G. Qian, *J. Solid State Chem.*, 2017, **255**, 97-101.
190. H. Li, X. Feng, Y. Guo, D. Chen, R. Li, X. Ren, X. Jiang, Y. Dong and B. Wang, *Sci. Rep.*, 2014, **4**, 4366.
191. C. Zong, X. Liu, H. Sun, G. Zhang and L. Lu, *J. Mater. Chem.*, 2012, **22**, 18418.
192. S. Nandi, S. Banesh, V. Trivedi and S. Biswas, *Analyst*, 2018, **143**, 1482-1491.
193. X. Xin, F. Dai, F. Li, X. Jin, R. Wang and D. Sun, *Anal. Methods*, 2017, **9**, 3094-3098.
194. S. Nandi, H. Reinsch, S. Banesh, N. Stock, V. Trivedi and S. Biswas, *Dalton Trans.*, 2017, **46**, 12856-12864.
195. Y.-Y. Cao, X.-F. Guo and H. Wang, *Sens. Actuators B*, 2017, **243**, 8-13.
196. S. S. Nagarkar, A. V. Desai and S. K. Ghosh, *Chem. Eur. J.*, 2015, **21**, 9994-9997.
197. X.-F. Yang, H.-B. Zhu and M. Liu, *Inorg. Chim. Acta*, 2017, **466**, 410-416.
198. O. Yassine, O. Shekhah, A. H. Assen, Y. Belmabkhout, K. N. Salama, and M. Eddaoudi, *Angew. Chem. Int. Ed.*, 2016, **55**, 15879-15883.
199. X. Wan, L. Wu, L. Zhang, H. Song and Y. Lv, *Sens. Actuators B*, 2015, **220**, 614-621.
200. Y.-P. Li, S.-N. Li, Y.-C. Jiang, M.-C. Hu and Q.-G. Zhai, *Chem. Commun.*, 2018, **54**, 9789-9792.
201. N. A. Travlou, K. Singh, E. Rodríguez-Castellón and T. J. Bandosz, *J. Mater. Chem. A*, 2015, **3**, 11417-11429.
202. K. Sel, S. Demirci, O. F. Ozturk, N. Aktas and N. Sahiner, *Microelectron. Eng.*, 2015, **136**, 71-76.
203. S. K. Bhardwaj, G. C. Mohanta, A. L. Sharma, K. H. Kim and A. Deep, *Anal. Chim. Acta.*, 2018, **1043**, 89-97.
204. N. B. Shustova, A. F. Cozzolino, S. Reineke, M. Baldo and M. Dincă, *J. Am. Chem. Soc.*, 2013, **135**, 13326-13329.
205. J.-N. Hao and B. Yan, *Nanoscale*, 2016, **8**, 2881-2886.
206. I. A. Ibarra, T. W. Hesterberg, J. S. Chang, J. W. Yoon, B. J. Holliday and S. M. Humphrey, *Chem. Commun.*, 2013, **49**, 7156-7158.
207. A. Sousaraei, C. Queiros, F. G. Moscoso, T. Lopes-Costa, J. M. Pedrosa, A. M. G. Silva, L. Cunha-Silva and J. Cabanillas-Gonzalez, *Anal. Chem.*, 2019, **91**, 15853-15859.
208. J. Zhang, D. Yue, T. Xia, Y. Cui, Y. Yang and G. Qian, *Micro. Mesoporous Mater.*, 2017, **253**, 146-150.
209. X. Lian, Y.-J. Zhou, H.-F. Zhang, M. Li and X.-C. Huang, *J. Mater. Chem. C*, 2020, **8**, 3622-3625.
210. A. H. Assen, O. Yassine, O. Shekhah, M. Eddaoudi and K. N. Salama, *ACS Sens.*, 2017, **2**, 1294-1301.
211. R. Liu, Y. Liu, S. Yu, C. Yang, Z. Li and G. Li, *ACS Appl. Mater. Interfaces*, 2019, **11**, 1713-1722.
212. K. Guo, L. Zhao, S. Yu, W. Zhou, Z. Li and G. Li, *Inorg. Chem.*, 2018, **57**, 7104-7112.
213. Z. Sun, S. Yu, L. Zhao, J. Wang, Z. Li and G. Li, *Chem. Eur. J.*, 2018, **24**, 10829-10839.
214. E. Martínez-Ahumada, A. López-Olvera, V. Jancik, J. E. Sánchez-Bautista, E.González-Zamora, V. Martis, D. R. Williams and I. A. Ibarra, *Organometallics*, 2020, **39**, 883-915.
215. Q. Li, J. Wu, L. Huang, J. Gao, H. Zhou, Y. Shi, Q. Pan, G. Zhang, Y. Du and W. Liang, *J. Mater. Chem. A*, 2018, **6**, 12115-12124.
216. M. E. DMello, N. G. Sundaram, A. Singh, A. K. Singh and S. B. Kalidindi, *Chem. Commun.*, 2019, **55**, 349-352.
217. C. H. Pham and F. Paesani, *Inorg. Chem.*, 2018, **57**, 9839-9843.
218. M. Wang, L. Guo and D. Cao, *Anal. Chem.*, 2018, **90**, 3608-3614.
219. J. Zhang, T. Xia, D. Zhao, Y. Cui, Y. Yang and G. Qian, *Sens. Actuators B*, 2018, **260**, 63-69.
220. M. R. Tchalala, P. M. Bhatt, K. N. Chappanda, S. R. Tavares, K. Adil, Y. Belmabkhout, A. Shkurenko, A. Cadiau, N. Heymans, G. De Weireld, G. Maurin, K. N. Salama and M. Eddaoudi, *Nat. Commun.*, 2019, **10**, 1328.
221. V. Chernikova, O. Yassine, O. Shekhah, M. Eddaoudi and Khaled N. Salama, *J. Mater. Chem. A*, 2018, **6**, 5550-5554.
222. S. Yang, J. Sun, A. J. Ramirez-Cuesta, S. K. Callear, W. I. F. David, D. P. Anderson, R. Newby, A. J. Blake, J. E. Parker, C. C. Tang and M. Schröder, *Nat. Chem.*, 2012, **4**, 887-894.
223. K. Rui, X. Wang, M. Du, Y. Zhang, Q. Wang, Z. Ma, Q. Zhang, D. Li, X. Huang, G. Sun, J. Zhu and W. Huang, *ACS Appl. Mater. Interfaces*, 2018, **10**, 2837-2842.
224. G. W. Peterson, J. J. Mahle, J. B. DeCoste, W. O. Gordon and and J. A. Rossin, *Angew. Chem. Int. Ed.*, 2016, **55**, 6235-6238.
225. M. Schulz, A. Gehl, J. Schlenkrich, H. A. Schulze, S. Zimmermann and A. Schaate, *Angew. Chem. Int. Ed.*, 2018, **57**, 12961-12965.
226. A. M. Ebrahim and T. J. Bandosz, *ACS Appl. Mater. Interfaces*, 2013, **5**, 10565-10573.
227. G. Nickerl, I. Senkovska and S. Kaskel, *Chem. Commun.*, 2015, **51**, 2280-2282.
228. S. Yuvaraja, S. G. Surya, V. Chernikova, M. T. Vijjapu, O. Shekhah, P. M. Bhatt, S. Chandra, M. Eddaoudi and K. N. Salama, *ACS Appl. Mater. Interfaces*, 2020, **12**, 18748-18760.
229. A. Gamonal, C. Sun, A. L. Mariano, E. Fernandez-Bartolome, E. Guerrero-SanVicente, B. Vlaisavljevich, J. Castells-Gil, C. Marti-Gastaldo, R. Poloni, R. Wannemacher, J. Cabanillas-Gonzalez and J. S. Costa, *J. Phys. Chem. Lett.*, 2020, **11**, 3362−3368.
230. Z. Meng, A. Aykanat and K. A. Mirica, *J. Am. Chem. Soc.*, 2019, **141**, 2046-2053.
231. P. Wu, J. Wang, C. He, X. Zhang, Y. Wang, T. Liu and C. Duan, *Adv. Funct. Mater.*, 2012, **22**, 1698-1703.
232. A. V. Desai, P. Samanta, B. Manna and S. K. Ghosh, *Chem. Commun.*, 2015, **51**, 6111-6114.
233. Y. Ye, H. Liu, Y. Li, Q. Zhuang, P. Liu and J. Gu, *Talanta*, 2019, **200**, 472-479.
234. A. Beltrán, M. I. Burguete, D. R. Abánades, D. Pérez-Sala, S. V. Luis and F. Galindo, *Chem. Commun.*, 2014, **50**, 3579-3581.
235. D. A. Reed, D. J. Xiao, M. I. Gonzalez, L. E. Darago, Z. R. Herm, F. Grandjean and J. R. Long, *J. Am. Chem. Soc.*, 2016, **138**, 5594-5602.
236. A. Toscani, C. Marín-Hernández, M. E. Moragues, F. Sancenón, P. Dingwall, N. J. Brown, R. Martínez-Máñez, A. J. White and J. D. Wilton-Ely, *Chem. Eur. J.*, 2015, **21**, 14529-14538.
237. X. Zou, J.-M. Goupil, S. Thomas, F. Zhang, G. Zhu, V. Valtchev and S. Mintova, *J. Phys. Chem. C*, 2012, **116**, 16593-16600.
238. K. Hwang, J. Ahn, I. Cho, K. Kang, K. Kim, J. Choi, K. Polychronopoulou and I. Park, *ACS Appl. Mater. Interfaces*, 2020, **12**, 13338-13347.
239. I. Stassen, J. H. Dou, C. Hendon and M. Dincă, *ACS Cent. Sci.*, 2019, **5**, 1425-1431.
240. N. G. Sundaram, M. E. DMello and S. B. Kalidindi, *Chem. Eur. J.*, 2018, **24**, 9220-9223.
241. I. Strauss, A. Mundstock, M. Treger, K. Lange, S. Hwang, C. Chmelik, P. Rusch, N. C. Bigall, T. Pichler, H. Shiozawa and J. Caro, *ACS Appl. Mater. Interfaces*, 2019, **11**, 14175-14181.
242. P. Freund, L. Mielewczyk, M. Rauche, I. Senkovska, S. Ehrling, E. Brunner and S. Kaskel, *ACS Sustainable Chem. Eng.*, 2019, **7**, 4012-4018.
243. J. Devkota, K.-J. Kim, P. R. Ohodnicki, J. T. Culp, D. W. Greve and J. W. Lekse, *Nanoscale*, 2018, **10**, 8075-8087.
244. J. J. Gassensmith, J. Y. Kim, J. M. Holcroft, O. K. Farha, J. F. Stoddart, J. T. Hupp and N. C. Jeong, *J. Am. Chem. Soc.*, 2014, **136**, 8277-8282.
245. V. Pentyala, P. Davydovskaya, M. Ade, R. Pohle and G. Urban, *Sens. Actuators B*, 2016, **225**, 363-368.

246. J. Hromadka, B. Tokay, R. Correia, S. P. Morgan and S. Korposh, *Sens. Actuators B*, 2018, **255**, 2483-2494.
247. X. Chong, P. R. Ohodnicki, E. Li, C.-H. Chang and A. X. Wang, *IEEE Sens. J.*, 2015, **15**, 5327-5332.
248. X.-L. Qu and B. Yan, *Inorg. Chem.*, 2019, **58**, 524-534.
249. Z.-F. Wu, B. Tan, M.-L. Feng, A.-J. Lan and X.-Y. Huang, *J. Mater. Chem. A*, 2014, **2**, 6426-6431.
250. Y. Dong, *J. Mol. Struct.*, 2018, **1160**, 46-49.
251. X.-D. Liu and Z.-L. Hou, *Inorg. Chem. Commun.*, 2018, **95**, 78-81.
252. Z.-F. Wu, B. Tan, M.-L. Feng, C.-F. Du and X.-Y. Huang, *J. Solid State Chem.*, 2015, **223**, 59-64.
253. L. Zhai, Z.-X. Yang, W.-W. Zhang, J.-L. Zuo and X.-M. Ren, *J. Mater. Chem. C*, 2018, **6**, 7030-7041.
254. D.-M. Chen, J.-Y. Tian, M. Chen, C.-S. Liu and M. Du, *ACS Appl. Mater. Interfaces*, 2016, **8**, 18043-18050.
255. P.-Y. Du, W. P. Lustig, S. J. Teat, W. Gu, X. Liu and J. Li, *Chem. Commun.*, 2018, **54**, 8088-8091.
256. M. Leidinger, M. Rieger, T. Sauerwald, C. Alépée and A. Schütze, *Sens. Actuators B*, 2016, **236**, 988-996.
257. C. S. L. Koh, H. K. Lee, X. Han, H. Y. F. Sim and X. Y. Ling, *Chem. Commun.*, 2018, **54**, 2546-2549.
258. J.-Y. Ge, H.-Y. Wang, J. Li, J.-Z. Xie, Y. Song and J.-L. Zuo, *Dalton Trans.*, 2017, **46**, 3353-3362.
259. A. Lan, K. Li, H. Wu, D. H. Olson, T. J. Emge, W. Ki, M. Hong and J. Li, *Angew. Chem. Int. Ed.*, 2009, **48**, 2334-2338.
260. M. Zhang, G. Feng, Z. Song, Y. P. Zhou, H. Y. Chao, D. Yuan, T. T. Tan, Z. Guo, Z. Hu, B. Z. Tang, B. Liu and D. Zhao, *J. Am. Chem. Soc.*, 2014, **136**, 7241-7244.
261. M.-J. Dong, M. Zhao, S. Ou, C. Zou and C.-D. Wu, *Angew. Chem. Int. Ed.*, 2014, **53**, 1575-1579.
262. H. Zhao, J. Ni, J. J. Zhang, S.-Q. Liu, Y.-J. Sun, H. Zhou, Y.-Q. Li and C.-Y. Duan, *Chem. Sci.*, 2018, **9**, 2918-2926.
263. C.-T. He, J.-Y. Tian, S.-Y. Liu, G. Ouyang, J.-P. Zhang and X.-M. Chen, *Chem. Sci.*, 2013, **4**, 351-356.
264. F.-Y. Yi, Y. Wang, J.-P. Li, D. Wu, Y.-Q. Lan and Z.-M. Sun, *Mater. Horiz.*, 2015, **2**, 245-251.
265. X.-G. Liu, H. Wang, B. Chen, Y. Zou, Z. G. Gu, Z. Zhao and L. Shen, *Chem. Commun.*, 2015, **51**, 1677-1680.
266. Y. Zhou and B. Yan, *Chem. Commun.*, 2016, **52**, 2265-2268.
267. F. Wang, W. Liu, S. J. Teat, F. Xu, H. Wang, X. Wang, L. An and J. Li, *Chem. Commun.*, 2016, **52**, 10249-10252.
268. Z. Guo, X. Song, H. Lei, H. Wang, S. Su, H. Xu, G. Qian, H. Zhang and B. Chen, *Chem. Commun.*, 2015, **51**, 376-379.
269. D.-M. Chen, N.-N. Zhang, C.-S. Liu and M. Du, *J. Mater. Chem. C*, 2017, **5**, 2311-2317.
270. X. Zhao, Y. Li, Z. Chang, L. Chen and X.-H. Bu, *Dalton Trans.*, 2016, **45**, 14888-14892.
271. S. L. Jackson, A. Rananaware, C. Rix, S. V. Bhosale and K. Latham, *Cryst. Growth Des.*, 2016, **16**, 3067-3071.
272. S. Pramanik, C. Zheng, X. Zhang, T. J. Emge and J. Li, *J. Am. Chem. Soc.*, 2011, **133**, 4153-4155.
273. F. Xu, L. Sun, P. Huang, Y. Sun, Q. Zheng, Y. Zou, H. Chu, E. Yan, H. Zhang, J. Wang and Y. Du, *Sens. Actuators B*, 2018, **254**, 872-877.
274. T. Xu, P. Xu, D. Zheng, H. Yu and X. Li, *Anal. Chem.*, 2016, **88**, 12234-12240.
275. J. Jiang, Z.-H. Ma, R. Liu and X. He, *Inorg. Chim. Acta*, 2020, **501**, 119241.
276. E. Haghighi and S. Zeinali, *RSC Adv.*, 2019, **9**, 24460-24470.
277. H. Yuan, J. Tao, N. Li, A. Karmakar, C. Tang, H. Cai, and N. S. S. J. Pennycook and D. Zhao, *Angew. Chem. Int. Ed.*, 2019, **58**, 14089-14094.
278. M. L. Aubrey, M. T. Kapelewski, J. F. Melville, J. Oktawiec, D. Presti, L. Gagliardi and J. R. Long, *J. Am. Chem. Soc.*, 2019, **141**, 5005-5013.
279. Y.-L. Peng, T. Pham, P. Li, T. Wang, Y. Chen, K.-J. Chen, K. A. Forrest, B. Space, P. Cheng, M. J. Zaworotko and Z. Zhang, *Angew. Chem. Int. Ed.*, 2018, **57**, 10971-10975.
280. J. A. Gustafson and C. E. Wilmer, *ACS Sens.*, 2019, **4**, 1586-1593.
281. A. M. Marti, S. D. Perera, L. D. McBeath and K. J. Balkus, Jr., *Langmuir*, 2013, **29**, 5927-5936.
282. H. Yamagiwa, S. Sato, T. Fukawa, T. Ikehara, R. Maeda, T. Mihara and M. Kimura, *Sci. Rep.*, 2014, **4**, 6247.
283. S. Zeinali, S. Homayoonnia and G. Homayoonnia, *Sens. Actuators B*, 2019, **278**, 153-164.
284. P. Davydovskaya, V. Pentyala, O. Yurchenko, L. Hussein, R. Pohle and G. A. Urban, *Sens. Actuators B*, 2014, **193**, 911-917.
285. M.-S. Yao, W.-X. Tang, G.-E. Wang, B. Nath and G. Xu, *Adv. Mater.*, 2016, **28**, 5229-5234.
286. B. Chen, Y. Yang, F. Zapata, G. Lin, G. Qian and E. B. Lobkovsky, *Adv. Mat.*, 2007, **19**, 1693-1696.
287. X.-Z. Song, S.-Y. Song, S.-N. Zhao, Z.-M. Hao, M. Zhu, X. Meng, L.-L. Wu and H.-J. Zhang, *Adv. Funct. Mater.*, 2014, **24**, 4034-4041.
288. Q. Zhang, J. Wang, A. M. Kirillov, W. Dou, C. Xu, C. Xu, L. Yang, R. Fang and W. Liu, *ACS Appl. Mater. Interfaces*, 2018, **10**, 23976-23986.
289. X. Dao, Y. Ni and H. Pan, *Sens. Actuators B*, 2018, **271**, 33-43.
290. H. Pan, S. Wang, X. Dao and Y. Ni, *Inorg. Chem.*, 2018, **57**, 1417-1425.
291. J. Wang, J. Wang, Y. Li, M. Jiang, L. Zhang and P. Wu, *New J. Chem.*, 2016, **40**, 8600-8606.
292. V. Sasikala, J. K. Sundar and M. A. Lakshmi, *ChemistrySelect*, 2019, **4**, 3862-3870.
293. K. Wang, Z. Lin, S. Huang, J. Sun and Q. Zhang, *Eur. J. Inorg. Chem.*, 2016, **2016**, 3411-3416.
294. F.-Y. Yi, W. Yang and Z.-M. Sun, *J. Mater. Chem.*, 2012, **22**, 23201-23209.
295. H.-N. Wang, S.-Q. Jiang, Q.-Y. Lu, Z.-Y. Zhou, S.-P. Zhuo, G.-G. Shan and Z.-M. Su, *RSC Adv.*, 2015, **5**, 48881-48884.
296. Y. Song, R. Fan, X. Du, K. Xing, Y. Dong, P. Wang and Y. Yang, *RSC Adv.*, 2016, **6**, 110182-110189.
297. M. Zhao, Z.-Q. Yao, Y.-L. Xu, Z. Chang and X.-H. Bu, *RSC Adv.*, 2017, **7**, 2258-2263.
298. Y. Liu, W. Liu, C. Xu, W. Dou, Z. Ju and W. Liu, *New J. Chem.*, 2018, **42**, 3885-3891.
299. N. Goel and N. Kumar, *RSC Adv.*, 2018, **8**, 10746-10755.
300. Y. Yang, L. Chen, F. Jiang, M. Wu, J. Pang, X. Wan and M. Hong, *CrystEngComm*, 2019, **21**, 321-328.
301. F. Yuan, T.-T. Wang, H.-M. Hu, C.-T. Li, C.-S. Zhou, X. Wang and G. Xue, *J. Solid State Chem.*, 2017, **251**, 79-89.
302. X. Shi, Y. Fan, J. Xu, H. Qi, J. Chai, J. Sun, H. Jin, X. Chen, P. Zhang and L. Wang, *Inorg. Chim. Acta*, 2018, **483**, 473-479.
303. M. Arıcı, O. Zafer Yeşilel and O. Büyükgüngör, *J. Solid State Chem.*, 2017, **249**, 141-148.
304. J. Jia, P. Wang, J. Chai, B. Ma, J. Sun, X. Chen, Y. Fan, L. Wang and J. Xu, *J. Solid State Chem.*, 2017, **253**, 430-437.
305. T.-T. Han, H.-L. Bai, Y.-Y. Liu and J.-F. Ma, *J. Solid State Chem.*, 2019, **269**, 588-593.
306. B.-L. Li, H.-N. Wang, L. Zhao, G.-Z. Li and Z.-M. Su, *Inorg. Chem. Commun.*, 2016, **66**, 87-89.
307. J. Sun, K.-X. Shang, Y.-J. Wu, Q. Zhang, X.-Q. Yao, Y.-X. Yang, D.-C. Hu and J.-C. Liu, *Polyhedron*, 2018, **141**, 223-229.
308. S. Kumar, A. Arora, A. Kumar and K. Tomar, *Inorg. Chem. Commun.*, 2018, **96**, 16-19.
309. X.-Y. Xu and B. Yan, *ACS Appl. Mater. Interfaces*, 2015, **7**, 721-729.
310. J. Zhang, S. B. Peh, J. Wang, Y. Du, S. Xi, J. Dong, A. Karmakar, Y. Ying, Y. Wang and D. Zhao, *Chem. Commun.*, 2019, **55**, 4727-4730.
311. Y. Zhao, Z. Zhang, T. Cao, L. Wang, Y. Fan, T. Wan and J. Jia, *Polyhedron*, 2020, **177**, 114314.
312. P. Davydovskaya, A. Ranft, B. V. Lotsch and R. Pohle, *Anal. Chem.*, 2014, **86**, 6948-6958.

313. G. Ren, Z. Li, W. Yang, M. Faheem, J. Xing, X. Zou, Q. Pan, G. Zhu and Y. Du, *Sens. Actuators B*, 2019, **284**, 421-427.
314 X.-Y. Bai, W.-J. Ji, S.-N. Li, Y.-C. Jiang, M.-C. Hu and Q.-G. Zhai, *Cryst. Growth Des.*, 2016, **17**, 423-427.
315. W. Liu, Y.-Y. Peng, S.-G. Wu, Y.-C. Chen, M. N. Hoque, Z.-P. Ni, X.-M. Chen and M.-L. Tong, *Angew. Chem. Int. Ed.*, 2017, **56**, 14982-14986.
316. W. Huang, F. X. Shen, S.-Q. Wu, L. Liu, D. Wu, Z. Zheng, J. Xu, M. Zhang, X.-C. Huang, J. Jiang, F. Pan, Y. Li, K. Zhu and O. Sato, *Inorg. Chem.*, 2016, **55**, 5476-5484.
317. Q. Chen, J. Li, Y.-S. Meng, H.-L. Sun, Y.-Q. Zhang, J.-L. Sun and S. Gao, *Inorg. Chem.*, 2016, **55**, 7980-7987.
318. J.-Y. Li, Y.-C. Chen, Z.-M. Zhang, W. Liu, Z.-P. Ni and M.-L. Tong, *Chem. Eur. J.*, 2015, **21**, 1645-1651.
319. R. A. Polunin, N. P. Burkovskaya, J. A. Satska, S. V. Kolotilov, M. A. Kiskin, G. G. Aleksandrov, O. Cador, L. Ouahab, I. L. Eremenko and V. V. Pavlishchuk, *Inorg. Chem.*, 2015, **54**, 5232-5238.
320. T. Zhao, I. Boldog, V. Spasojevic, A. Rotaru, Y. Garcia and C. Janiak, *J. Mater. Chem. C*, 2016, **4**, 6588-6601.
321. P. Müller, F. M. Wisser, V. Bon, R. Grünker, I. Senkovska and S. Kaskel, *Chem. Mater.*, 2015, **27**, 2460-2467.
322. M. M. Wanderley, C. Wang, C.-D. Wu and W. Lin, *J. Am. Chem. Soc.*, 2012, **134**, 9050-9053.
323. C. Cui, Y. Liu, H. Xu, S. Li, W. Zhang, P. Cui and F. Huo, *Small*, 2014, **10**, 3672-3676.
324. X. Lian and B. Yan, *Inorg. Chem.*, 2016, **55**, 11831-11838.
325. H. Zhang, D. Chen, H. Ma and P. Cheng, *Chem. Eur. J.*, 2015, **21**, 15854-15859.
326. S. Durini, N. Ilić, K. Ramazanova, T. Grell, P. Lönnecke and E. Hey-Hawkins, *Chempluschem*, 2019, **84**, 307-313.
327. X. Wan, H. Song, D. Zhao, L. Zhang and Y. Lv, *Sens. Actuators B*, 2014, **201**, 413-419.
328. A. V. Desai, S. Sharma, A. Roy, M. M. Shirolkar and S. K. Ghosh, *Mol. Syst. Des. Eng.*, 2020, **5**, 469-476.
329. J.-P. Zheng, S. Ou, M. Zhao and C.-D. Wu, *ChemPlusChem*, 2016, **81**, 758-763.
330. S. Sachdeva, D. Soccol, D. J. Gravesteijn, F. Kapteijn, E. J. R. Sudhölter, J. Gascon and L. C. P. M. de Smet, *ACS Sens.*, 2016, **1**, 1188-1192.
331. M. A. Andrés, M. T. Vijjapu, S. G. Surya, O. Shekhah, K. N. Salama, C. Serre, M. Eddaoudi, O. Roubeau and I. Gascón, *ACS Appl. Mater. Interfaces*, 2020, **12**, 4155-4162.
332. M. R. Venkatesh, S. Sachdeva, B. El Mansouri, J. Wei, A. Bossche, D. Bosma, L. de Smet, E. J. R. Sudhölter and G. Q. Zhang, *Sensors*, 2019, **19**, 888.
333. S. Sachdeva, S. J. H. Koper, A. Sabetghadam, D. Soccol, D. J. Gravesteijn, F. Kapteijn, E. J. R. Sudholter, J. Gascon and L. de Smet, *ACS Appl. Mater. Interfaces*, 2017, **9**, 24926-24935.
334. S. Homayoonnia and S. Zeinali, *Sens. Actuators B*, 2016, **237**, 776-786.
335. J.-N. Hao and B. Yan, *Nanoscale*, 2016, **8**, 12047-12053.
336. H. Tian, H. Fan, M. Li and L. Ma, *ACS Sens.*, 2015, **1**, 243-250.
337. X.-Y. Xu and B. Yan, *J. Mater. Chem. A*, 2017, **5**, 2215-2223.
338. K. Vellingiri, A. Deep, K.-H. Kim, D. W. Boukhvalov, P. Kumar and Q. Yao, *Sens. Actuators B*, 2017, **241**, 938-948.
339. Y. Wang, G. Zhang, F. Zhang, T. Chu and Y. Yang, *Sens. Actuators B*, 2017, **251**, 667-673.
340. C. Li, J. Huang, H. Zhu, L. Liu, Y. Feng, G. Hu and X. Yu, *Sens. Actuators B*, 2017, **253**, 275-282.
341. Y.-Y. Xue, J.-L. Wang, S.-N. Li, Y.-C. Jiang, M.-C. Hu and Q.-G. Zhai, *J. Solid State Chem.*, 2017, **251**, 170-175.
342. Z.-Z. Lu, R. Zhang, Y.-Z. Li, Z.-J. Guo and H.-G. Zheng, *J. Am. Chem. Soc.*, 2011, **133**, 4172-4174.
343. C.-Y. Liu, X.-R. Chen, H.-X. Chen, Z. Niu, H. Hirao, P. Braunstein and J.-P. Lang, *J. Am. Chem. Soc.*, 2020, **142**, 6690-6697.
344. Y. Yu, J.-P. Ma, C.-W. Zhao, J. Yang, X.-M. Zhang, Q.-K. Liu and Y.-B. Dong, *Inorg. Chem.*, 2015, **54**, 11590-11592.
345. F.-Y. Yi, S.-C. Wang, M. Gu, J.-Q. Zheng and L. Han, *J. Mater. Chem. C*, 2018, **6**, 2010-2018.
346. Z. Hu, C.-A. Tao, H. Liu, X. Zou, H. Zhu and J. Wang, *J. Mater. Chem. A*, 2014, **2**, 14222-14227.
347. S. A. A. Razavi, M. Y. Masoomi and A. Morsali, *Chem. Eur. J.*, 2017, **23**, 12559-12564.
348. Y. Li, S. Zhang and D. Song, *Angew. Chem. Int. Ed.*, 2013, **52**, 710-713.
349. F.-Y. Yi, J. Chen, S.-C. Wang, M. Gu and L. Han, *Chem. Commun.*, 2018, **54**, 8233-8236.
350. W.-J. Li, S.-Y. Gao, T.-F. Liu, L.-W. Han, Z.-J. Lin and R. Cao, *Langmuir*, 2013, **29**, 8657-8664.
351. V. Zeleňák, M. Almáši, A. Zeleňáková, P. Hrubovčák, R. Tarasenko, S. Bourelly and P. Llewellyn, *Sci. Rep.*, 2019, **9**, 15572.
352. A. Mondal, A. K. Kharwar and S. Konar, *Inorg. Chem.*, 2019, **58**, 10686-10693.

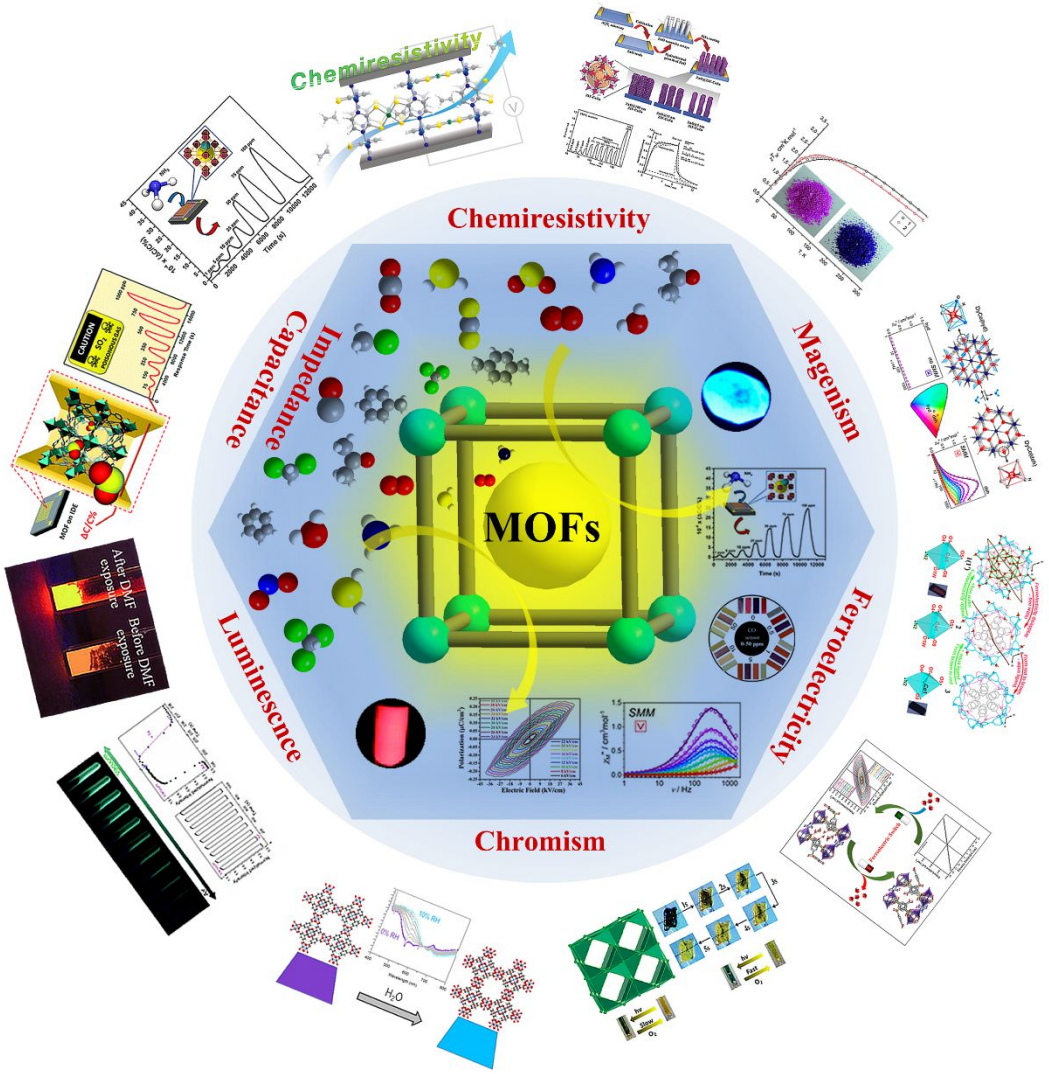

This review summarizes the recent advances of metal organic framework (MOF) based sensing of gases and volatile compounds.